MODELING COUPLED FLUID FLOW AND GEOMECHANICAL AND GEOPHYSICAL PHENOMENA WITHIN A FINITE ELEMENT FRAMEWORK

by

Matthew M. Silbernagel

A thesis submitted to the Faculty and The Board of Trustees of the Colorado School of Mines in partial fulfillment of the requirements for the degree of Master of Science (Geophysical Engineering).

Golden, Colorado

Date 06-16-2007

Signed: Matthew Silbernagel
Matthew M. Silbernagel

Approved: Michael L. Batzle
Dr. Michael L. Batzle
Thesis Advisor

Date June 20, 2007

Terence K. Young
Dr. Terence K. Young
Professor and Head
Department of Geophysics

ABSTRACT

A fully coupled finite-element approach is taken for the modeling of geomechanical effects induced by reservoir production/injection and the cyclic dependence between pore fluid flow and the concurring deformation of the solid rock matrix. The governing equations and constitutive relations of fluid flow are coupled to stress-strain relations. With the appropriate boundary and initial conditions, these equations are implemented as partial differential equations into a customizable finite element software package. Several representative numerical simulations are presented to illustrate the validity, applicability, and usefulness of the fully-coupled approach. The ability to predict observable phenomena—ignored in decoupled models—is verified in the finite-element poroelastic formulation. Specifically, the Mandel-Cryer effect (initially higher pore pressures resulting from a drained boundary condition) and the Noordbergum effect (initially higher pore pressures resulting from layered heterogeneity) are simulated in the models. These models are relevant to a wide range of petroleum and hydrogeologic investigations, including sample-scale loading experiments, wellbore pressure-transient testing, and reservoir-scale deformation analysis, and seismic time-lapse studies.

Special consideration is given for implementing a nonlinear elasticity formulation for directly linking the changes in the effective stress field to changes in seismic velocities during reservoir production and injection. The results are analyzed in terms of pore fluid pressure, effective vertical stress, strain, and seismic velocities. Fluid withdrawal from the reservoir causes "stress arching," which is manifested as strain contraction within the reservoir, and strain expansion in the host rock. Pore fluid pressures are tightly linked to the specified initial porosity (range: 5% to 45%) and reservoir permeability (range: 1e-11 m^2 to 1e-14 m^2). Lower reservoir permeabilities cause more drastic changes in the amplitudes of the cones of pressure depression and expansion around a producing well and a injection well, respectively. A higher initial porosity maintains higher pressure profiles throughout the reservoir during constant production. As the initial reservoir porosity is varied, the amplitudes of the cones of pressure depression are uniform from year to year. The specified initial porosity and the

fluid content are the dominate controls on velocity changes, especially the slow (Biot) wave. Increasing porosity significantly increases the slow wave velocity as fluid mobility improves. The Vp/Vs ratio is found to be an indicator of the degree of consolidation with depth.

The distinctive contribution of thesis is a unified, internally consistent numerical framework that illustrates the mutual interdependency of fluid-structure interaction and the seismic velocity response. While not encompassing all possibly relevant phenomena, the work in this thesis takes an principal step in developing fully coupled platform that handle parametric sensitivity and interdependency of several phenomena, which is critical for analyzing multicomponent seismic data and optimizing production.

TABLE OF CONTENTS

ABSTRACT iii
LIST OF FIGURES viii
LIST OF TABLES xiii
ACKNOWLEDGEMENTS xiv
CHAPTER 1. INTRODUCTION 1
1.1 Introduction to Integrated Reservoir Modeling 1
1.2 Historical Perspective 1
1.3 Overview of Poroelastic Concepts and Reservoir Geomechanics Approach 2
1.4 Notable Occurrences of Deforming Reservoirs 5
1.4.1 Valhall Field 6
1.4.2 Wilmington Field 6
1.4.3 Genesis Field 7
1.4.4 Other Occurrences and Issues 8
1.5 Recent Approaches and Challenges 10
1.6 Integration with Time-Lapse Seismics 11
1.6.1 Modified Gassmann Methodology 12
1.6.2 Nonlinear Anisotropic Elasticity Methodology 14
1.6.3 A Numerical Example at Belridge Field 14
1.7 Aims and Objectives of this Thesis 16
1.8 Thesis Outline 17
CHAPTER 2. THEORETICAL BACKGROUND OF MODELING PHENOMENOLOGY 18
2.1 Constitutive Relations 18
2.2 Governing Equations 21
2.2.1 Force Equilibrium Equations 22
2.2.2 Fluid Flow Relations 24
2.2.3 Boundary and Initial Conditions 25
2.3 Poroelastic Modeling in Comsol Multiphysics 3.3a 26
2.4 Summary of Equations and Discussion 27

CHAPTER 3. COUPLING STRATEGIES 30
3.1 Introduction 30
3.2 Coupling Mechanics and Notation 30
3.3 Loose Coupling 31
3.4 Iterative Coupling 31
3.5 Explicit Coupling 32
3.6 Full Coupling and Comparison of Numerical Approaches 33
3.7 Summary 34
CHAPTER 4. PRACTICAL NUMERICAL SIMULATIONS 35
4.1 Introduction 35
4.2 Uniaxially-Constrained Consolidation Test 35
4.2.1 Model Description 35
4.2.2 Model Results and Discussion 37
4.3 Verification of Mandel-Cryer's Problem 40
4.3.1 Model Description 41
4.3.2 Model Results and Discussion 43
4.4 Formation Pressure Testing Simulation 45
4.4.1 Model Description 46
4.4.2 Model Results and Discussion 49
4.5 Modeling of the Noordbergum Effect through the Compaction of a Pumped Confined Aquifer 53
4.5.1 Model Description 54
4.5.2 Model Results and Discussion 59
4.6 4-D Reservoir Simulation Tied to Modeling Changes in Seismic Velocities 63
4.6.1 Model Description 63
4.6.2 Model Results 69
4.6.3 Parameter Sensitivity 78
4.7 Discussion on Stability 91
4.8 Summary of Salient Features 92

CHAPTER 5. CONCLUSIONS AND RECOMMENDATIONS 94
5.1 Conclusions 94
5.2 Recommendations for Future Work 95
REFERENCES 98
APPENDICES 105
APPENDIX A: Superposition of Finite Element Matrices and Notation 105
APPENDIX B: Nonlinear Elasticity and Two-Phase Fluid Flow Theory 106

LIST OF FIGURES

Figure 1-1. Schematic of general grain geometry. (from Biot (1962)) 3

Figure 1-2. Schematic illustrating Terzaghi's (1943) description of effective stress and the effect on seismic velocities. (after Calvert (2005)) 4

Figure 1-3. Reducing pore pressure leads to contraction of the reservoir and dilation in the overburden, resulting in significant effective stress (σ') changes outside of the reservoir. (modified after Dusseault (2007)) 5

Figure 1-4. Subsidence problems at Wilmington Field in Long Beach, California. (photo courtesy of the University of Wisconsin--Stevens Point Geology Department.) 7

Figure 1-5. Expression of geomechanical effects on the Genesis Field time-lapse signal. Panel on the left is a section taken from the difference cube 2002-1990. The four zoomed sections on the right are taken from the baseline 1990 3D survey. (modified from Duranti, 2005) 8

Figure 1-6. Subsidence costs (USD) in the United States (1991) as estimated by the National Academy of Sciences. (figures modified from NAS Report "Mitigating Losses from Land Subsidence in the United States (National Academy of Sciences, 1991)") 9

Figure 1-7. von Mises stress for the Belridge field numerical experiment after 10 years of production, considering coupled mechanical deformation and flow modeling. Range: nominal (cooler colors) to 1.15MPa (warmer colors). (data from Minkoff et al. (1999)) 15

Figure 1-8. (Top) Difference in compressional wave velocity between flow simulation alone and coupled flow and geomechanics, with only porosity changing dynamically. (Bottom) Difference in compressional wave velocity between flow simulation alone and coupled flow and geomechanics with both porosity and permeability changing dynamically. Both figures are at five years of production. (data from Minkoff et al. (2004)) 16

Figure 2-1. Normal (σ) and shear (τ) components of the stress tensor at an internal point P, shown on an infinitesimal REV. (after Wang, 2000) 22

Figure 3-1. Workflow for the iterative method for coupled variables pressure (p), temperature (T), stress and mean total stress ($\boldsymbol{\sigma}$,σ_m), strain ($\boldsymbol{\varepsilon}$), reservoir porosity (ϕ), and displacement ($\mathbf{u}$). (modified from Tran et al. (2004)) 32

Figure 4-1. Schematic of the uniaxially-constrained loading simulation. 37

Figure 4-2. Vertical displacement of the sample under uniform loading and with undrained boundaries. 38

Figure 4-3. Vertical displacement vs. height of the sample with undrained boundaries. 39

Figure 4-4. Pore pressure vs. sample height with undrained boundaries..... 39

Figure 4-5. Schematic description of the poroelastic pore-pressure response. (after Hart, 2000) 41

Figure 4-6. Schematic of fluid-saturated cylinder cross-section (1 meter in diameter) under uniformly-applied radial compressive load at t=0. 43

Figure 4-7. Cross-section of a cylinder showing early pressure (Pa) distribution. The pore pressure build up at the center indicates a Mandel-Cryer effect. The red arrows indicate fluid flow vectors. Dimensions are in meters..... 44

Figure 4-8. Pressure (Pa) at the center (x=0,y=0) of the cylinder vs. time (sec). The fully-coupled poroelastic simulation captures the expected nonmonotonic behavior due to the Mandel-Cryer effect. 45

Figure 4-9. Schematic drawing showing a dual-packer drill stem formation tester. 46

Figure 4-10. Finite element mesh containing 369 triangular elements. The mesh refines gradually toward the sink located at x=(0,0), y=(-187.5,-212.5). Dimensions are in meters. 48

Figure 4-11. Drill stem test simulation showing a surface plot of the von Mises stress distribution after the drawdown rate of 1m/day applied for t=2.4 hours. The black lines indicate the streamlines of fluid flow and the arrows indicate fluid velocity. . 49

Figure 4-12. von Mises stress distribution over the entire drawdown period with 0.05-hour (3-minute) time intervals. 50

Figure 4-13. Distribution of total displacement through the reservoir with 0.05-hour (3-minute) time intervals from t=0 to t=2.4 hours..... 51

Figure 4-14. Pressure Distribution through the reservoir with 0.05-hour (3-minute) time intervals from t=0 to t=2.4 hours. 52

Figure 4-15. Pressure history at y=-200 m for a drawdown rate of 1/m day applied for t=0.1 days hours. 53

Figure 4-16. The three subdomains and model geometry of the hydrogeologic system. Dimensions are in meters..... 55

Figure 4-17. Boundary conditions imposed on fluid flow for the hydrogeologic system. For clarity, the vertical scale has been exaggerated..... 57

Figure 4-18. Boundary conditions for displacements imposed on the hydrogeologic system. For clarity, the vertical scale has been exaggerated. 58

Figure 4-19. Finite mesh of the hydrogeologic system containing 2038 elements. 58

Figure 4-20. von Mises stresses (Pa), fluid streamlines, fluid velocities (vectors), and deformation (m) shown for 3860 days. Dimensions are in meters. The vertical axis has been exaggerated for clarity. 59

Figure 4-21. Horizontal strain predicted from at the ground surface for ~1 year (blue), ~5 years (green), and ~10 years (red). The range (x) is in meters and strain (ux) is dimensionless. 60

Figure 4-22. Displacements predicted by the fully-coupled poroelastic analysis (dashed lines) vs. Terzaghi's consolidation equation (solid lines). The vertical scale has been exaggerated. 61

Figure 4-23. Results of simulations of flow and deformation using the Terzaghi and Biot methods for computed vertical displacements. (from Leake and Hsieh, 1997)..... 62

Figure 4-24. Early times at 0.1 day (dark blue), 10 days (green), and 100 days (red) show the hydraulic head reversal effect along the surface of the upper aquifer (which is not pumped directly). This effect disappears in later times (500 days, light blue) as the head drops in response to prolonged pumping of the lower aquifer. 62

Figure 4-25. Two subdomains for the 3-D finite element mesh. 64

Figure 4-26. Relationship between vertical Vp and strain in the overburden and surrounding rock. In this study, strain is negative for contraction and positive for tension. The dilation factor "R" is the ratio of relative change in velocity to strain.67

Figure 4-27. Relationship between vertical Vp and strain within the reservoir. In this study, strain is positive for contraction and negative for tension. The dilation factor "R" is the ratio of change in velocity over initial velocity to strain..... 68

Figure 4-28. Location of the horizontal cross-line (dimensions in meters). 69

Figure 4-29. Profile of effective (solid frame) vertical stress (Pa) along a horizontal cross-line shown in Figure 4-28. The profile is not symmetric since the production well is located at y=4500 m and the injector well is located at 3500 m. The arrows indicate the boundaries of the reservoir. 70

Figure 4-30. Vertical compressional wave velocity (V_p) profiles. The profile is not symmetric since the production well is located at y=4500 m and the injector well is located at 3500 m. The arrows indicate the boundaries of the reservoir. 71

Figure 4-31. Change in V_p from t=0 to t=5 years plotted on a vertical slice (x=2000 m). Reservoir permeability is 1e-12 m^2 and reservoir porosity is 0.40. Dilation is

occurring in the under- and over-burden (dark blue cool color) and contraction is occurring within the reservoir (warmer colors). 72

Figure 4-32. Vertical Vp/Vs ratio profile with depth (z). Permeability of the reservoir is 1e-12 m^2 and reservoir porosity is 0.40. All other parameters are as listed in Table 4-5. 73

Figure 4-33. A profile slice (x=2000 m) of the change in vertical strain ε_{33} between t=0 and t=5 years. Warmer, positive colors indicate dilation. Cooler, negative colors indicate compression. 74

Figure 4-34. A vertical slice through the modeling domain showing the change in VpSlow from t=0 to t=5 years. The initial reservoir porosity is 0.45 and reservoir permeability is 1e-12 m^2. All other parameters are as listed in Table 4-5. 75

Figure 4-35. The compression slow (Biot) velocity profile. Reservoir porosity is 0.45 and reservoir permeability is 1e-12 m^2. All other parameters are as listed in Table 4-5. 76

Figure 4-36. VpSlow profile where reservoir porosity is 0.05 and reservoir permeability is 2e-13 m^2. All other parameters are as listed in Table 4-5. 77

Figure 4-37. Change in the epsilon anisotropic parameter (ε) from t=5 to t=0 years. 78

Figure 4-38. Total pore pressure profiles along a cross-line through the reservoir at different time stages. The parameter of interest is reservoir permeability: 1e-11 m^2 (~10 Darcy). The initial reservoir porosity is 35%. The producing well is located at y=4500 m and the injection well is located at y=3500 m. 79

Figure 4-39. Total pore pressure profiles along a cross-line through the reservoir at different time stages. The parameter of interest is reservoir permeability: 1e-12 m^2 (~1 Darcy). The initial reservoir porosity is 0.40. The producing well is located at y=4500 m and the injection well is located at y=3500 m. 80

Figure 4-40. Total pore pressure profiles along a cross-line through the reservoir at different time stages. The parameter of interest is reservoir permeability: 1e-13 m^2 (~0.1 Darcy). The initial reservoir porosity is 0.40. The producing well is located at y=4500 m and the injection well is located at y=3500 m. 81

Figure 4-41. Total pore pressure profiles along a cross-line through the reservoir at different time stages. The parameter of interest is reservoir permeability: 1e-14 m^2 (~0.01 Darcy). The initial reservoir porosity is 0.40. The producing well is located at y=4500 m and the injection well is located at y=3500 m. In this scenario, negative total fluid pressures are an artifact imposed by the fluid extraction rate around the well. 82

Figure 4-42. Total fluid pressure profile along a cross-line through the reservoir. In this case, the initial porosity is the parameter of interest and is set to 0.45. Reservoir permeability is 1e-12 m^2. All other parameters are as listed in Table 4-5. 83

Figure 4-43. Total fluid pressure profile along a cross-line through the reservoir. In this case, the initial porosity is the parameter of interest and is set to 0.40. Reservoir permeability is 1e-12 m^2. All other parameters are as listed in Table 4-5. 84

Figure 4-44. Total fluid pressure profile along a cross-line through the reservoir. In this case, the initial porosity is the parameter of interest and is set to 0.35. Reservoir permeability is 1e-12 m^2. All other parameters are as listed in Table 4-5. 85

Figure 4-45. Total fluid pressure profile along a cross-line through the reservoir. In this case, the initial porosity is the parameter of interest and is set to 0.30. Reservoir permeability is 1e-12 m^2. All other parameters are as listed in Table 4-5. 86

Figure 4-46. Total fluid pressure profile along a cross-line through the reservoir. In this case, the initial porosity is the parameter of interest and is set to 0.25. Reservoir permeability is 1e-12 m2. All other parameters are as listed in Table 4-5. 87

Figure 4-47. Total fluid pressure profile along a cross-line through the reservoir. In this case, the initial porosity is the parameter of interest and is set to 0.20. Reservoir permeability is 1e-12 m^2. All other parameters are as listed in Table 4-5. 88

Figure 4-48. Total fluid pressure profile along a cross-line through the reservoir. In this case, the initial porosity is the parameter of interest and is set to 0.15. Reservoir permeability is 1e-12 m^2. All other parameters are as listed in Table 4-5. 89

Figure 4-49. Total fluid pressure profile along a cross-line through the reservoir. In this case, the initial porosity is the parameter of interest and is set to 0.10. Reservoir permeability is 1e-12 m^2. All other parameters are as listed in Table 4-5. 90

Figure 4-50. Total fluid pressure profile along a cross-line through the reservoir. In this case, the initial porosity is the parameter of interest and is set to 0.05. Reservoir permeability is 1e-12 m^2. All other parameters are as listed in Table 4-5. 91

Figure 5-1. Confining pressure vs. porosity change, with irreversible compaction due to hysteresis. (after Batzle, 2006)..... 96

Figure 5-2. Schematic of low-frequency “shaker” apparatus (after Hofmann, 2005). 97

LIST OF TABLES

Table 3-1. Comparison of finite differences vs. finite elements methods. (after Zienkiewicz and Taylor (2000)) 33

Table 4-1. Geomechanical and fluid properties used in the Terzaghi simulation. 36

Table 4-2. Geomechanical properties of Berea sandstone and fluid properties of water for the Mandel-Cryer effect simulation. (after Wang, 2000)..... 42

Table 4-3. Material properties used in the drill stem test simulation. (from Wang, 2000) 47

Table 4-4. Geomechanical and fluid flow properties of the aquifer pumping simulation. 56

Table 4-5. Unstressed material properties used in the 3-D finite element model. 65

ACKNOWLEDGEMENTS

I appreciate all the patient help and gentle guidance from my advisor, Michael Batzle, to whom I am thankful for allowing my foray into the "garden level," despite my having a "Pauli Effect" on his experimental lab equipment. His incisive humor and adroit rock-squeezing skills elucidated the joys of the many facets of poroelasticity. I also wish to thank my committee members, Tom Davis and Jennifer Miskimins, for providing encouragement and sharing their wealth of practical experience. To L. Soutter, V. Grechka, D. Prokofiev, H. Lee, R. Hofmann, to my colleagues at the Center for Rock Abuse and the Reservoir Characterization Project, and to my friends in the Department of Geophysics, I am grateful for all the useful discussions topical to this research and beyond. Additionally, the GK-12 Partnership provided an insightful interlude into the realm of secondary education, whose students renewed my sense of wonder and curiosity in the physical sciences.

I am deeply indebted to my gracious wife, Young Shin, for her understanding and support during my late-night studies. Her love and thoughtfulness bridged my many shortcomings. The arrival of our newborn son, Lukas, was a welcomed blessing, and I appreciate his efforts in helping me type this thesis.

CHAPTER 1. INTRODUCTION

1.1 Introduction to Integrated Reservoir Modeling

Phenomena arising from the coupled interaction between pore fluid flow and structural deformation play an important role in reservoir exploration, management, and stability. Considerable effort has been made in a variety of disciplines to understand and theorize the coupled interaction. Karl Terzaghi (1925) pioneered the experimental approach using controlled laboratory experiments to reproduce the phenomena in soils, while Maurice Biot (1941) developed generalized energy balance equations as the basis for theoretical poroelastic models.

More recently, the need has emerged to implement geomechanically-coupled reservoir simulations for purposes of calibrating time-lapse geophysical models. Integrating geomechanics with reservoir fluid flow simulation and rock physics is critical to the management of poorly-consolidated, high-porosity, and stress-sensitive reservoirs. Geomechanical modeling of in situ stress conditions provides valuable insight into modeling enhanced hydrocarbon production schemes, consolidation resulting from pore fluid withdrawal, stress-strain effects on the time-lapse seismic response, borehole stability concerns, hydraulic fracture design, and so forth. However, in past applications, these three disciplines (geomechanics, fluid flow simulation, and rock physics / seismics) have been approached in isolation with limited exchange of information and feedback. A goal of this thesis is to bridge these gaps by developing a finite-element, 4-D framework from which all three problems are solved together and simultaneously at each time step.

1.2 Historical Perspective

Although the term "poroelasticity" appears to have been first coined by Geertsma (1966) in petroleum engineering, the scientific literature pertaining to poroelastic concepts is found in a variety of disciplines and spans more than 150 years. Equations of poroelasticity have roots in Darcy's law and the generalized Hooke's law. Darcy's law (1856) describes the time-dependent hydraulic flow resulting from a non-uniform pore

pressure distribution. The time-dependent pore pressure produces poroelastic stresses and strains that vary with time, which in turn couple back to the pore pressure distribution. Hookean equations of linear elasticity govern the strain-displacement relationship (Timoshenko and Goodier, 1951). A nonlinear elasticity formulation (e.g., Thurston (1974)) can be added to directly link changes in stress to changes acoustic velocities.

Terzaghi (1943) is credited with elucidating the concepts of effective stress and consolidation in civil engineering. His effective stress theory is widely used in 1-D settlement problems involving saturated, unconsolidated earth materials. For the special boundary conditions in his controlled laboratory experiments, Terzaghi assumed that the pore pressure field and the applied stress field are uncoupled. In other words, the pore pressure history curve is expected to behave monotonically after a stress is applied to a drained system.

Biot generalized Terzaghi's theory to include stress dependence and described in 3-D the poroelastic coupling between structure and fluid movement based on stress-strain constitutive relations (Biot, 1941; Biot, 1955; Biot and Willis, 1957). Biot's original formulation focused on mechanical behavior and oversimplified pore fluid flow behavior. Consequently, attempts have been made to reinterpret and reformulate Biot's equations for geomechanically coupled reservoir flow models (Verruijt, 1969; Geertsma, 1973; Rice and Cleary, 1976; Parker and Lenhard, 1987; Detournay and Cheng, 1993; Chen et al., 1995; Wang, 2000). These contributions have laid the foundation for handling the complexity and non-linearity of multiphase fluid flow within the framework of geomechanics.

1.3 Overview of Poroelastic Concepts and Reservoir Geomechanics Approach

Porous materials are solids permeated by in an internal structure of openings filled with fluid(s). The fluid and solid constituents that occupy different volumes of a porous medium can be replaced with interpenetrating continua that allow all phases to be present concurrently at every point of the entire medium. The deforming solid matrix and the fluids in the pore space typically have a relative velocity to each other, which results in the interaction between the constituents. The overall microscopic pore structure is

generally quite complicated in many geological materials. Local variability in pore aspect ratios, wettability, cementation, tortuosity, and so forth, must be considered. As such, attempting to fully describe the microscopic-scale mechanical interaction is quite laborious. Alternatively, building a macroscopic scale model is more feasible for many geomechanical applications, assuming the interacting constituents occupy the whole control volume.

Extracting fluids from the pore space (Figure 1-1) in a reservoir or aquifer transfers the stress burden to the remaining solid framework, sometimes to such a degree that notable consolidation of the matrix occurs. This reduction in pore volume, in return, alters pore fluid pressures. Consequential fluid movement results as the fluid pressures equilibrate, and this coupled loop iterates. Pore fluid injection into or withdrawal from a reservoir translates to increasing or decreasing pore pressure.

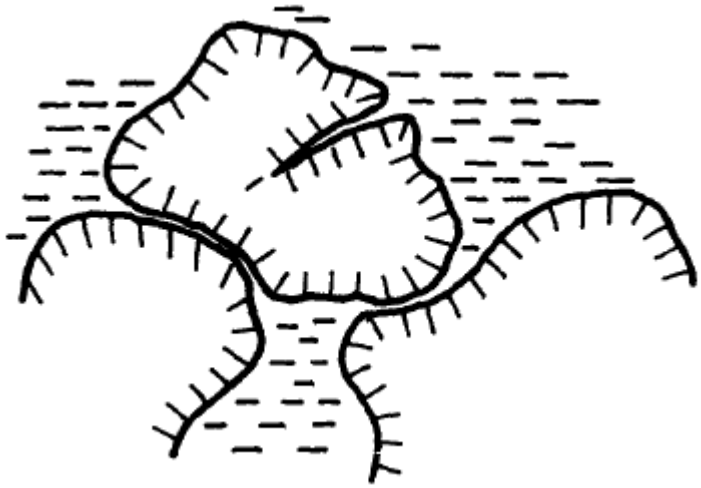

Figure 1-1. Schematic of general grain geometry. (from Biot (1962))

The effective stress law is the concept that this coupled behavior is governed by the combination of applied stress and pore pressure (Terzaghi, 1943). The effective stress is the calculated stress responsible for causing displacements. It represents the average stress carried by the grain contacts of the solid frame. Figure 1-2 depicts Terzaghi's description of the increase of effective stress as a result of pore pressure reduction and the effect on seismic velocities.

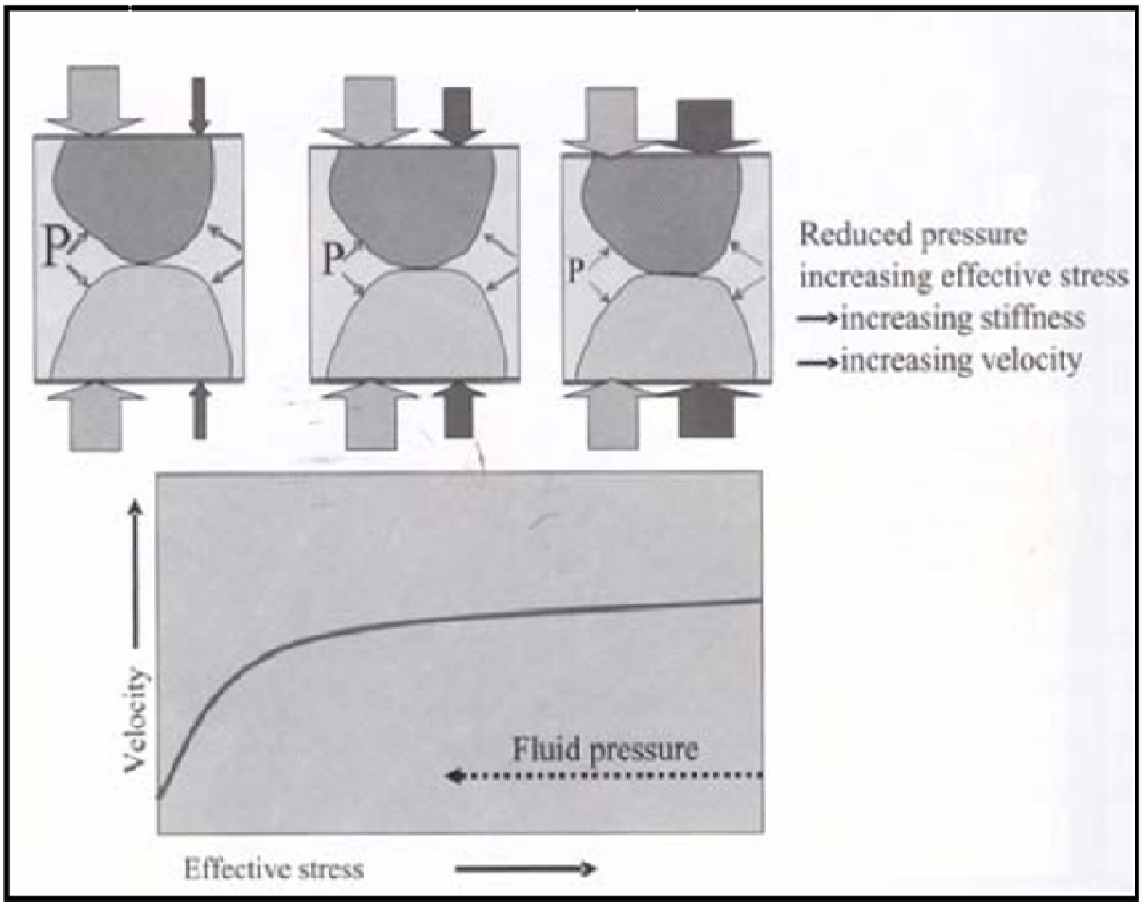

Figure 1-2. Schematic illustrating Terzaghi's (1943) description of effective stress and the effect on seismic velocities. (after Calvert (2005))

A conceptual understanding of the changing effective stresses resulting from reservoir contraction is shown in Figure 1-3. Porosity, fluid permeabilities, acoustic velocities are all sensitive to changes in effective stress, which may occur both proximal and distal from injecting or producing wells, depending upon the fluid flow and geomechanical properties of the reservoir and surrounding strata.

Analytical solutions to the effective stress distribution are usually limited to simple geometries and by assumptions of homogeneity and static pore pressure changes (Fuck, 2001; Fuck, 2007). In the last decade, a number of authors have developed separate numerical methods for handling geomechanics and reservoir flow (Dusseault et al., 2007), but integrating them in a single, consistent system is a challenge addressed in this thesis. Numerical modeling with finite elements provides a more flexible, realistic

approach that honors the linkage between geomechanics of the stress field and transient fluid flow, thus providing an integrated platform for time-lapse seismic analysis.

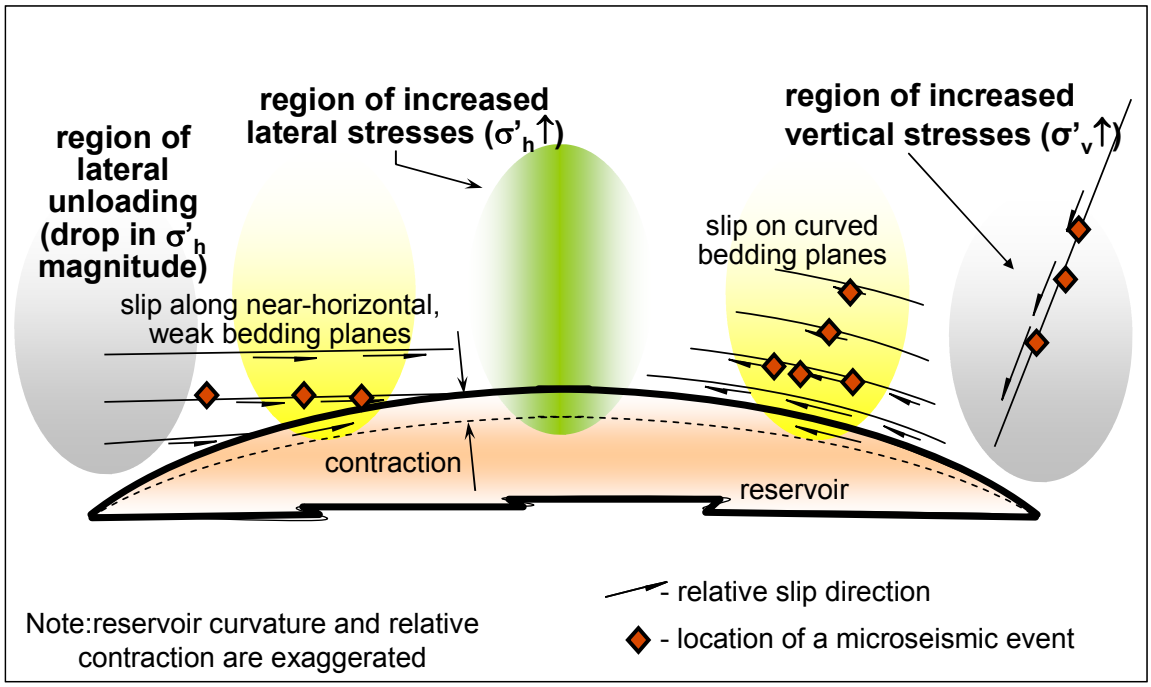

Figure 1-3. Reducing pore pressure leads to contraction of the reservoir and dilation in the overburden, resulting in significant effective stress (σ') changes outside of the reservoir. (modified after Dusseault (2007))

1.4 Notable Occurrences of Deforming Reservoirs

The problem of deformation (dilation and contraction) in reservoir production has a number of serious implications. At the pore scale, the reduction of pore volume and permeability may impede the ability to sustain hydrocarbon or groundwater production. Compaction may lead to notable subsidence at the ground surface or seafloor, resulting in damage to wells, platform foundations, and infrastructure. Subsidence may disturb agricultural, industrial, and urban activities and create operational hazards and economic liabilities. To illustrate the severity of compaction problems, the following case studies are presented in more detail.

1.4.1 Valhall Field

Valhall Field is an initially high porosity, overpressured Cretaceous chalk reservoir located in the central graben of the North Sea. Oil and gas production began in 1982. After only three years of primary production, the measured fluid pressures in the high porosity zones differed significantly from predictions of the loosely-coupled reservoir simulator, prompting further numerical and experimental studies (Ruddy et al., 1989). A 3-D elastic superposition model subsidence model was built and linked to the conventional reservoir flow simulator to provide seafloor subsidence predictions. Satellite surveys detected significant seafloor subsidence just four years into production of the field. Subsidence has been as high as 25 cm/year A subsequent drive mechanism study (Cook and Jewell, 1995) found that the compaction drive provided the majority (>70%) of primary depletion of hydrocarbon recoveries at Valhall Field.

1.4.2 Wilmington Field

Wilmington Field is an oil field located in Long Beach, California. In 1941, 0.4 m of production-induced subsidence was detected over an area of about 50 km^2. (Allen, 1972). By 1962, 9 m of subsidence was measured at the surface of a heavily pumped region (Figure 1-4). Displacements (both vertical and horizontal) caused damage to docks, pipelines, foundations, sewage systems, and roadways. A regional water-injection program went online in 1960, stabilizing subsidence in the most affected regions. Reversing large-scale subsidence is generally not feasible since closed pores are difficult to reopen. Damages and remediation totaled more than US$100 million at Wilmington Field.

Figure 1-4. Subsidence problems at Wilmington Field in Long Beach, California. (photo courtesy of the University of Wisconsin--Stevens Point Geology Department.)

1.4.3 Genesis Field

Genesis Field spans across three blocks of the Green Canyon in the Gulf of Mexico. The primary production targets are extremely unconsolidated sand intervals. Rapid compaction is reducing porosity and closing off permeability pathways in these intervals. Conversely, some shale intervals above the producing targets are evidently dilating due to elastic rebound. Considerable attention has been focused on the expression of this complex interaction revealed by time-lapse (4-D) seismic surveys (Duranti, 2005). The geomechanical effects on the 2002-1990 4-D seismic data are shown in Figure 1-5. The top of the N1 sand has shifted down by 2.4 ms and is interpreted as sand compaction. The arrow points to an anomaly above reservoir, which is interpreted as an elastic rebound of the shale section to reservoir compaction. The SB3 and SB2 panels show very small time shifts, thus supporting the idea that the dilation of the shales has a local pulse influence. The overall net shift of compaction offset by dilation is 2 ms upwards, as measured at the sea floor.

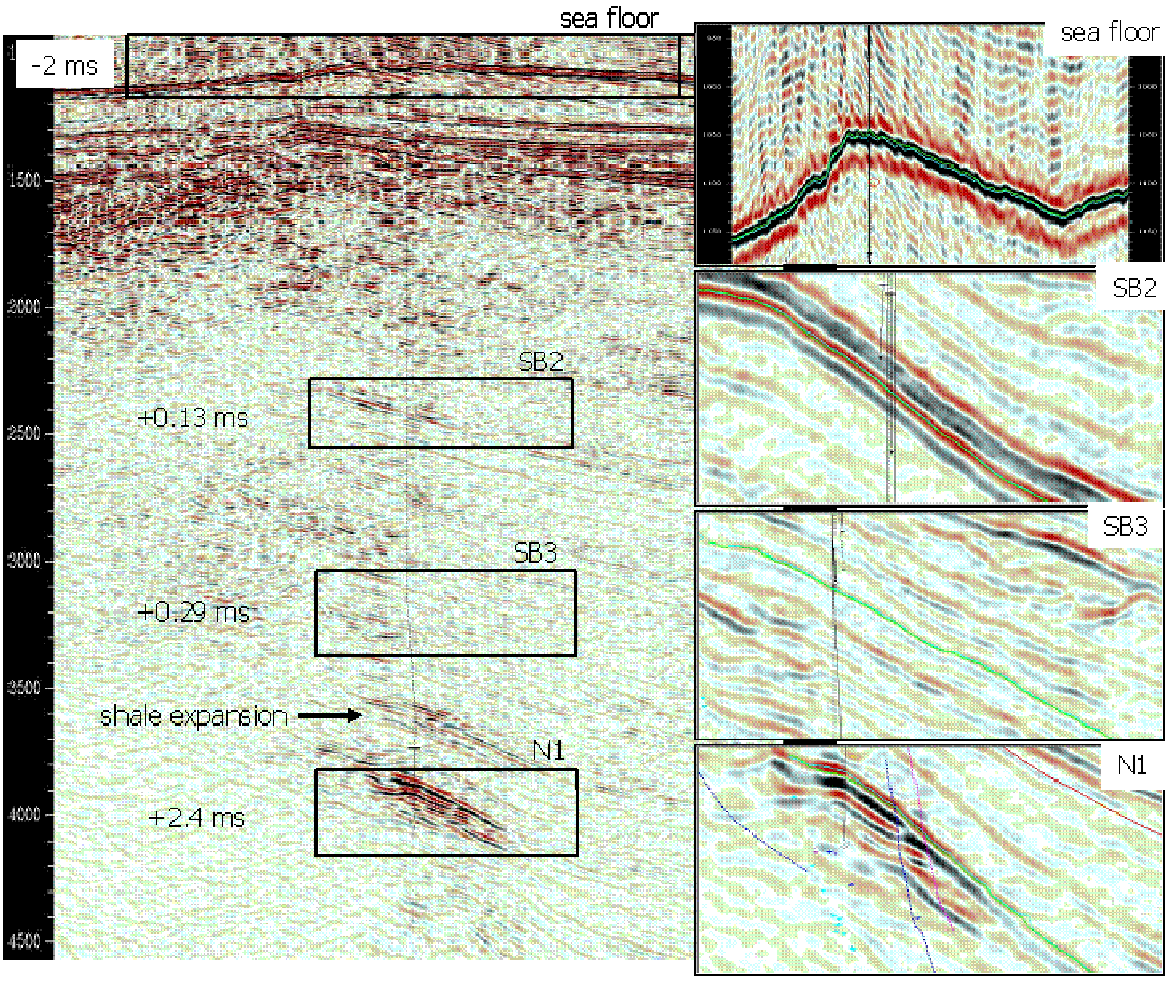

Figure 1-5. Expression of geomechanical effects on the Genesis Field time-lapse signal. Panel on the left is a section taken from the difference cube 2002-1990. The four zoomed sections on the right are taken from the baseline 1990 3D survey. (modified from Duranti, 2005)

1.4.4 Other Occurrences and Issues

The occurrence of compaction in hydrocarbon reservoirs is sometimes beneficial in that it may provide a considerable drive mechanism for production, as shown for Valhall Field. Similarly, compaction drive is responsible for a major percentage of oil production in the shallow Bolivar Coast fields in Lake Maracaibo. Yet, surface subsidence poses significant environmental problems in many places where municipal and agricultural water is pumped from shallower aquifers. In the United States (Figure 1-6), surface subsidence related to groundwater withdrawal has been documented at a

number of localities including Las Vegas NV, Savannah GA, Galveston TX, and the Santa Clara and San Joaquin Valleys in California (Chilingarian et al., 1996). Perhaps the most dramatic expression of widespread surface subsidence due to fluid withdrawal has occurred in Mexico City, which is underlain by weak, unconsolidated and saturated lacustrine clays, where displacements of more than 9 m have been recorded, especially in impervious areas allowing minimal groundwater recharge (Poland, 1984). Other localities experiencing notable surface subsidence include Suzhou City, China (Chen et al., 2003), the Po River Basin in Italy (Gambolati et al., 2000), and Bangkok, Thailand (Holzer and Johnson, 1985).

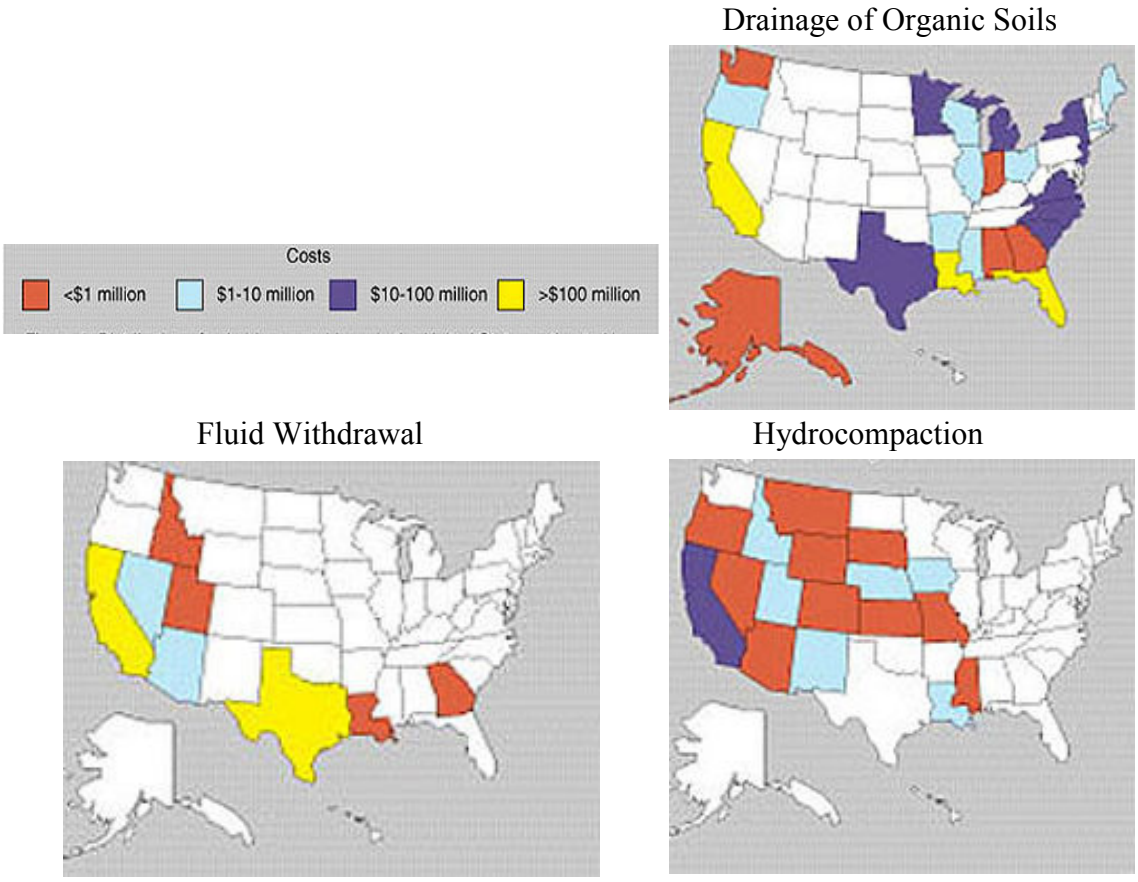

Figure 1-6. Subsidence costs (USD) in the United States (1991) as estimated by the National Academy of Sciences. (figures modified from NAS Report "Mitigating Losses from Land Subsidence in the United States (National Academy of Sciences, 1991)")

1.5 Recent Approaches and Challenges

Deformations dynamically alter porosity, pore compressibility, and pore fluid mobility, and may have significant impact on production. These deformations also affect the apparent time-shifts from seismic surveys of under- and over-burden. In most conventional standard reservoir simulators, the stress state of the field is either ignored or oversimplified by incorporating an effective rock compressibility scalar as the principal geomechanical link to the reservoir flow simulator, where rock compressibility is assumed to be a constant or a variable of fluid pressure. Key studies have shown that simulations using simply the rock compressibility scalar to describe the complete tensorial response of the stress state may give misleading or erroneous predictions (Settari and Price, 1984; Chen et al., 1995; Chin et al., 1998). In fact, not only has the rock compressibility term been shown to vary with the initial and boundary conditions (Gutierrez and Lewis, 1998), it is influenced by the dynamic variation of the stress state during depletion and injection (Sen and Settari, 2005). Clearly, mechanical deformations in stress-sensitive reservoirs tie strongly to economic and environmental considerations.

To determine how changes in the effective stress tensor relate to production and completion practices, recent attempts have been made to couple geomechanical modeling with reservoir fluid flow simulation to predict simultaneous changes in porosity and permeability resulting from injection or production (Gutierrez and Lewis, 1998; Lewis and Schrefler, 1998; Osorio et al., 1998; Settari and Walters, 1999; Fredrich et al., 2000; Minkoff et al., 2004; Sen and Settari, 2005; Tran et al., 2005a; Yin, 2006). However, such coupling is typically accomplished by running two separate numerical codes (one for time-dependent fluid flow and a second for quasistatic solid deformation). The codes are run in serial with the exchange of relevant parameters occurring at prescribed time intervals. This approach is the basis of the staggered-in-time loose coupling scheme summarized by Minkoff et al. (2004) and discussed in further detail in Chapter 3.

While the loose coupling approach offers the benefits of using industry-standard geomechanical models and reservoir simulators, it may not be the most suitable approach for reservoirs that have tight coupling between fluid flow and deformation in weak formations such as Valhall Field (previous section). Since nearly 60% of the earth's liquid fuel is in the form of viscous oils in weak sandstones (International Energy

Agency, 2005), clearly more work needs to be done to develop more robust, fully-coupled models that integrate the reservoir's dependencies on changes in pressure, stress, temperature, geochemistry, fracture rheology, and so forth, during all stages of production and injection. Although not all possible relevant phenomena are considered here, this thesis undertakes the current challenge of developing a unified platform capable of handling fluid flow, solid deformation, and seismic velocity responses at each time step.

1.6 Integration with Time-Lapse Seismics

Conventional evaluation of 4D seismics is generally focused on the differences in seismic attributes within the reservoir interval. However, recent studies (e.g., Hatchell and Bourne, 2005) have shown that time-lapse seismic changes resulting from production occur not only in the reservoir, but also notably in the overburden and volumes surrounding the pay zones. 4-D seismic studies are inherently sensitive to incongruous data acquisition geometries, inconsistencies in source and receiving instrumentation, and other sources of noise. Integrating coupled models of fluid flow and mechanical deformation affords valuable insights into subsurface compaction and changing geomechanical conditions. The closing of pore space during natural depletion has a significant impact on pore pressures and saturations, and consequently, elastic wave properties, namely velocities. Computed stresses relate to strains through nonlinear theory of elasticity (e.g., Thurston, 1974), which can then be used to model 4-D changes in seismic velocities.

Relying alone on the analysis of 4-D seismic data of compacting reservoirs may lead to misinterpretation and erroneous estimation of seismic-derived rock properties. The impact of using coupled geomechanical modeling to develop seismic properties is discussed in the literature (Settari and Walters, 1999; Olden et al., 2001; Vidal et al., 2002a; Vidal et al., 2002b; Minkoff et al., 2003; Tran et al., 2004; Herwanger and Horne, 2005; Tran et al., 2005b). For a high-porosity, low-permeability oil reservoir, Minkoff et al. (2004) have shown that incorporating time-dependent pressures, saturations, and porosities from geomechanically-coupled models into Gassmann's equations can result in seismic wave velocities and densities that are markedly different from those calculated

from fluid flow simulation alone. Similarly, Vidal et al. (2002a) have shown how coupled geomechanical models can be used to quantitatively evaluate the impact of gas production on seismic studies.

1.6.1 Modified Gassmann Methodology

Gassmann's (1951) equations relate the bulk moduli of a porous rock to the porosity and modulus of the fluid in the pore space. This methodology can be modified to predict time-lapse attributes from coupled pore fluid flow and geomechanical modeling. The approach is generalized as follows. Firstly, the field distribution of geomechanical and reservoir data (Young's Modulus, Poisson's ratio, fluid density, porosity, permeability, saturation, pore pressure, production rates, etc.) are incorporated the into a dynamically coupled poroelastic model. Secondly, time-dependent model outputs (i.e., pressure (p), saturations (S), and porosity (ϕ)) are converted into elastic rock parameters substitutions, as described by Gassmann. Given the composition of pore fluids, calculating effective bulk (K) and shear (G) moduli for the reservoir rock from the elastic moduli of the dry rock is given by the following equations:

$$G_{sat} = G_{dry} \tag{1.1}$$

$$\frac{K_{sat}}{K_{solid} - K_{sat}} = \frac{K_{dry}}{K_{solid} - K_{dry}} + \frac{K_{fluid}}{\phi(K_{solid} - K_{fluid})} \tag{1.2}$$

Typically, dry bulk and shear moduli are derived from well logs or rock physics measurements made on core plugs at different differential pressures. Several empirical relationships exist for making this transform (e.g., Hertz-Midlin). Most of these models assume hydrostatic stress conditions in the subsurface. The solid matrix bulk modulus, K_{solid}, may be estimated by an effective media model with a given mineral composition. The fluid modulus is a function of pressure and saturation. If the fluid is a gas, the modulus is obtained from a modified ideal gas law that corrects the disparity between atmospheric and reservoir conditions (e.g., Fluids Consortium FLAG software relations, 2005). The fluid mixture bulk modulus is calculated from a saturation-weighted average as follows:

$$K_{fluid}^{-1} = \frac{S_1}{K_1} + \frac{S_2}{K_2} + \frac{S_3}{K_3} \tag{1.3}$$

where the subscripts 1, 2, and 3 denote water, oil, and gas, respectively. Similarly, the total fluid density is given by the summation of the individual phase densities calculated from equations of state (Minkoff et al., 2004):

$$\rho_{fluid} = S_1\rho_1 + S_2\rho_2 + S_3\rho_3 \tag{1.4}$$

The concept of a "true porosity" is discussed in Minkoff et al. (1999). True porosity is intended to capture the stress-sensitive behavior as a function of volumetric strain, ε, and the unstressed initial porosity, ϕ_0:

$$\phi_{true} = 1 - (1 - \phi_0)e^{-\varepsilon} \tag{1.5}$$

Finally, application of Gassmann's equations and elastic parameter relationships gives the density (ρ), compressional (V_p) and shear (V_s) wave velocities at a given fluid saturation, pressure, porosity. The basic velocity relations for homogeneous, elastic, isotropic are (Mavko et al., 2003):

$$V_p = \left[\frac{K + \frac{4}{3}G}{\rho}\right]^{1/2} \tag{1.6}$$

$$V_s = \left[\frac{G}{\rho}\right]^{1/2} \tag{1.7}$$

The significance of using output generated from coupled flow and geomechanics in Gassmann's equations has been demonstrated (Fredrich et al., 2000; Minkoff et al., 2004). Porosity is assumed to be constant in most conventional applications of Gassmann equations. However, when pore fluid flow and geomechanics are coupled, porosity may change (even dramatically) with each timestep. Furthermore, pore pressures used as input loads in the geomechanics model result in stress changes that affect reservoir porosity and permeability. In turn, these new reservoir flow properties affect future calculations of pressure and saturation. The bulk fluid modulus and the dry moduli are all affected by pressure and saturation changes.

1.6.2 Nonlinear Anisotropic Elasticity Methodology

There are various rock physics models available for linking seismic velocity to effective stress. Because many subsurface rocks exhibit intrinsic anisotropy and are subject to nonhydrostatic stress fields, nonlinear anisotropic elasticity theory (Thurston and Brugger, 1964; Thurston, 1974; Sarkar et al., 2003; Prioul et al., 2004) provides a suitable framework for describing the effective stress tensor as a function of a 3-D stress field and for predicting seismic velocities of both compressional and shear waves in any direction for any particular 3-D stress state. This approach has the advantage of directly linking shear wave velocities with horizontal stresses. Also, it is not limited by the assumptions of the empirical velocity-stress models that link compressional wave velocity in isotropic rocks to hydrostatic stress. In the past decade, estimates of the independent third-order stiffness constants (c111, c112, c123) are available not only from lab measurements on cores (Prioul et al., 2004), but also from in situ multimode borehole acoustics, making downhole calibrations possible (e.g., Sinha and Winkler, 1999). Further details of the nonlinear elastic continuous-medium approach, coupled to multi-phase fluid flow, are included in Section 4.6 and in the Appendices.

1.6.3 A Numerical Example at Belridge Field

The data for this example are based on a study of the Belridge field, located near Bakersfield, California, with an estimated 5×10^8 m^3 original oil-in-place. Production has been limited in certain diatomite zones. Diatomite is approximately 15 times weaker than typical sandstone. Porosities in these zones range from 45% to 70%, but permeabilities are very low (~0.1 mD). With the advent of hydraulic fracturing in the 1970s, production started rising. However, substantial subsidence, up to 6 meters, occurred as a result of fluid withdrawal in the high porosity diatomite, causing numerous well failures (Minkoff et al., 2004).

Minkoff et al. (1999) first proposed a modeling experiment based on the weakest zone of Belridge field diatomite. The vertical sides of the model are to be constrained from movement normal to the boundary. The prescribed in situ stress state at t=0 is vertical overburden loading. The horizontal principal stresses (x and y) are calculated by multiplying the vertical principal stress (z) by empirical factors of 0.65 and 1.20,

respectively (Fredrich et al., 2000). The reservoir has four production wells, completed to various depths, to be placed at the corners of the 105.5 m x 105.5 m x 13.4 m model domain. The initial pore pressure is 3.76 MPa, water saturation 35%, and porosity 50%.

Figure 1-7 represents the von Mises stress distribution calculated after 10 years of production. The obvious difference in stress at each well is due to the different well production schedules and completion depths. Maximum vertical subsidence reaches nearly 64 cm. Incidentally, final porosities drop from 50% to 48% near the wells.

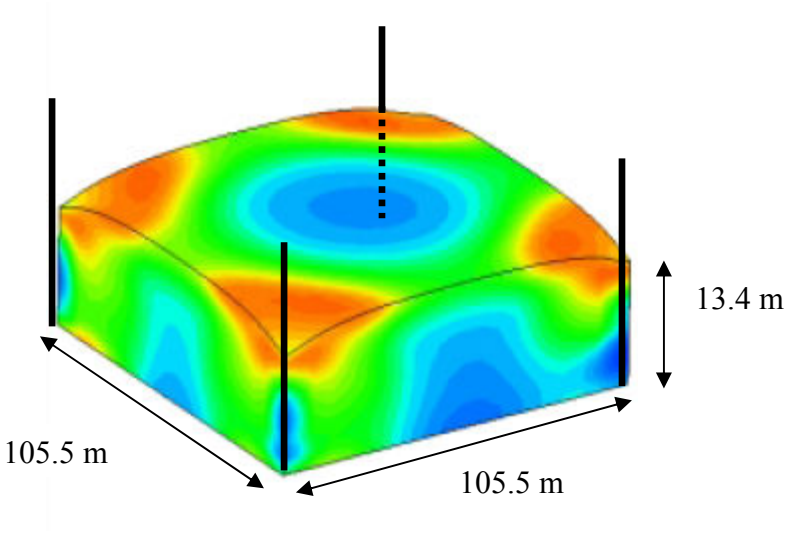

Figure 1-7. von Mises stress for the Belridge field numerical experiment after 10 years of production, considering coupled mechanical deformation and flow modeling. Range: nominal (cooler colors) to 1.15MPa (warmer colors). (data from Minkoff et al. (1999))

Gassmann's equations are used to compute time-lapse seismic velocities. In the first five years simulated by the coupled model, compressional wave velocity drops by 350 m/s near the wells, due to gas coming out of solution. The seismic wave velocity discrepancies, between flow simulator-alone versus multiphysics coupling, are shown in Figure 1-8. They are significant enough to be detectable in real field data.

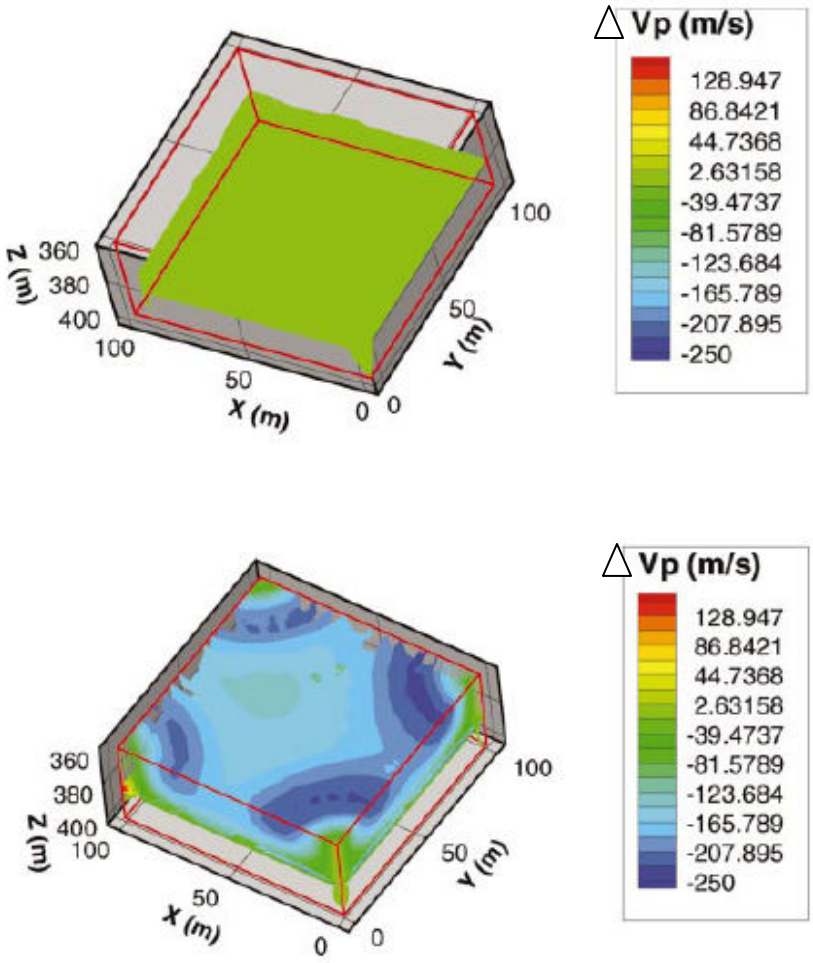

Figure 1-8. (Top) Difference in compressional wave velocity between flow simulation alone and coupled flow and geomechanics, with only porosity changing dynamically. (Bottom) Difference in compressional wave velocity between flow simulation alone and coupled flow and geomechanics with both porosity and permeability changing dynamically. Both figures are at five years of production. (data from Minkoff et al. (2004))

1.7 Aims and Objectives of this Thesis

This work investigates the dynamic, multiphysical linkages between fluid flow and geomechanical deformation and seismic velocity responses. The aim of this thesis is to extend the loosely-coupled approach of reservoir geomechanics to the next logical step by implementing, developing and testing a fully coupled geomechanical model where the equations governing fluid flow and geomechanics and time-lapse seismics are solved

simultaneously within the framework of the finite element method. Such a unified platform stands to contribute to the overall understanding of the mutual interdependency the pertinent flow and geomechanical parameters throughout the lifetime of reservoir production and injection. This work is intended to be of interest in the disciplines dealing with, but not limited to, well testing, surface subsidence, and enhanced hydrocarbon recovery projects in weak, unconsolidated, or otherwise stress-sensitive formations. The formulation developed in the thesis may be adapted and calibrated to a variety of production scenarios. The primary goal is to provide a better understanding of reservoir dynamics that prevent steady production rates and disturb infrastructure.

1.8 Thesis Outline

This chapter has provided a brief history and introduction to the role of geomechanics in geophysical and petroleum engineering studies. The physical and mathematical background of modeling continuum mechanics is addressed in Chapter 2. Special emphasis will be given to comparing the theoretical poroelastic underpinnings to the default code found in a commercial finite element modeling package, and how to remedy the discrepancies. In Chapter 3, different computation schemes for coupling the flow and geomechanical components are discussed on the basis of accuracy, ease of implementation, efficiency, and code compatibility. Chapter 4 presents the results of several representative numerical simulations, selected to test validity, applicability, usefulness of fully-coupled geomechanical approach. The details of finite element matrices and a non-linear formulation are presented in the appendices. Conclusions and recommendations for future work in this area are noted in Chapter 5.

CHAPTER 2. THEORETICAL BACKGROUND OF MODELING PHENOMENOLOGY

The basis for modeling poromechanics is founded on the principles defining fluid-structure interaction. Extracting fluids from the pore space in a reservoir or aquifer transfers the additional stress burden to the remaining solid rock frame, sometimes to such a degree that measurable, irreversible compaction of the matrix occurs. This reduction in pore volume, in return, alters pore fluid pressures. Fluid pressure equilibration causes secondary fluid movement, providing feedback to the coupled fluid-structure loop. The governing equations that describe this dynamic interaction between fluid flow and stress are formulated on the basis of Biot's coupled poroelasticity theory (Biot, 1941; Biot, 1955). The motion of fluid flow in porous material is described by Darcy's law. The structural deformations are governed by the constitutive equations of linear elasticity. The fluid-structure interaction problem is reduced to partial differential equations, for ease of numerical implementation and added flexibility in regards to modifying source and loss terms. In this chapter, the constitutive relations and governing equations of the poroelastic models are described, laying the framework for numerical implementation and application in subsequent sections of this thesis.

2.1 Constitutive Relations

Constitutive models provide the essential link between the macroscopic level and the microscopic level continuum properties and complete the set of governing equations describing the poroelastic response to a change in stress state. Macroscopic constitutive theory assumes that at the micro-level, the material is homogeneous, and consequently, the stain field is homogenous and stress is uniform surrounding each point in the solid. Further, the focus of this thesis is constrained to isothermal, linear poroelasticity.

The basis for Biot's poroelastic theory for a fluid-filled porous material is two linear constitutive equations between four poroelastic variables: field stress (σ_{ij}), field strain (ε_{ij}), fluid content increment (ζ), and fluid pressure (p). Mathematical

representations of poroelastic theory are represented differently in geomechanics, petroleum engineering, and hydrogeology. The convention used in this work takes stress and strain to be positive in structural expansion (i.e., tension), fluid content increment to be positive for fluid added to storage in the control volume, and fluid pressure to be positive if greater than atmospheric pressure. Hence, fluid injection into a jacketed poroelastic sample would result in both a positive structural stress as the matrix tries to expand and a positive pore pressure as the interstitial fluid is compressed. In the simplest 1-D formulation, the two linear constitutive equations express ε and ζ as functions of σ and p as (cf. Detournay and Cheng, 1993; cf. Wang, 2000):

$$\varepsilon = a_{11}\sigma + a_{12}p \tag{2.1}$$

$$\zeta = a_{21}\sigma + a_{22}p \tag{2.2}$$

By imposing various constraints on an elementary control volume, the poroelastic coefficients (a_{ij}) are defined as ratios of field variables (K, H, R), where K is the drained bulk modulus, H is the reciprocal of the poroelastic expansion coefficient, and R is the Biot modulus. Biot (1941) demonstrated a potential energy reciprocity through which only three proportionality coefficients, drained compressibility ($a_{11}=\delta\varepsilon/\delta\sigma|_{\Delta p=0} \equiv 1/K$), poroelastic expansion ($a_{12}=\delta\varepsilon/\delta p|_{\Delta\sigma=0}=a_{21}=\delta\zeta/\delta\sigma|_{\Delta p=0} \equiv 1/H$), and unconstrained specific storage ($a_{22}=\delta\zeta/\delta p|_{\Delta\sigma=0} \equiv 1/R$), are needed to fully describe the poroelastic response to an applied stress causing volumetric deformation. A constant increment of fluid signifies an undrained condition, a constant pore pressure signifies a drained condition, constant stress signifies no change in external stress, and constant strain signifies no change in external displacement. Three additional coefficients—Skempton's coefficient ($-\delta p/\delta\sigma|_{\Delta\zeta=0} \equiv R/H=B$), Biot-Willis coefficient ($\delta\zeta/\delta p|_{\Delta p=0} \equiv K/H=\alpha$), and constrained specific storage ($\delta\zeta/\delta p|_{\Delta\varepsilon=0} \equiv \alpha(1-\alpha B)/(KB)=S_\varepsilon$)—can be derived from the three previously defined constants. When shear stresses (τ) are present, a fourth independent constant, either the shear modulus or Poisson's ratio, is needed to fully describe the poroelastic constitutive equations.

For purposes in this thesis, the constitutive relations need to be solved for stress since stress appears in the elemental force balance equation, $-\nabla\cdot\boldsymbol{\sigma}=\mathbf{F}$, which is discussed

in the next section. Eqns. 2.1 and 2.2 can be manipulated as needed by pairing independent and dependent variables. A mixed stiffness formulation can be developed such that strain and pore pressure are independent variables and stress is paired with fluid content increment as dependent variables:

$$\sigma = K\varepsilon - \alpha p \tag{2.3}$$

$$\zeta = \alpha\varepsilon + \frac{\alpha(1-\alpha B)}{KB} p \tag{2.4}$$

The constrained specific storage coefficient is defined such that

$$S_\varepsilon = \frac{\alpha}{K_u B} = \frac{\alpha(1-\alpha B)}{KB} \tag{2.5}$$

where the undrained bulk modulus is $K_u \equiv \delta\sigma/\delta\varepsilon|_{\Delta\zeta=0} = K/(1-\alpha B)$. Eqn. 2.4 can, therefore, be rewritten as:

$$\zeta = \alpha\varepsilon + S_\varepsilon p \tag{2.6}$$

At the macroscopic stress-strain scale, the standard linear elastic relationships (Mavko et al., 2003),

$$K = \frac{E}{3(1-2\upsilon)} \tag{2.7}$$

and

$$E = \frac{2G}{3(1+\upsilon)} \ , \tag{2.8}$$

relate the static elastic constants E (Young's Modulus), G (shear modulus), and ν (Poisson's ratio) to the poroelastic bulk modulus, K.

So far, all the components for a 1-D poroelastic analysis have been identified. The next step is developing the 2-D, 2-D axial symmetry, and 3-D formulation. Seven linear constitutive equations are needed to completely describe a general anisotropic state of stress: six for the tensorial quantity (σ_{ij} or ε_{ij}) and one for the scalar quantity (p or ζ). Using principal coordinates (subscripts $_{1,2,3}$ where $\sigma_{ij}=0$ and $\varepsilon_{ij}=0$ for $i \neq j$), the set of seven constitutive equations needed to fully describe the general anisotropic case are reduced to four equations for four dependent variables formulated in terms of four independent variables:

$$\varepsilon_1 = \frac{1}{E}\sigma_1 - \frac{\nu}{E}\sigma_2 - \frac{\nu}{E}\sigma_3 + \frac{\alpha p}{3K} \tag{2.9}$$

$$\varepsilon_2 = -\frac{\nu}{E}\sigma_1 + \frac{1}{E}\sigma_2 - \frac{\nu}{E}\sigma_3 + \frac{\alpha p}{3K} \tag{2.10}$$

$$\varepsilon_3 = -\frac{\nu}{E}\sigma_1 - \frac{\nu}{E}\sigma_2 + \frac{1}{E}\sigma_3 + \frac{\alpha p}{3K} \tag{2.11}$$

$$\zeta = -\frac{\alpha}{3K}(\sigma_1 + \sigma_2 + \sigma_3) + \frac{p}{R} \tag{2.12}$$

Eqns. 2.9-2.12 are similar to those found standard elasticity texts, with the important addition of pore pressure term to account for *poro*elastic behavior. The equations can be cast in general coordinates and resolved for normal and shear stresses, and the shear modulus using Eqn. 2.7:

$$\sigma_{xx} = 2G\varepsilon_{xx} + 2G\frac{\nu}{1-2\nu}(\varepsilon_{xx} + \varepsilon_{yy} + \varepsilon_{zz}) - \alpha p \tag{2.13}$$

$$\sigma_{yy} = 2G\varepsilon_{yy} + 2G\frac{\nu}{1-2\nu}(\varepsilon_{xx} + \varepsilon_{yy} + \varepsilon_{zz}) - \alpha p \tag{2.14}$$

$$\sigma_{zz} = 2G\varepsilon_{zz} + 2G\frac{\nu}{1-2\nu}(\varepsilon_{xx} + \varepsilon_{yy} + \varepsilon_{zz}) - \alpha p \tag{2.15}$$

$$\tau_{xy} = 2G\varepsilon_{xy} \tag{2.16}$$

$$\tau_{xz} = 2G\varepsilon_{xz} \tag{2.17}$$

$$\tau_{yz} = 2G\varepsilon_{yz} \tag{2.18}$$

The seventh constitutive equation is similar to that of Eqn. 2.6, except ε is expressed as the sum of the three normal strains, or volumetric strain (ε_{kk}):

$$\zeta = \alpha\varepsilon_{kk} + S_\varepsilon p \tag{2.19}$$

2.2 Governing Equations

The poroelastic governing equations for fully saturated pore fluid flow are based on force equilibrium equations and conservation of fluid mass as applied to Darcy's law. The equations are bidirectionally coupled because pore pressure or increment of fluid content appears in the force equilibrium equations, and because stress or volumetric strain appears in the poroelastic fluid continuity equations. The fundamental requirement behind the linear poroelastic problem is that mechanical equilibrium equations and the

fluid continuity equation be satisfied simultaneously. In real systems, dynamic waves transmit stress changes over a certain period of time, as simulated by a wave propagation term (cf. Dvorkin and Nur, 1993). In this thesis, however, a quasistatic approach is developed to satisfy mechanical equilibrium at each time step, and to account for time-dependent fluid movement due to the delaying effects of finite permeability and storage response. Special attention is given to casting initial and boundary conditions for this quasistatic poroelastic problem.

2.2.1 Force Equilibrium Equations

Assuming the validity of Cauchy's principle, the force equilibrium equations are developed by analyzing the total stress (applied force divided by the unit area of solid grains and pore fluid) exerted on a unit bulk volume of rock. If a change in stress state or pore pressure is instantaneously applied to a poroelastic body, displacements and pore pressure within each Representative Elementary Volume (REV) adjust instantaneously to maintain a state of internal force-displacement equilibrium. The normal (σ) and shear (τ) components of the stress tensor are illustrated on an REV in Figure 2-1.

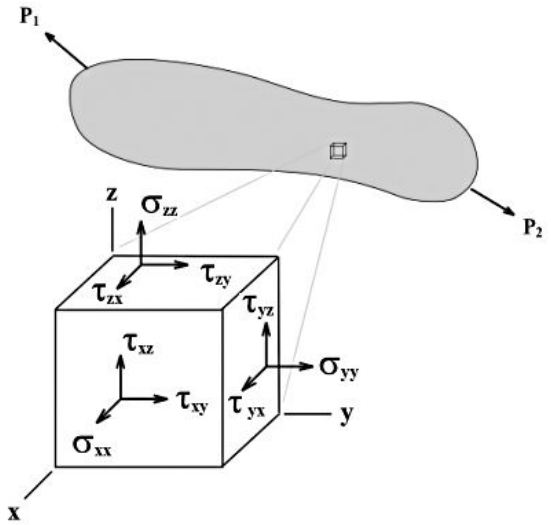

Figure 2-1. Normal (σ) and shear (τ) components of the stress tensor at an internal point P, shown on an infinitesimal REV. (after Wang, 2000)

Furthermore, applied stresses on the faces of an REV must be in static translational and rotational equilibrium such that the stress tensor (σ_{ij}) is symmetric ($\tau_{yx} = \tau_{xy}$, $\tau_{zx} = \tau_{xz}$, and $\tau_{zy} = \tau_{yz}$).

$$\sigma_{ij} = \begin{bmatrix} \sigma_{xx} & \tau_{xy} & \tau_{xz} \\ \tau_{yx} & \sigma_{yy} & \tau_{yz} \\ \tau_{zx} & \tau_{zy} & \sigma_{zz} \end{bmatrix} \tag{2.20}$$

Using principle coordinates, the REV can be aligned such that the shear strains are zero.

$$\sigma_{ij} = \begin{bmatrix} \sigma_{xx} & 0 & 0 \\ 0 & \sigma_{yy} & 0 \\ 0 & 0 & \sigma_{zz} \end{bmatrix} \tag{2.21}$$

Assuming insignificant accelerations and summing the net forces in each principal direction, the following force-displacement equilibrium equations are derived (cf. Means, 1976; cf. Detournay and Cheng, 1993; cf. Wang, 2000):

$$\frac{\partial \sigma_{xx}}{\partial x} + \frac{\partial \tau_{yx}}{\partial y} + \frac{\partial \tau_{zx}}{\partial z} + F_x = 0 \tag{2.22}$$

$$\frac{\partial \tau_{xy}}{\partial x} + \frac{\partial \sigma_{yy}}{\partial y} + \frac{\partial \tau_{zy}}{\partial z} + F_y = 0 \tag{2.23}$$

$$\frac{\partial \tau_{xz}}{\partial x} + \frac{\partial \tau_{yz}}{\partial y} + \frac{\partial \sigma_{zz}}{\partial z} + F_z = 0 \tag{2.24}$$

where **F** (F_x, F_y, F_z) is the body force per unit bulk volume. In the absence of applied loads, **F** is just the weight force due to gravity, so **F**=(0,0,-ρg). In engineering notation, the three force-displacement equilibrium equations are represented as

$$\sum_{i=1}^{3} \frac{\partial \sigma_{ij}}{\partial x_i} = F_i \quad \text{for all j} \tag{2.25}$$

For very small deformations, the strains can be defined equivalently with index notation in terms of derivatives of displacement, $\vec{u}$:

$$\varepsilon_{ij} = \frac{1}{2}\left(\frac{\partial u_i}{\partial x_j} + \frac{\partial u_j}{\partial x_i} \right) \tag{2.26}$$

In standard notation, the volumetric strain is the sum of the longitudinal strains as expressed by the divergence of displacement

$$\varepsilon = \varepsilon_{kk} = \varepsilon_{xx} + \varepsilon_{yy} + \varepsilon_{zz} = \frac{\partial u}{\partial x} + \frac{\partial \mathrm{v}}{\partial y} + \frac{\partial w}{\partial z} \tag{2.27}$$

where *u*, v, and *w* are the components of displacement in the x, y, and z directions, respectively. Applying these definitions of the strain components and substituting the

constitutive equations for stress components from the previous section (Eqns. 2.13-2.15) into the force-displacement equations (Eqns. 2.22-2.24) will yield three coupled partial differential equations relating, in mechanical equilibrium, six quantities of strain to pore pressure and the body force. After substitutions, Eqns. 2.22-2.24 become the structural poroelastic equations:

$$G\nabla^2 u + \frac{G}{1-2\nu}\left[\frac{\partial^2 u}{\partial x^2} + \frac{\partial^2 \mathrm{v}}{\partial x \partial y} + \frac{\partial^2 w}{\partial x \partial z}\right] + F_x = \alpha \frac{\partial p}{\partial x} \tag{2.28}$$

$$G\nabla^2 v + \frac{G}{1-2\nu}\left[\frac{\partial^2 u}{\partial y \partial x} + \frac{\partial^2 \mathrm{v}}{\partial y^2} + \frac{\partial^2 w}{\partial y \partial z}\right] + F_y = \alpha \frac{\partial p}{\partial y} \tag{2.29}$$

$$G\nabla^2 w + \frac{G}{1-2\nu}\left[\frac{\partial^2 u}{\partial z \partial x} + \frac{\partial^2 \mathrm{v}}{\partial z \partial y} + \frac{\partial^2 w}{\partial z^2}\right] + F_z = \alpha \frac{\partial p}{\partial z} \tag{2.30}$$

Traditional equations of elasticity (e.g. Timoshenko and Goodier, 1951) are equivalent to these poroelastic equations, except for the addition of the pore pressure gradient term on the right-hand side, which has units identical to those of a body force.

2.2.2 Fluid Flow Relations

Flow in porous material is governed by Darcy's Law (1856), an energy transport equation, which relates fluid flow rates to pressure gradients and elevation gradients:

$$\vec{q} = -\frac{k}{\mu}\vec{\nabla}(p + \rho_f g z) \tag{2.31}$$

where $\vec{q}$ is fluid flux, k is the intrinsic permeability, μ is the viscosity, ρ_f is the fluid density, g is the acceleration of gravitational, and z is the elevation potential. Since inertial terms are ignored in the equation of pore fluid motion, the relative seepage velocity is expressed as an average linear velocity between the fluid and the solid matrix displacements, $\vec{}$ f and $\vec{}$ s, respectively:

$$\vec{v} = \frac{1}{\phi}\vec{q} = \frac{\partial \vec{}\,^{\mathrm{f}}}{\partial t} - \frac{\partial \vec{}\,^{\mathrm{s}}}{\partial t} \tag{2.32}$$

where ø is the effective (non-occluded) porosity. Fluid exchange within an REV can be due to deformation, fluid pressure change, or the presence of a source (injection) or a sink (well). Defined terms of an equation of continuity, Biot and Willis (1957) express the increment of fluid content as

$$\zeta = -\phi\vec{\nabla}\cdot(\vec{u}_f - \vec{u}_s) \tag{2.33}$$

The porosity term drops out of this fluid continuity equation by taking the time derivative and substituting in the relative seepage velocity:

$$\frac{\partial\zeta}{\partial t} = -\phi\vec{\nabla}\cdot(\frac{1}{\phi}\vec{q}) = -\vec{\nabla}\cdot\vec{q} \tag{2.34}$$

or, expressed in terms of an external volumetric fluid source distribution function, Q:

$$Q = \frac{\partial\zeta}{\partial t} + \vec{\nabla}\cdot(\vec{q}) = -\vec{\nabla}\cdot\vec{q} \tag{2.35}$$

Now, substituting in Darcy's law for the fluid flux, the result is

$$Q = \frac{\partial\zeta}{\partial t} + \vec{\nabla}\cdot(-\frac{k}{\mu}\vec{\nabla}(p + \rho_f gz)) \tag{2.36}$$

Finally, the time derivative of the last constitutive relation between fluid content increment and strain and pressure (Eqn. 2.19) is substituted to give the poroelastic fluid flow governing equation

$$Q = \alpha\frac{\partial}{\partial t}\varepsilon_{kk} + S_\varepsilon\frac{\partial p}{\partial t} + \vec{\nabla}\cdot(-\frac{k}{\mu}\vec{\nabla}(p + \rho_f gz)) \tag{2.37}$$

This form of the equation is described in terms of volumetric strain as the mechanical variable and pore pressure as the fluid variable. Although other permutations are possible, this form of the equation closely aligns with the formulation used in Comsol Multiphysics 3.3a, a commercial finite element modeling environment (Section 2.3).

2.2.3 Boundary and Initial Conditions

Because the pore pressure variable p in the constitutive equations is defined as the additional pressure relative to hydrostatic conditions, the boundary and initial conditions of the problem domain must be cast in terms of excess pore pressure. Hydrostatic pressure is the pressure due to the weight of the overlying fluid column. The difference between the total pressure and the hydrostatic pressure is the excess pressure:

$$p_{total} - [\rho_f g(z_{datum} - z)] = p_{excess} \tag{2.38}$$

Specifying the pore pressure (or changes in hydraulic head) and the stress condition at a boundary is typical in many modeling applications. Specifying a drained boundary would mean setting p=0. Specifying an impermeable ("no-flow") boundary or

symmetry plane would mean setting ζ=0. Since mechanical stresses are assumed to be transmitted instantaneously, the slower fluid response can be set as undrained. For example, a suddenly applied boundary load would mean setting ζ=0 and solving for the mechanical equilibrium equations for the excess pore pressure distribution.

2.3 Poroelastic Modeling in Comsol Multiphysics 3.3a

The Comsol Multiphysics 3.3 finite element modeling package simulates the coupling of various physical interactions. The software is capable of handling porous fluid flow (e.g. Darcy's Law application mode). The software is also capable of handling the solid phase of classic elasticity problems. Typically, the user chooses one or combines two or more Physics Application Modes. Unfortunately, at the time of this publication, Comsol provides no specific mode nor coupled modes for modeling poroelastic behavior. In other words, porous materials with fluid-filled pores and elastic frames cannot be modeled with any pre-existing coupling. This is due in part to the fact that the poroelastic problem deals not only with the classical multiphysics coupling (cf. Section 2.1 on Constitutive Relations), but there also exists a very strong coupling with the equations of equilibrium. Fortunately, Comsol enables the user to modify or add to the partial differential equation systems. This is by no means a trivial task, but it does give the user added flexibility and the ability to verify the programmed code. Often the code in some commercial modeling environments is contained within a "black box" and is not easily verifiable or customizable.

By default, the structural equations ("plane strain mode") in the Comsol Multiphysics 3.3 finite element modeling package follow the classical elasticity derivation, in terms of shear moduli:

$$G\nabla^2 u + \frac{G}{1-2\nu}\left[\frac{\partial^2 u}{\partial x^2} + \frac{\partial^2 \mathrm{v}}{\partial x \partial y} + \frac{\partial^2 w}{\partial x \partial z}\right] + F_x = 0 \tag{2.39}$$

$$G\nabla^2 v + \frac{G}{1-2\nu}\left[\frac{\partial^2 u}{\partial y \partial x} + \frac{\partial^2 \mathrm{v}}{\partial y^2} + \frac{\partial^2 w}{\partial y \partial z}\right] + F_y = 0 \tag{2.40}$$

$$G\nabla^2 w + \frac{G}{1-2\nu}\left[\frac{\partial^2 u}{\partial z \partial x} + \frac{\partial^2 \mathrm{v}}{\partial z \partial y} + \frac{\partial^2 w}{\partial z^2}\right] + F_z = 0 \tag{2.41}$$

Eqns. 2.39-41 do not account for poroelastic effects contributed by the pore pressure gradient term, $\alpha(\vec{\nabla}p)$ (cf. Eqns. 2.28-2.30). The pore pressure gradient term is equivalent to a body force.

The governing equation found in Comsol's Darcy's Law application mode is a pure pore pressure formulation:

$$Q = S_\varepsilon \frac{\partial p}{\partial t} - \vec{\nabla} \cdot (\frac{k}{\mu} \vec{\nabla}(p + \rho_f g D)) \tag{2.42}$$

All terminology is the same as those defined in the previous sections, except for the *D* term which is equivalent to Darcy's elevation potential, *z* (Eqn. 2.31). By default, the strain-displacement relations (Eqns. 2.26 and 2.27) are not included in Comsol's formulation. To be equivalent to the full poroelastic fluid flow governing equation (Eqn. 2.37), an additional loss term containing a time rate change in strain, $-\alpha \frac{\partial}{\partial t}(\vec{\nabla} \cdot \vec{u})$, must to be amended to Comsol's volumetric fluid source function, *Q*:

$$Q - \alpha \frac{\partial}{\partial t}(\vec{\nabla} \cdot \vec{u}) = S_\varepsilon \frac{\partial p}{\partial t} - \vec{\nabla} \cdot (\frac{k}{\mu} \vec{\nabla}(p + \rho_f g D)) \tag{2.43}$$

2.4 Summary of Equations and Discussion

Definitions, constitutive relations, and coupled governing equations cast with relevant initial and boundary conditions provide a framework for approaching a large variety of geomechanically coupled poroelastic problems. Following a discussion of the relevant constitutive relations, a set of poroelastic equations have been posed to describe the two-way coupling between deformation and fluid flow.

Structural Equilibrium

$$G\nabla^2 u + \frac{G}{1-2\nu}\left[\frac{\partial^2 u}{\partial x^2} + \frac{\partial^2 \mathrm{v}}{\partial x \partial y} + \frac{\partial^2 w}{\partial x \partial z}\right] + F_x = \alpha \frac{\partial p}{\partial x} \tag{2.44}$$

$$G\nabla^2 v + \frac{G}{1-2\nu}\left[\frac{\partial^2 u}{\partial y \partial x} + \frac{\partial^2 \mathrm{v}}{\partial y^2} + \frac{\partial^2 w}{\partial y \partial z}\right] + F_y = \alpha \frac{\partial p}{\partial y} \tag{2.45}$$

$$G\nabla^2 w + \frac{G}{1-2\nu}\left[\frac{\partial^2 u}{\partial z \partial x} + \frac{\partial^2 \mathrm{v}}{\partial z \partial y} + \frac{\partial^2 w}{\partial z^2}\right] + F_z = \alpha \frac{\partial p}{\partial z} \tag{2.46}$$

Fluid Flow

$$Q = \alpha \frac{\partial}{\partial t} \varepsilon_{kk} + S_{\varepsilon} \frac{\partial p}{\partial t} + \vec{\nabla} \cdot (-\frac{k}{\mu} \vec{\nabla}(p + \rho_f g z)) \tag{2.47}$$

For purposes of verification, care has been taken in formulating the full poroelastic equations parallel to those found in commercial numerical modeling software. In both structural equilibrium and fluid flow, the poroelastic equations and those found in Comsol Multiphysics are essentially equivalent, except for poroelastic source terms containing the Biot-Willis coefficient. For the fluid-flow continuity equation, the strain-displacement term,

$$-\alpha \frac{\partial}{\partial t} (\vec{\nabla} \cdot \vec{u}), \tag{2.48}$$

must be added to the default Comsol volumetric fluid source term, Q. Similarly, for structural equilibrium, a pore pressure gradient term,

$$-\alpha (\vec{\nabla} p), \tag{2.49}$$

must be added to the default Comsol body force term, **F**.

In general, the built-in PDE-based solvers in Comsol's packages are considered quite robust and are well tested. However, the built-in equation systems linking the various application modes (e.g., Darcy mode and plane-strain mode) are relatively new and, thus, may contain omissions, bugs, or improper assumptions. As with any modeling package, the validity and applicability of the built-in equation systems should be verified before undertaking a modeling project. The advantage of Comsol's Multiphysics package is that it allows the user to verify, unlock, and modify the built-in equation systems if necessary. Because Comsol Multiphysics was built to interface with Matlab, a popular matrix-oriented data analysis program, the equations in Comsol can be modified using standard Matlab expressions. Such a task in other commercial reservoir simulators is often very cumbersome, if not impossible for the end user.

Other commercial reservoir modeling packages were considered for implementing geomechanically coupled reservoir characterization studies in this thesis. One such package is Steam, Thermal, and Advanced Processes Reservoir Simulator (STARS) available from the Computer Modeling Group (CMG). The advantage of this simulator is that it was built specifically to simulate large-scale reservoir fluid flow studies. However, the program's code integrates geomechanical responses to fluid flow through a

loosely coupled algorithm that is not transparent to or readily modifiable by the user. This is the major drawback in using CMG's package or other similar commercial simulators for understanding and prototyping new models that describe multiphysical coupled behavior. Despite its current limitations, Comsol's flexibility and transparency made it the best candidate for building geomechanically coupled models in this thesis.

In this chapter, the equations governing the two different problem domains have been presented. The default system of equations in a commercial finite element package has been verified and amended to handle bidirectionally coupled poroelastic behavior. In the next chapter, different computation schemes for implementing the numerical coupling between the flow and geomechanical components are addressed.

CHAPTER 3. COUPLING STRATEGIES

3.1 Introduction

As set forth in Chapter 2, the coupling between reservoir fluid flow simulation and geomechanics can be described by two equation sets accounting for the deformation of the skeleton and the fluid motion in the pore space. Computation methods for coupling pore fluid flow and solids deformation generally fall into four different categories: decoupled (loose), iterative coupling, explicit coupling, and full coupling. However, the degree to which this coupling is performed depends on the particular problem, and requires foresight and judgment from the model user. Factors include code compatibility and the desired level of accuracy and efficiency. This chapter focuses on a discussion of the various coupling strategies, and their nuances, advantages, and pitfalls. Ultimately, the result will be a better understanding of the strategy selected for implementation in this thesis.

3.2 Coupling Mechanics and Notation

The standard finite element matrices are formed using the principle of superposition. After space and time discretization, the coupled problem can be written in matrix notation (cf. Lewis and Schrefler, 1998):

$$K\Delta_t u + L\Delta_t p = F \tag{3.1}$$

$$L^T\Delta_t u + E\Delta_t p = R \tag{3.2}$$

where K is the stiffness matrix, Δ_t is the timestep, u is the solids displacement vector, L is the coupling matrix between mechanical and flow unknowns (i.e., displacement and pore pressure), F is the vector of force boundary conditions, E is the flow matrix, p is the pore pressure, and R is the source term for the flow drive. The timestep is defined such that such that $\Delta_t u = u^{n+1}-u^n$ and such that $\Delta_t p = p^{n+1}-p^n$ where n is the index of time discretization. In this notation, K and E are considered to be linear operators. For problems of nonlinear elasticity and nonlinear flow, K and E adopt a general nonlinear formulation.

In effect, Eqn. 3.1 balances the geomechanical equilibrium, whereas Eqn. 3.2 represents the fluid mass balance equation. Eqns. 3.1 and 3.2 are coupled through the coupling matrix L, such that the pore pressure gradient affects the stress equilibrium equation through the $L\Delta_t p$ term. Similarly, the displacement vector operates on the flow drive via the $L^T\Delta_t u$ term accounting for reservoir volumetric strains.

3.3 Loose Coupling

Decoupling (otherwise known as "pseudo" or "loose" coupling) of a system is achieved by assuming there are no displacements with each timestep (i.e., a conventional reservoir simulator), or conversely, there are no pressure changes with each timestep (i.e., classical elasticity). Empirical relations are derived from charts of porosity vs. vertical displacements and stress, and are entered directly into the reservoir simulator (Tran et al., 2004).

3.4 Iterative Coupling

The iterative coupling method solves the pore fluid flow variables and the geomechanical conditions independently and sequentially. The coupling between the reservoir simulator and the geomechanical model is then performed at the end of each timestep through pore volume calculations. Updated information on temperature and pressure from the reservoir simulator is sent to the coupling module. Conventionally, the mean total stress is usually assumed to be constant within reservoir simulators, thereby unrealistically limiting porosity to a function of temperature and pressure only. In the case of the iterative method, the geomechanical model sends to the coupling module a porosity function based on partial compressibilities through which the porosity changes with increments in temperature, pressure, and mean total stress (Tran et al., 2004). The number of iterations is determined by a convergence tolerance, typically set on pressure or stress changes between two consecutive iterations toward the solution (Figure 3-1). The advantage of the iterative coupling method is the relative ease of implementation since existing simulators for pore fluid flow and geomechanics can be linked externally (Tran et al., 2005a). Furthermore, the method is made more computationally efficient by specifying the porosity vs. effective stress relation directly in the reservoir flow model, as described in detail by Settari and Mourits (1998). The main disadvantage is that the

number of iterations may become unwieldy if the calculations tend toward a first-order convergence rate in nonlinear iterations.

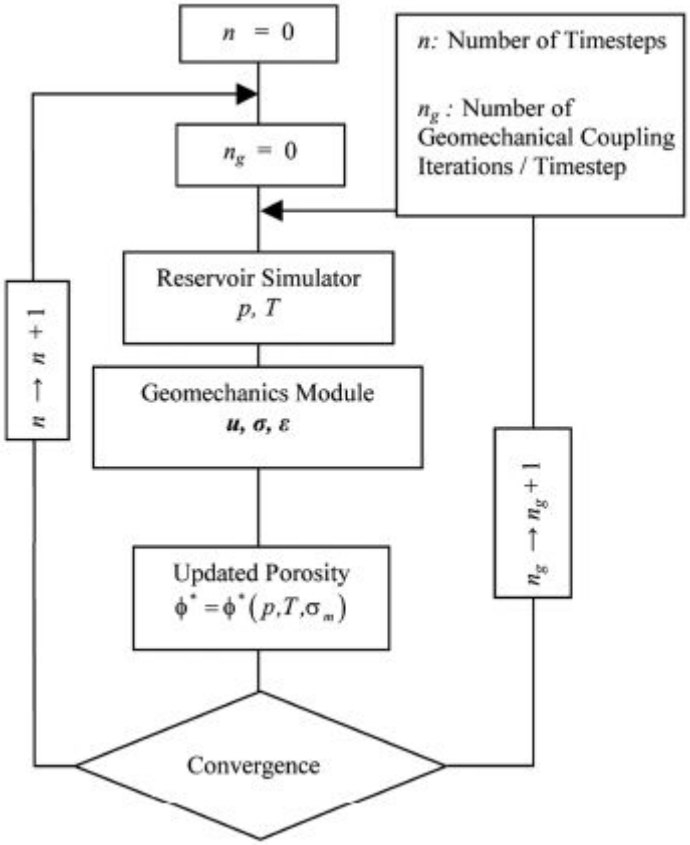

Figure 3-1. Workflow for the iterative method for coupled variables pressure (p), temperature (T), stress and mean total stress ($\boldsymbol{\sigma}$,σ_m), strain ($\boldsymbol{\varepsilon}$), reservoir porosity (ϕ), and displacement ($\mathbf{u}$). (modified from Tran et al. (2004))

3.5 Explicit Coupling

The explicitly coupled method is a special case of the iteratively coupled method in which only one iteration per one time increment is performed. Porous flow calculations are made at each timestep, whereas geomechanical deformations are only computed at selected timesteps, usually driven by the magnitude of pore volume changes. Alternatively, for water injection or other situations where stress-dependent enhancement of permeability is of primary interest, (Longuemare et al., 2002) have demonstrated an alternative method that ignores the volume coupling and instead uses a transmissibility function to achieve coupling through the T matrix. Again, the advantage of this method

is the ease of coupling an existing flow simulator to an existing geomechanical model. However, timestep restrictions are generally needed for stability and accuracy (Dean et al., 2006).

3.6 Full Coupling and Comparison of Numerical Approaches

For the full coupling (otherwise known as implicit coupling) method, Eqns. 3.1 and 3.2 are solved simultaneously and internally at each timestep. Whereas the explicit iterative coupling methods may employ mixed discretizations (reservoir simulators are typically finite difference and stress models are typically finite element), the fully coupled approach is internally consistent. The coupled system discretization may be either finite difference (Osorio et al., 1998) or finite element (Noorishad et al., 1982; Gutierrez and Lewis, 1998; Lewis and Schrefler, 1998). A comparison of the finite element method vs. the finite difference method is made in Table 3-1.

Table 3-1. Comparison of finite differences vs. finite elements methods. (after Zienkiewicz and Taylor (2000))

Finite Differences	Finite Elements
Approximation to the partial differential equation.	Approximation to the *solution* of the partial differential equation.
Discretization is always rectangular or square, and heavily constrained.	Discretization is triangular and allows for solving complex geometries and boundaries.
Easier to implement and solve.	Difficult to implement and solve.
Resolution between grid points can be of poor quality.	Interpolation is better except in a few straightforward problems.

The focus of this thesis will be on implementing a unified finite element platform. Although more complicated to solve, the primary advantage of the finite element approach is the flexibility in handling multiple complex geometries. However, in order to ensure solution convergence, finite-element fluid flow mechanisms are often simplified in comparison with conventional simulators (typically finite difference) such as Eclipse. However, the finite element approach remains a compelling and viable alternative with opportunities for new development and use in reservoir geomechanics.

A goal of this research is to implement a fully-coupled code in the finite element framework that honors the multiphysical linkages between fluid flow, geomechanics, and ultimately seismic velocity changes.

3.7 Summary

Numerical coupling schemes can be separated into two general groups. Coupling can be implemented throughout the problem domain, or it can be carried out at a numerical interface at certain time steps. The degree of physical coupling between the fluid flow phase and the geomechanical phase in a reservoir must be investigated before choosing a coupling scheme. For many geological problems, the physical coupling is tight and complex, necessitating a coupled numerical approach throughout the problem domain.

In theory, the same results for the iteratively coupled and the fully coupled schemes are expected at convergence. Although offering flexibility and modularity, the iteratively coupled scheme can consume unneeded nonlinear iterations to achieve convergence between the two subdomains. Furthermore, stability and solution uniqueness are difficult to ensure for iterative methods if the two subdomains are tightly coupled. The fully-coupled approach is the most robust, fundamentally correct, and internally consistent scheme in that all the equations are set up and solved simultaneously in a single matrix. Besides these advantages, the fully-coupled approach can be used to isolate the sensitivity of a particular parameter such as porosity or permeability. The focus of this thesis is on the implementation of fully-coupled geomechanical models in the framework of a finite element environment.

CHAPTER 4. PRACTICAL NUMERICAL SIMULATIONS

4.1 Introduction

This chapter presents several numerical simulations to verify the validity of the poroelastic formulation developed in Chapter 2 and its implementation into a finite element code. While these models may not incorporate every physical and chemical phenomena that may be of interest in geologic systems, the purpose is to gain a better understanding of two fundamental physical processes, pore fluid flow and deformation, and to emphasize their mutual dependence within a system.

Consequently, a number of assumptions and limitations must be imposed on the models, such as, homogeneity of grains at the pore scale, Darcy flow (i.e., no skin effects), no heat effects, and no chemical alterations. The complete mathematical description of all assumptions involved is covered thoroughly in Lewis and Schrefler (1998). Here, the emphasis of this section is to unify the fluid-structure interaction in working simulations within the finite element framework and to demonstrate various observable phenomena singular to a fully-coupled poroelastic formulation.

4.2 Uniaxially-Constrained Consolidation Test

A simple uniaxial consolidation test simulation is performed in a 2-D model domain to verify the Terzaghi-based (1943) analytical solutions used in standard soil mechanics texts (e.g., Das, 2004). Zheng (2003) provides the theoretical basis for the finite-element approach to the problem. Here, the goal is to confirm that the Biot-based, fully-coupled formulation developed in Chapter 2 is correctly implemented in Comsol 3.3a and agrees with deformation behavior observed at the laboratory scale.

4.2.1 Model Description

The classic Terzaghi experiment is represented by a 2-D sample domain in finite elements. The geomechanical and fluid properties used in this study are listed in Table 4-1. A schematic of the simulation is shown in Figure 4-1. The horizontal and vertical displacements of the bottom boundary are constrained to zero and the horizontal

displacements of the left and right boundaries are constrained to zero. The top boundary is free to move vertically. In this first simulation, all the boundaries are undrained ("no-flow"). A uniformly load of 5 MPa is suddenly applied along the top boundary. The effects of gravity are ignored in this simulation.

For this experiment, Terzaghi derived a consolidation equation for excess pore pressure,

$$\frac{\partial p}{\partial t} = c\frac{\partial^2 p}{\partial z^2} \tag{4.1}$$

where c is Terzaghi's experimental consolidation and the other variables are as previously defined. The consolidation coefficient, c, is equivalent to the expression, $\frac{k}{\mu S}$, where S is the uniaxial specific storage coefficient. This formulation is independent of stress and is compared to results of the Biot poroelastic finite element simulation.

Table 4-1. Geomechanical and fluid properties used in the Terzaghi simulation.

Symbol	**Comments**	**Units**	**Expression**
ρ_f	Fluid Density	kg m^{-3}	0.94e3
k	Permeability	m^2	2e-13
S_ε	Constrained Specific Storage	Pa^{-1}	8.1e-11
α	Biot-Willis Coefficient	[dimensionless]	0.8
μ_f	Dynamic Fluid Viscosity	N s m^{-2}	1.12e-4
E	Young's Modulus	N m^{-2}	14e9
ν	Poisson's Ratio	[dimensionless]	0.20
ø	Porosity	[dimensionless]	0.20
ρ_r	Rock Density	kg m^{-3}	2.0e3

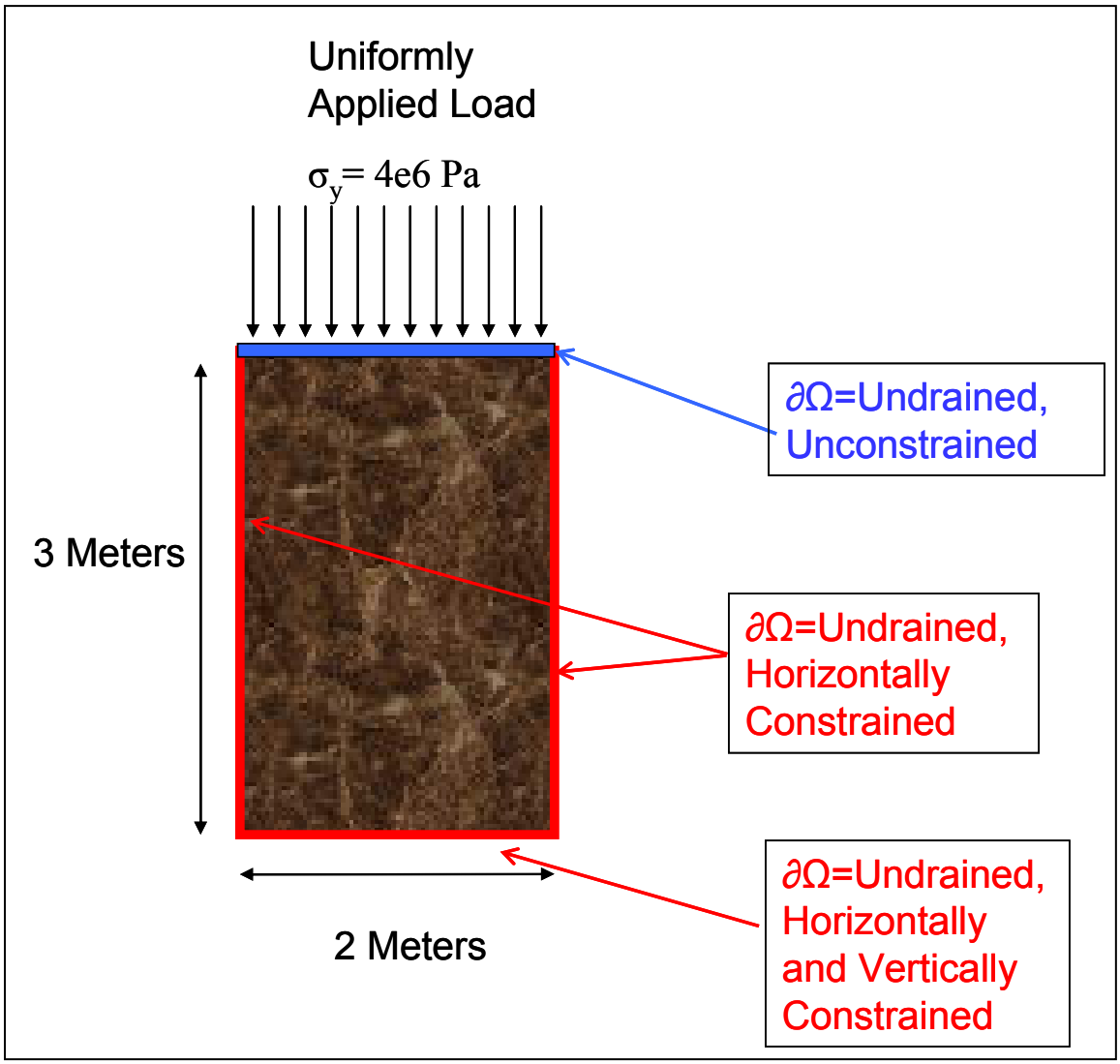

Figure 4-1. Schematic of the uniaxially-constrained loading simulation.

4.2.2 Model Results and Discussion

The vertical displacements resulting from the applied stress are shown in Figure 4-2. Figure 4-3 compares the vertical displacements calculated from the Biot poroelastic simulation to Terzaghi's solution. There is excellent agreement since the solution predicted by Terzaghi is a special case of the theory of poroelasticity where the pore pressure field is effectively uncoupled from the applied stress field given these boundary conditions. The strain is uniform inside the model domain. Similarly, the pore pressure

is distributed equally throughout the sample (due to Pascal's Principle) since the closed system is undrained (Figure 4-4).

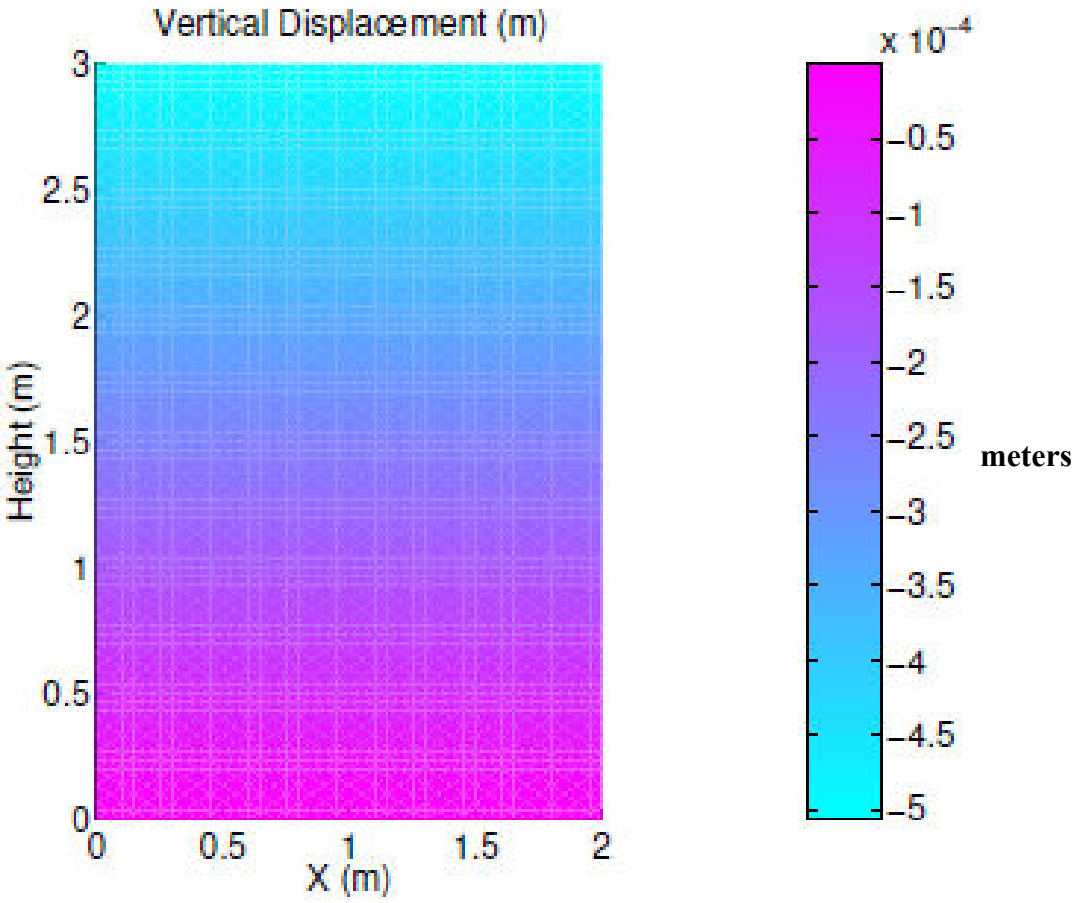

Figure 4-2. Vertical displacement of the sample under uniform loading and with undrained boundaries.

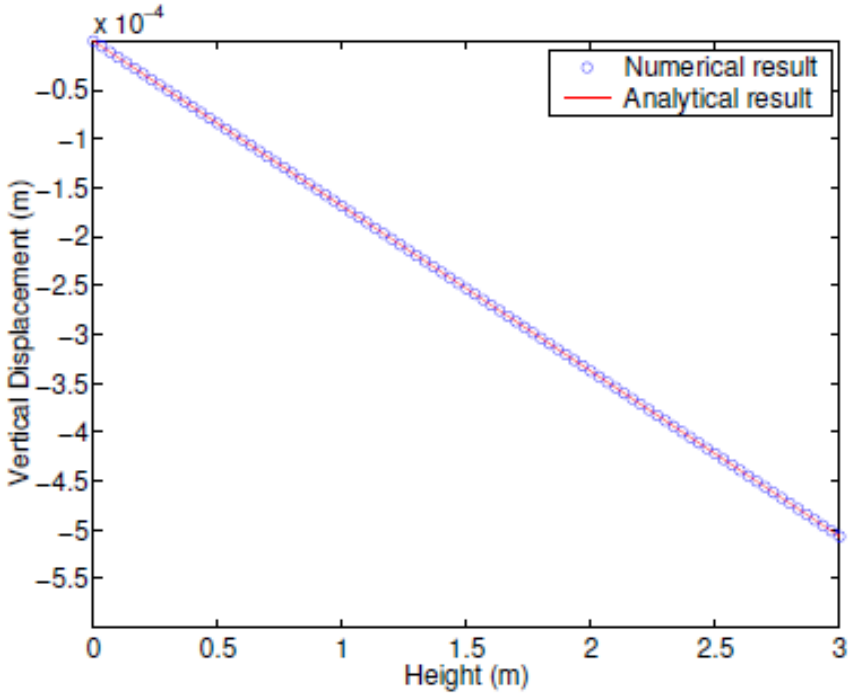

Figure 4-3. Vertical displacement vs. height of the sample with undrained boundaries.

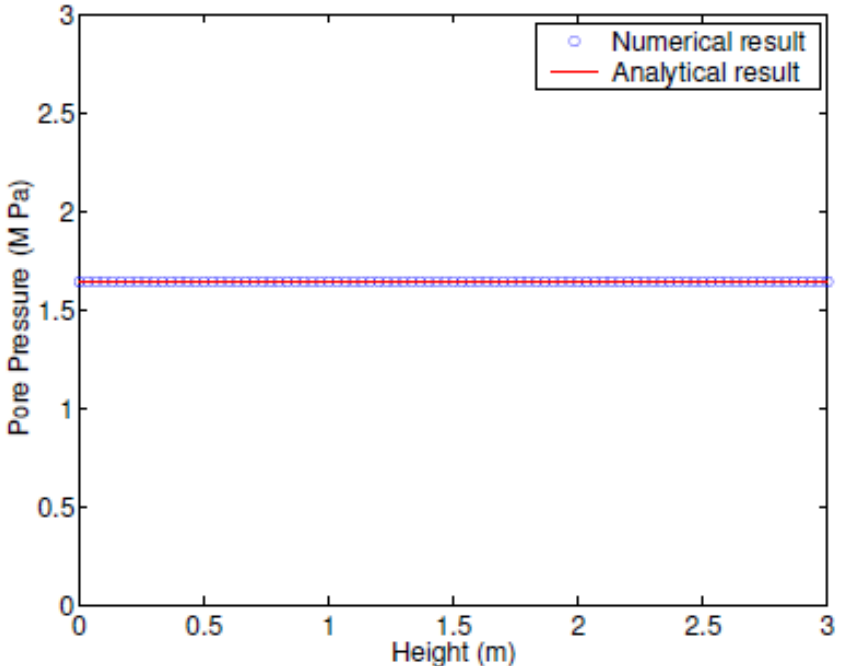

Figure 4-4. Pore pressure vs. sample height with undrained boundaries.

4.3 Verification of Mandel-Cryer's Problem

In this section, a numerical simulation of the Mandel-Cryer problem is carried out as a verification of the fully-coupled poroelastic formulation described in Chapter 2. Prokofiev (2007) identified the need to test this scenario within the finite element framework of Comsol 3.3a. The Mandel-Cryer effect has been used in a number of studies as a benchmark for testing poroelastic models (Detournay and Cheng, 1993; Hart, 2000; Akers, 2001).

Mandel (1953) presented an example of nonmonotonic poroelastic behavior in response to the sudden compression of a long rectangular prism between two rigid, impermeable plates. The pore pressure rises nonmonotonically above the initial normal stress condition in the central region of the sample, and then decays as fluid leaks out the side boundaries, and the load transfers to the solid matrix. Mandel's problem is described in mathematical detail by Detournay and Cheng (1988). The behavior is explained by the contraction at the drained boundaries inducing additional pore pressure build-up in the plate interior.

Similarly, Cryer (1963) developed an analytic solution to a problem of a drained sphere of elastic porous material having an applied constant surficial pressure. Cryer found that the pore pressure at the center of the sphere exceeds the externally applied pressure, and then reverses and dissipates. This nonmonotonic behavior, due to poroelastic coupling, is termed the Mandel-Cryer effect.

Gibson et al. (1963) were able to reproduce the Mandel-Cryer effect by conducting several laboratory experiments on clay spheres. They demonstrated that the total stress within a consolidating sphere is in fact time-dependent, in contrast to the stress-time invariance predicted by Terzaghi's consolidation theory (Cryer, 1963). Total stress at the center of the sphere increases above unity at early times, and decays at later times.

To understand this effect qualitatively, Hart (2000) describes the poroelastic response in a cylinder (Figure 4-5). In an interior region, the pore pressure is suddenly stepped up, reducing the effective stress and pulling the sample apart. This creates a new region of negative pore pressure. Also, a region of negative axial strain occurs that is associated with the region of pore pressure decrease. Subsequently, the axial strain

increases as the sample expands as pore pressure diffusion overtakes the initial pore pressure decrease. A pore pressure change generating a strain which in turn induces a pore pressure of sign opposite to the initial pore pressure change is a result of the Mandel-Cryer effect.

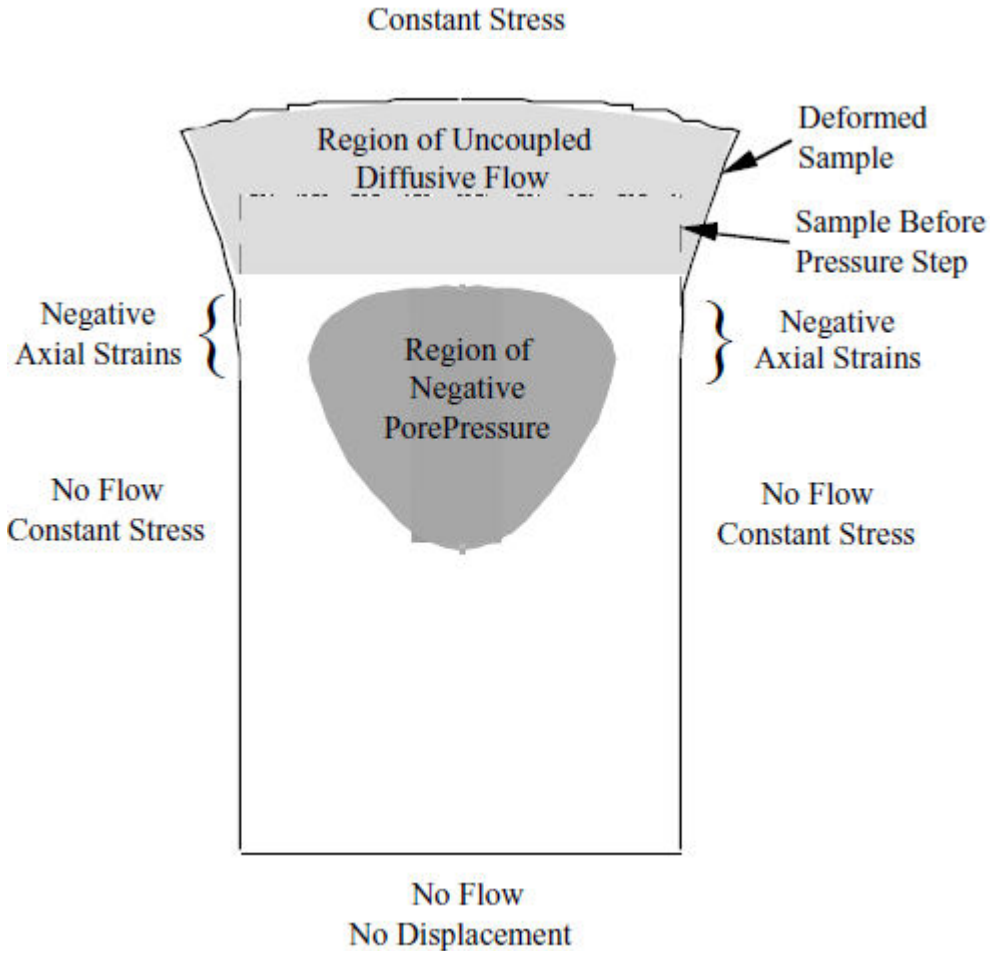

Figure 4-5. Schematic description of the poroelastic pore-pressure response. (after Hart, 2000)

4.3.1 Model Description

To verify the Mandel-Cryer effect with finite element code, two simulations of a drained, infinite cylinder of saturated rock are performed. One simulation is fully coupled while the other simulation uses the uncoupled, Darcy-based, fluid-flow continuity equation. Mandel (1953) showed that the nonmonotonic behavior results

from inclusion of the strain-displacement source term, $-\alpha \frac{\partial}{\partial t}(\vec{\nabla} \cdot \vec{u})$, in the fluid-flow continuity equation (cf. Eqn. 2.43):

$$Q - \alpha \frac{\partial}{\partial t}(\vec{\nabla} \cdot \vec{u}) = S_{\varepsilon} \frac{\partial p}{\partial t} - \vec{\nabla} \cdot (\frac{k}{\mu} \vec{\nabla}(p + \rho_f g D)) \tag{4.2}$$

The time derivative of dilation is dropped from the equation for the second simulation:

$$Q = S_{\varepsilon} \frac{\partial p}{\partial t} - \vec{\nabla} \cdot (\frac{k}{\mu} \vec{\nabla}(p + \rho_f g D)) \tag{4.3}$$

Note that the former equation is the default equation for the Darcy's Law application mode in Comsol.

A horizontal cross-section of the cylinder is simulated using geomechanical properties typical of Berea sandstone (Table 4-2). The cylinder has a diameter of one meter. Water is used as the saturating fluid. A sudden compressive radial unit load is applied uniformly at t=0 (Figure 4-6). The boundary is drained, meaning the fluid is free to leak out of the cylinder. The circumferential wall and interior solid domain are allowed to contract.

Table 4-2. Geomechanical properties of Berea sandstone and fluid properties of water for the Mandel-Cryer effect simulation. (after Wang, 2000)

Symbol	**Comments**	**Units**	**Expression**
K	Bulk Modulus of Water	Pa	2.3e9
ρ_f	Fluid Density	kg m^{-3}	1e3
k	Permeability	mD	1.9e2
S_α	Poroelastic Storage Coefficient	m^{-1}	1e6
α	Biot-Willis Coefficient	[dimensionless]	0.8
μ_f	Dynamic Viscosity of Water	N s m^{-2}	1.12e-3
E	Young's Modulus	N m^{-2}	14e9
ν	Poisson's Ratio	[dimensionless]	0.20
ø	Porosity	[dimensionless]	0.20
ρ_b	Bulk Density	kg m^{-3}	2.2e3

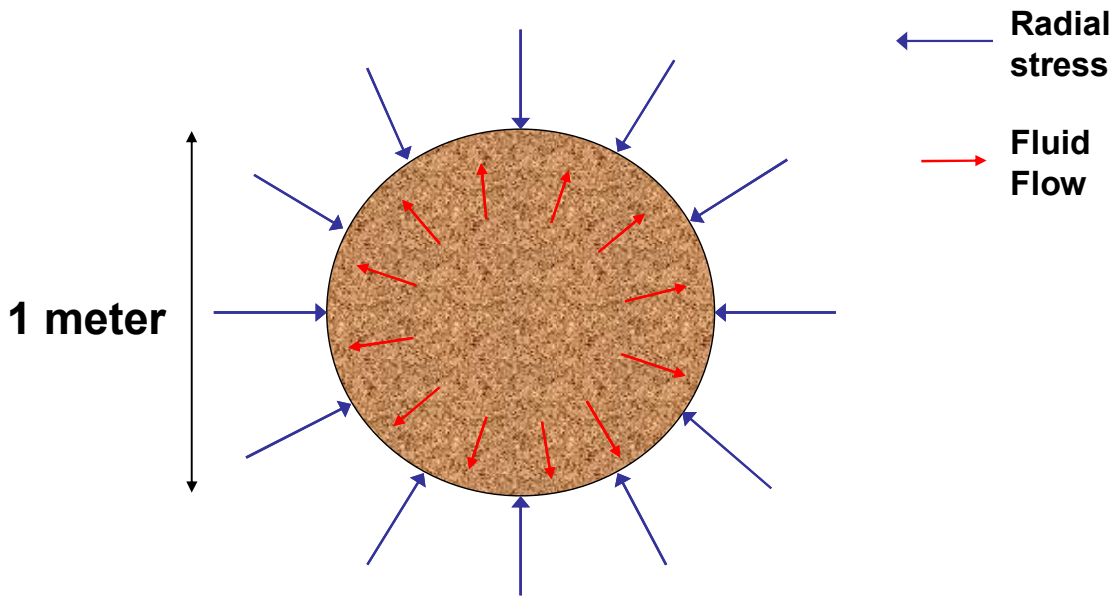

Figure 4-6. Schematic of fluid-saturated cylinder cross-section (1 meter in diameter) under uniformly-applied radial compressive load at t=0.

4.3.2 Model Results and Discussion

The horizontal cross-section of the pressure distribution within the cylinder is captured in Figure 4-7. The original shape is outlined and the arrows indicate radial fluid flow. Pore pressure measured at the center of the cylinder (x=0,y=0) is plotted versus dimensionless time. A comparison of the pore pressure computed from the fully-coupled poroelastic formulation (with the time derivative of dilation term) versus the uncoupled default Darcy's Law formulation (without the time derivative of dilation term) clearly illustrates the Mandel-Cryer effect. For the fully-coupled simulation, the pore pressure at the center of the cylinder rises above the initial value, then reverses and dissipates. The behavior is explained by the fact that cylinder contracts close to the drained boundary due to the pore pressure decay and reduction of effective stress. Strain compatibility requires consolidation, and thus, pore pressure buildup at the core.

Consequently, the Mandel-Cryer effect can be understood as a stress transfer towards the interior. The poroelastic pore pressure at the core is greater than the uncoupled pore pressure obtained from standard fluid-continuity equation. Therefore, the decay of the build-up in pore pressure takes longer than would be predicted from an

uncoupled solution. A practical application of this effect in a drill stem pressure-transient tester simulation is illustrated in the next section (4.4).

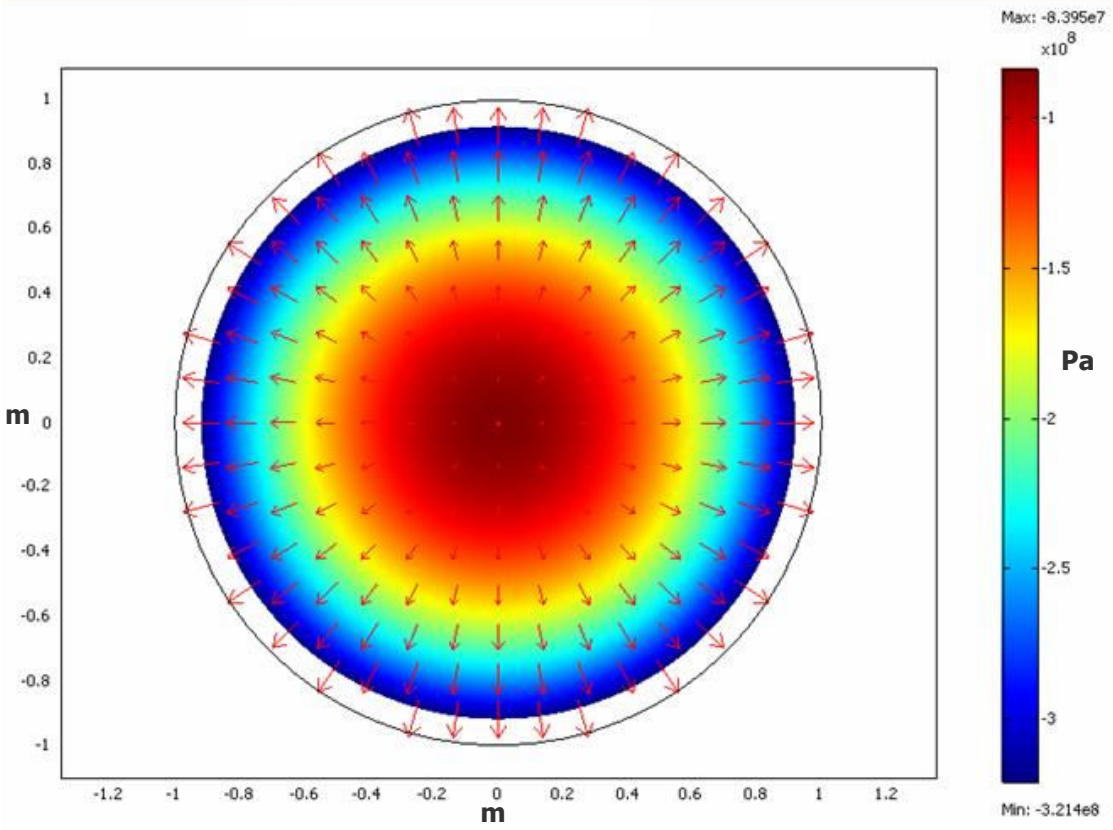

Figure 4-7. Cross-section of a cylinder showing early pressure (Pa) distribution. The pore pressure build up at the center indicates a Mandel-Cryer effect. The red arrows indicate fluid flow vectors. Dimensions are in meters.

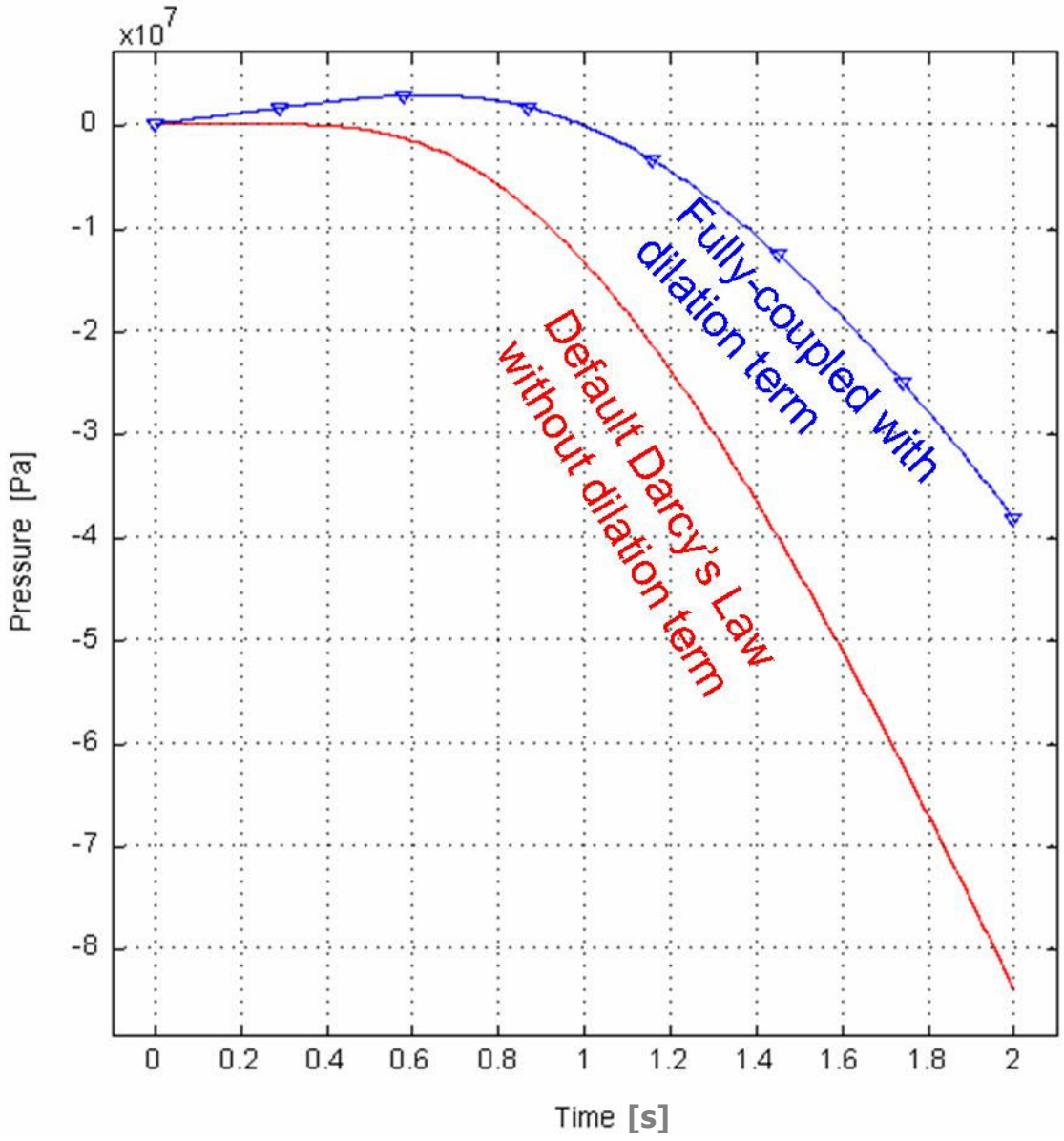

Figure 4-8. Pressure (Pa) at the center (x=0,y=0) of the cylinder vs. time (sec). The fully-coupled poroelastic simulation captures the expected nonmonotonic behavior due to the Mandel-Cryer effect.

4.4 Formation Pressure Testing Simulation

In this section, the measurement configuration of a drill stem test is simulated to better understand the interaction between fluid pressure and solid deformation. Formation pressure testers are used in hydrogeological investigations (Hackbarth, 1978) and by the petroleum industry (Lee et al., 2003) to evaluate the production potential of a

particular interval. Fluid flow parameters of a formation such as permeability are analyzed by measuring pressures in response to an applied constant or transient flow rate. The drill stem test, conducted before the well is cased, measures the reservoir fluid pressures in a packed-off interval. The bottom-hole pressures are recorded during the flow test. A schematic drawing of a typical dual-packer formation tester is shown in Figure 4-9.

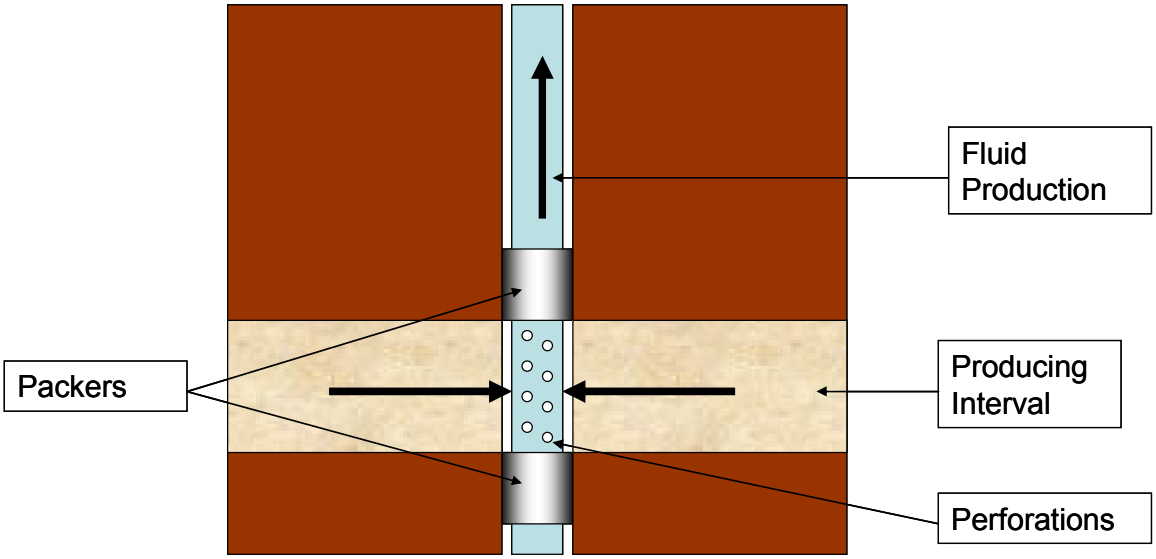

Figure 4-9. Schematic drawing showing a dual-packer drill stem formation tester.

Although considerable efforts have been made to model coupled flow and deformation at reservoir scale, there are few published studies on the modeling of near-wellbore pressure-transient behavior and local deformation. Lee et al. (2006) describe a loosely coupled, 2-D axial-symmetric, finite-difference formulation for simulating drill stem testing. Their study is the impetus for developing a fully-coupled, finite-element implementation.

4.4.1 Model Description

In developing a coupled model of a conventional drill stem formation test, the physical dimensions and the initial and boundary conditions must be specified to accurate represent the tool's configuration and operation. As a first approach, a medium with homogenous and isotopic geomechanical and fluid properties is assumed for this model. A 2-D axial-symmetric model domain is used because of the symmetry around the

wellbore. A typical length of the packed off interval is 25 m (Lee et al., 2003). This boundary acts as a fluid sink. Whereas the fluid effects are relatively confined to the pore flow scale in the near-wellbore region, the distribution of the coupled geomechanical effects extend more distally. Therefore, a relatively large scale is used to model the formation: the vertical depth is 400 m (15 times greater than the packed-off interval) and the horizontal range interval is 3000 m (120 times greater than the packed-off interval). The material properties and poroelastic parameters selected for the model (Table 4-3) are typical for a sandstone reservoir simulation (Wang, 2000).

For this analysis, the change in hydraulic head, *H*, will be solved for instead of the pressure variable, *p*. Multiplying pressure by fluid density and the gravitational constant yields the hydraulic head, with units in meters. This modification allows the boundary conditions to be simplified. All the fluid flow boundary conditions are specified as zero fluid flux ("no-flow boundaries"), except in the packed-off fluid sink interval at x=(0,0), y=(-187.5,-212.5). At this boundary interval, the hydraulic head drawdown rate is set to 0.1 m/day for a test period of t=2.4 hours. The initial hydraulic head at the top surface (y=0) is specified as zero.

Table 4-3. Material properties used in the drill stem test simulation. (from Wang, 2000)

Symbol	**Comments**	**Units**	**Expression**
g	Gravitational Constant	$m\ s^{-2}$	9.82
ρ_f	Fluid Density	$kg\ m^{-3}$	820
k	Intrinsic Permeability	m^2	1.875e-13
S_α	Poroelastic Storage Coefficient in Head Form: $S_\varepsilon=S_\alpha/(\rho_f g)$	m^{-1}	1e6
α	Biot-Willis Coefficient	[dimensionless]	0.8
μ_f	Dynamic Viscosity	$N\ s\ m^{-2}$	0.4
E	Young's Modulus	$N\ m^{-2}$	8e8
ν	Poisson's Ratio	[dimensionless]	0.20
ø	Porosity	[dimensionless]	0.20
ρ_b	Bulk Density	$kg\ m^{-3}$	2200

The plane strain boundary conditions are such that allow horizontal and vertical displacements at the top surface and throughout the model domain. The base is fixed such that horizontal and vertical displacements are constrained to zero. Horizontal displacement is constrained to zero at the left and right boundaries.

Meshing the whole computation domain is required for the finite element computations. Figure 4-10 shows the meshing of the problem domain used in the simulation. The domain is meshed into 369 triangular finite elements, with higher refinement approaching the sink boundary located at x=(0,0), y=(-187.5,-212.5). The intent is to achieve higher computation accuracy near the wellbore where the physical interaction between fluid flow and deformation is most tightly coupled. Since this model is dealing with a transient analysis of a drill stem test, Comsol's time dependent linear system solver is used to find a converging solution.

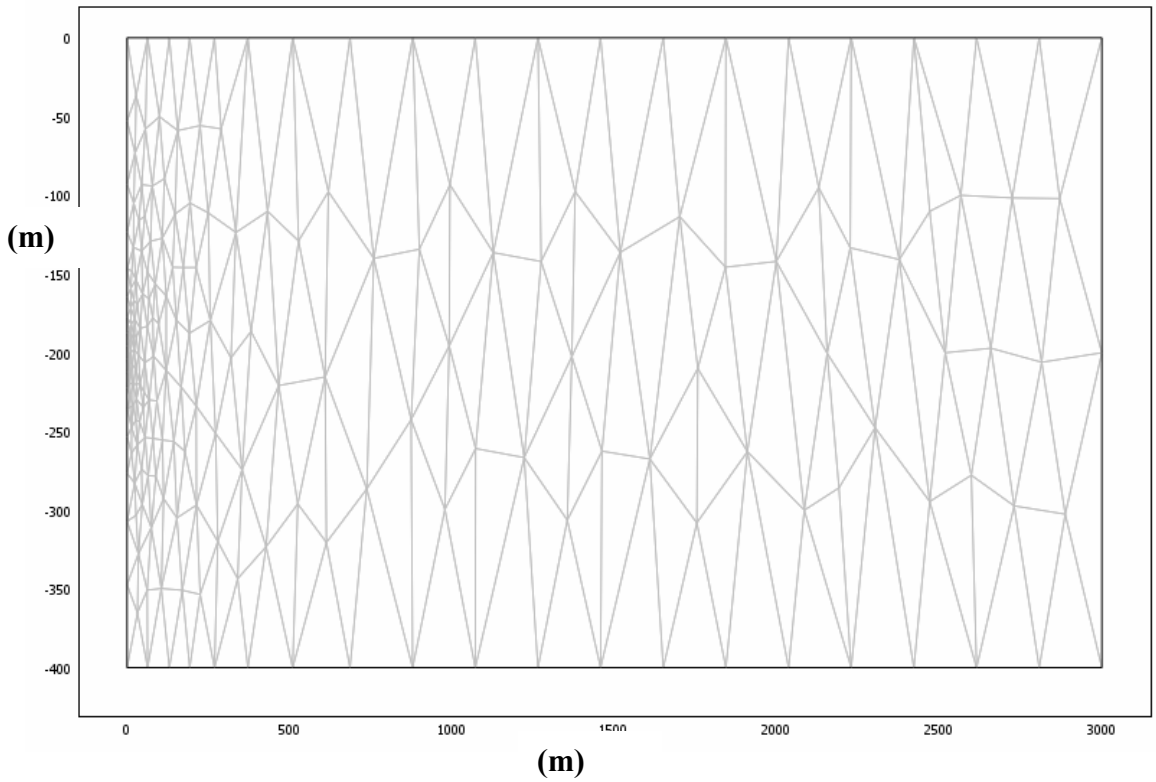

Figure 4-10. Finite element mesh containing 369 triangular elements. The mesh refines gradually toward the sink located at x=(0,0), y=(-187.5,-212.5). Dimensions are in meters.

4.4.2 Model Results and Discussion

The von Mises stress distribution after the drawdown rate of 1m/day has been applied for t=2.4 hours is shown as a surface plot in Figure 4-11. The streamlines illustrate the fluid flow paths towards the sink boundary. The arrows represent fluid flow velocities, which increase approaching the sink boundary. In Figure 4-12, the von Mises stress distribution along the line y=-200 m (shown in pink in Figure 4-11) is plotted in incremental 0.048-hour intervals during the drawdown period from t=0 to t=2.4 hours. The von Mises stresses are highest near the well. However, the stress distribution trends make a reversal near x=400m. This nonmonotonic behavior is an example of the Mandel-Cryer effect described in section 4.2. Similarly, total displacements along the line y=-200 m for each time interval are shown in Figure 4-13. In this case, the trend reversal occurs around x=800 m at later times. The pore pressure distribution along the line y=-200 m for each time interval is shown in Figure 4-14. The fact that pressures stabilize away from the well indicates the chosen model domain range is sufficiently large. The pressure history at the point x=0,y=-200 is shown in Figure 4-15. The pressure drops significantly in the first five minutes, and then continues to gradually decrease until the end of the simulation.

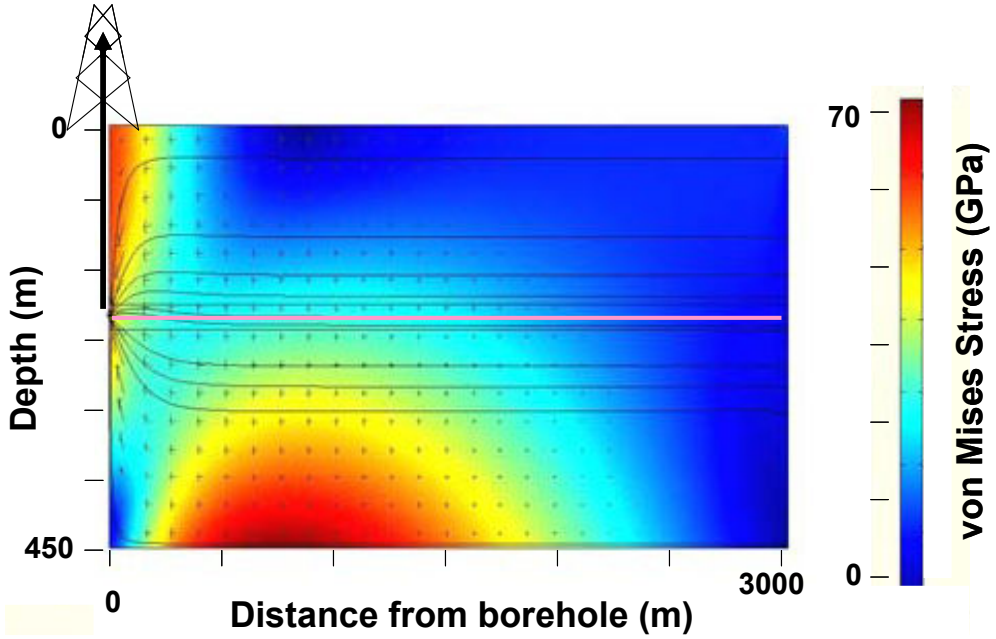

Figure 4-11. Drill stem test simulation showing a surface plot of the von Mises stress distribution after the drawdown rate of 1m/day applied for t=2.4 hours. The black lines indicate the streamlines of fluid flow and the arrows indicate fluid velocity.

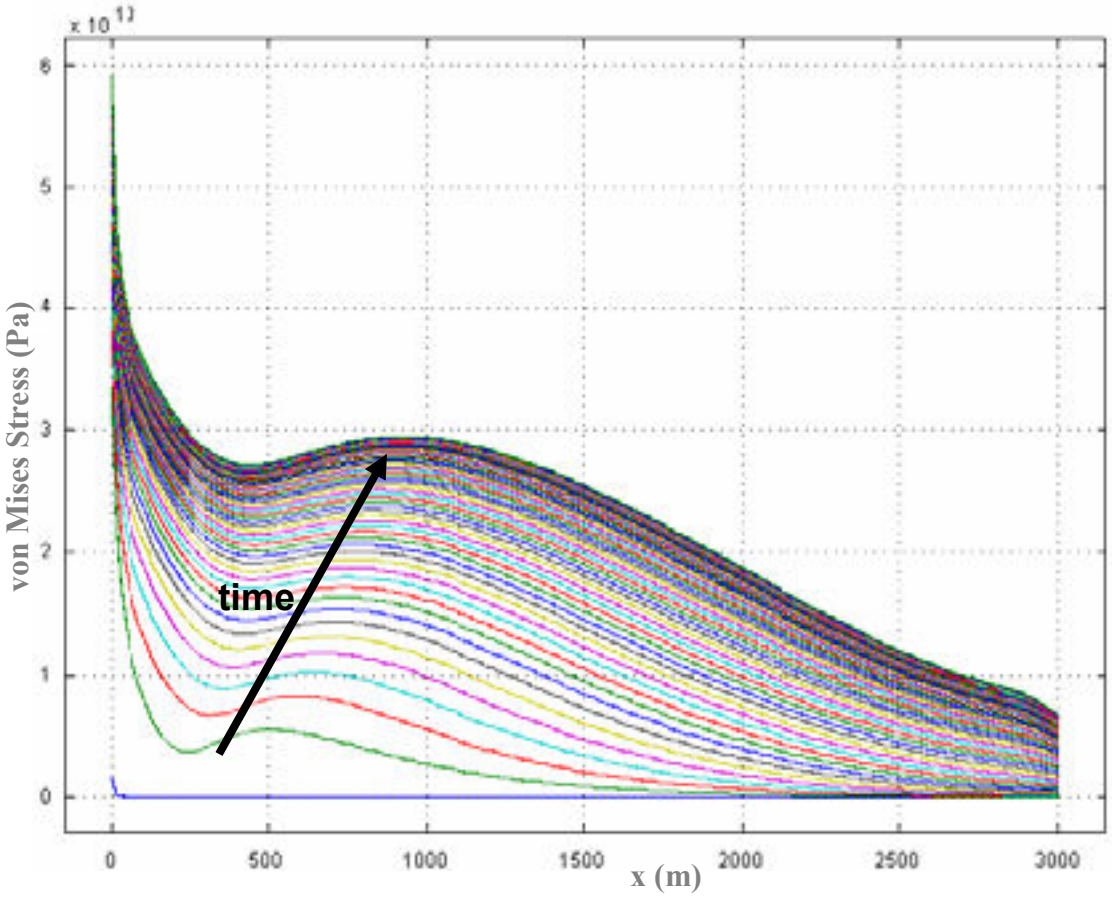

Figure 4-12. von Mises stress distribution over the entire drawdown period with 0.05-hour (3-minute) time intervals.

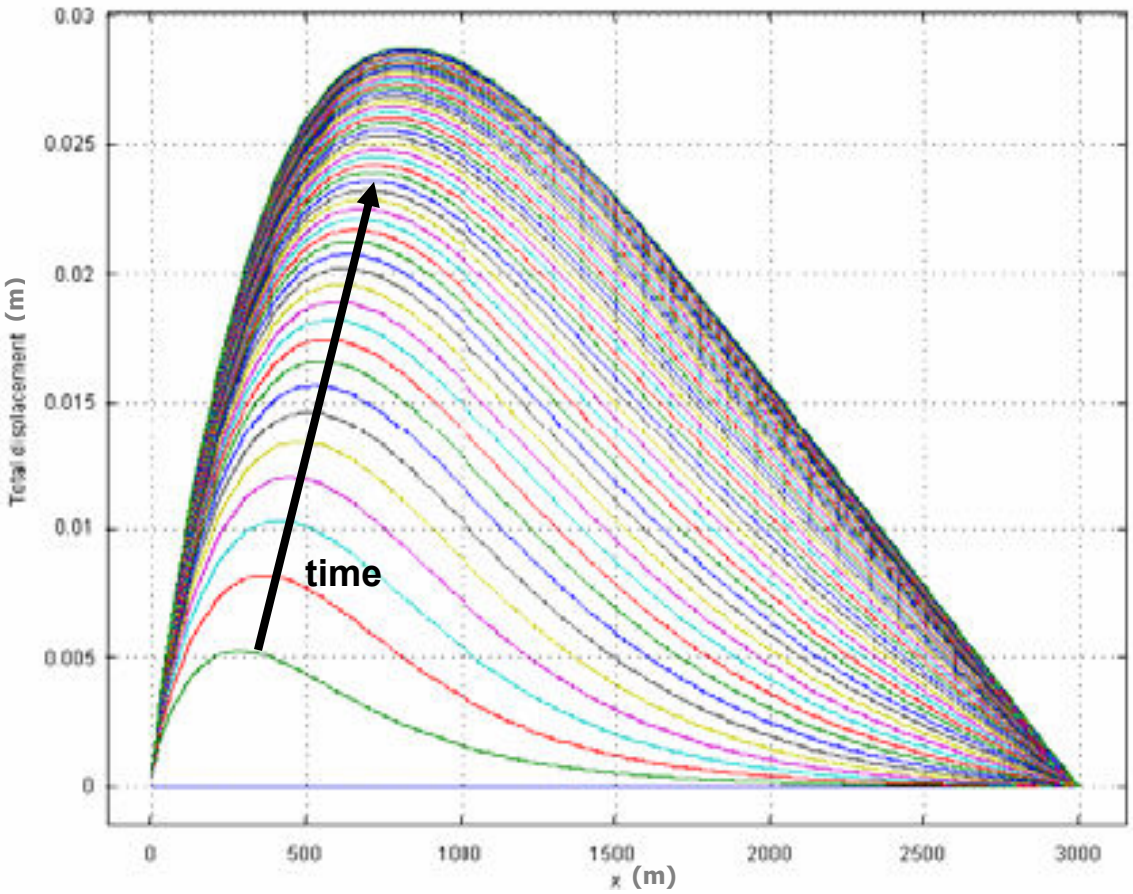

Figure 4-13. Distribution of total displacement through the reservoir with 0.05-hour (3-minute) time intervals from t=0 to t=2.4 hours.

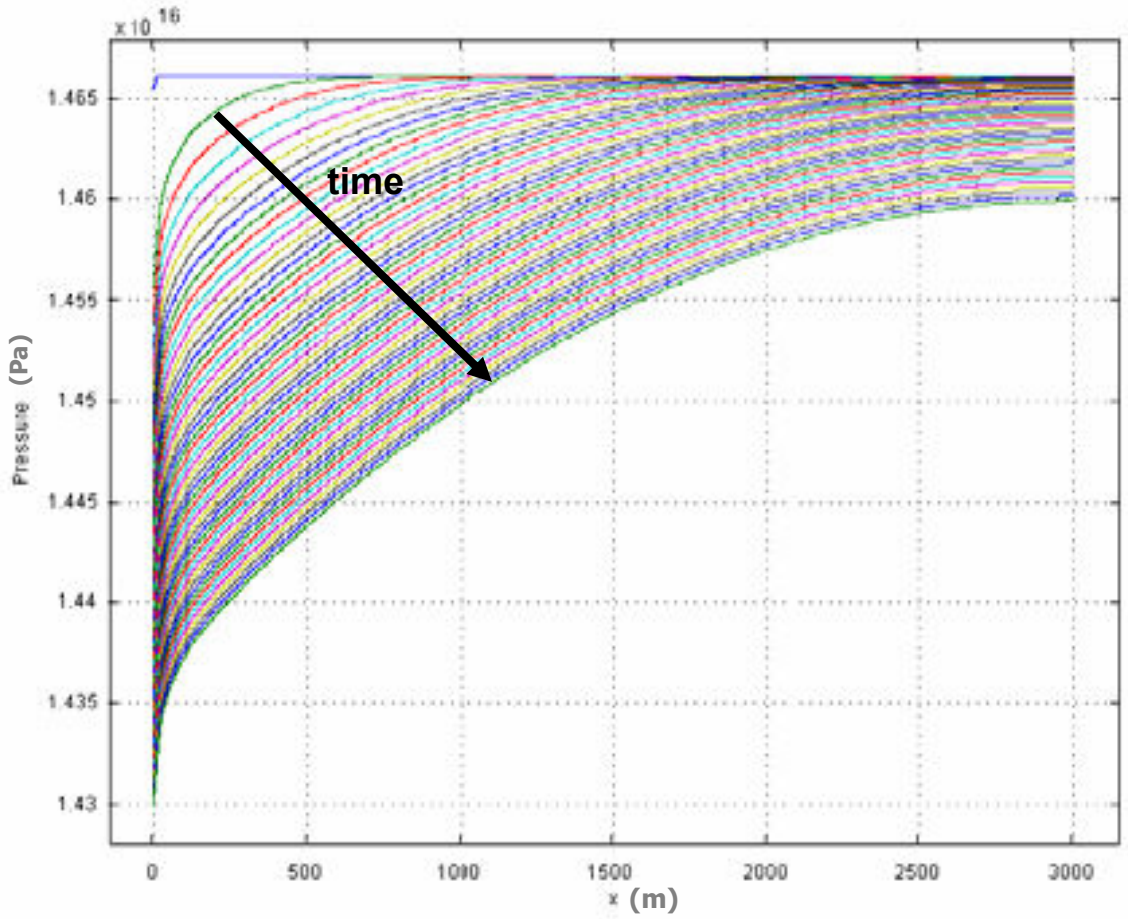

Figure 4-14. Pressure Distribution through the reservoir with 0.05-hour (3-minute) time intervals from t=0 to t=2.4 hours.

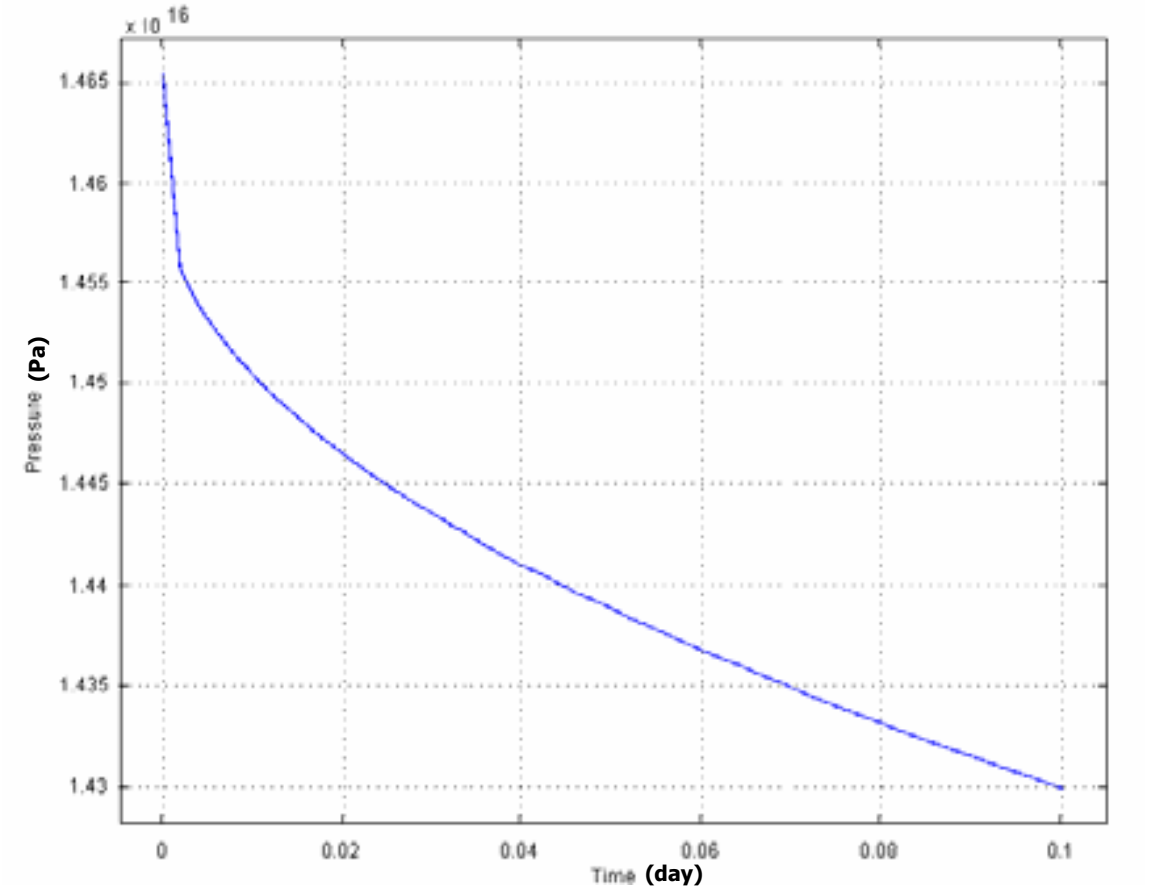

Figure 4-15. Pressure history at y=-200 m for a drawdown rate of 1/m day applied for t=0.1 days hours.

4.5 Modeling of the Noordbergum Effect through the Compaction of a Pumped Confined Aquifer

In this section, a numerical simulation is presented to investigate the "Noordbergum effect" due to pumping of a confined aquifer. The term was first coined by Verruijt (1969) to explain the phenomena observed during confined aquifer pumping tests in the village of Noordbergum whereby fluid pressures (measured in terms of hydraulic head) sharply increased in the overlying unconfined aquifer not being directly pumped. The phenomena, sometimes called "reverse water-level fluctuation," has been observed in a number of field tests (Wolff, 1970; Langguth and Treskatis, 1989), but has largely been disregarded and irreproducible in conventional 1-D flow modeling projects.

The conventional approach assumes horizontal displacements are constrained to zero and that vertical total stress is constant. Making these assumptions allows the modeling code to be greater simplified to solve the problem just in terms of hydraulic head using variations of Terzaghi's 1-D diffusion equation discussed in Chapter 4.2.2. However, the observable Noordbergum effects, which can manifest as fissures at the near surface, create a paradox for this approach. A sharp increase in hydraulic head in a zone adjacent to the produced zone can only be explained by a strong coupling between pore fluid flow and the surrounding solid rock matrix. Except for special simplified cases allowing decoupling, there are no general analytical solutions to Biot's poroelastic formulation for most real reservoirs having heterogeneous layers and asymmetric geometries. Consequently, a numerical poroelastic formulation using the finite element approach is developed with the Comsol package to analyze the Noordbergum effect in realistic field settings.

4.5.1 Model Description

This model builds upon hydrogeologic data made available from Leake and Hsieh (1997) in the US Geological Survey Open Report 97-47 and Comsol's modeling library. The intent here is to verify the initial analysis of Leake and Hsieh, append the additional coupling terms discussed in Chapter 2, and build a realistic hydrogeologic model.

The data are from a hydrogeologic system in San Joaquin Valley in central California. Three geologic layers form the hydrogeologic system in the 2-D axisymmetrical model domain. These layers are classified into the following subdomains: an overlying unconfined aquifer ($\Omega 3$), a middle confining aquitard ($\Omega 2$), and a lower confined aquifer ($\Omega 1$), shown in Figure 4-16. These units fill in an alluvial basin that is bounded by mountain range where faulting has created an impermeable bedrock step. The basin extends down 420 m in the center of the basin and thins out gradually to 120 m above the bedrock step. The aquitard itself pinches out towards this step. The geomechanical properties and associated parameters are listed in Table 4-4. The assumptions are that the geologic units are homogeneous and isotropic.

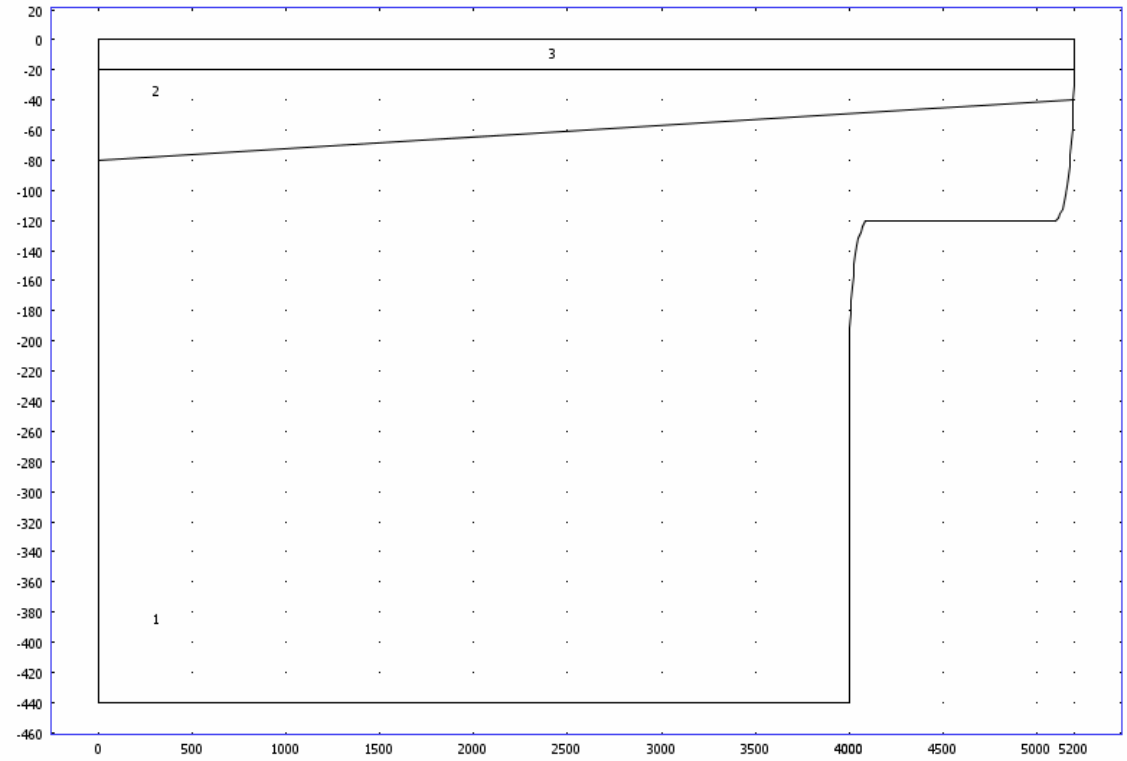

Figure 4-16. The three subdomains and model geometry of the hydrogeologic system. Dimensions are in meters.

Table 4-4. Geomechanical and fluid flow properties of the aquifer pumping simulation.

Symbol	**Comments**	**Units**	**Expression**
g	Gravitational Constant	$m\ s^{-2}$	9.82
ρ_f	Fluid Density of Water (15°C)	$kg\ m^{-3}$	999
μ_f	Dynamic Fluid Viscosity	$N\ s\ m^{-2}$	1.12e-3
E (Ω3)	Young's Modulus of Upper Aquifer	$N\ m^{-2}$	8e8
E (Ω2)	Young's Modulus (Middle Confining Aquitard)	$N\ m^{-2}$	8e7
E (Ω1)	Young's Modulus (Lower Confined Aquifer)	$N\ m^{-2}$	8e8
ν (Ω3)	Poisson's Ratio (Ω3)	[dimensionless]	0.25
ν (Ω2)	Poisson's Ratio (Ω2)	[dimensionless]	0.25
ν (Ω1)	Poisson's Ratio (Ω1)	[dimensionless]	0.25
ø (Ω3)	Porosity (Ω3)	[dimensionless]	0.20
ø (Ω2)	Porosity (Ω2)	[dimensionless]	0.20
ø (Ω1)	Porosity (Ω1)	[dimensionless]	0.20
P_r (Ω1), (Ω3)	Rock Density (Ω1), (Ω3)	$kg\ m^{-3}$	2200
P_r (Ω2)	Rock Density (Ω2)	$kg\ m^{-3}$	2500
α	Biot-Willis Coefficient	[dimensionless]	0.95
S_α (Ω3)	Poroelastic Storage Coefficient (Ω3) where $S_\varepsilon=S_\alpha/(\rho_f g)$	m^{-1}	8.5e-6
S_α (Ω2)	Poroelastic Storage Coefficient (Ω2) where $S_\varepsilon=S_\alpha/(\rho_f g)$	m^{-1}	8.5e-5
S_α (Ω1)	Poroelastic Storage Coefficient (Ω1) where $S_\varepsilon=S_\alpha/(\rho_f g)$	m^{-1}	8.5e-6
H_0	Initial Steady State Hydraulic Head	m	0
H_t	Declining Head Boundary	$m\ year^{-1}$	7

In this simulation, the poroelastic storage coefficient (in hydraulic head form) accounts for the compressibility of the fluid, which in this case is assumed to be water

(β_w=0.44e-9 Pa^{-1}) and is used explicitly in the poroelastic formulation. The flow field is initially at steady state, so that the term H may be defined as the change in hydraulic head such that the well outlet boundary becomes the decline with hydraulic head. The boundary conditions imposed on fluid flow field are shown in Figure 4-17. Pumping from the lower aquifer outlet drops the hydraulic head by 5 m per year over a pumping period of 10 years.

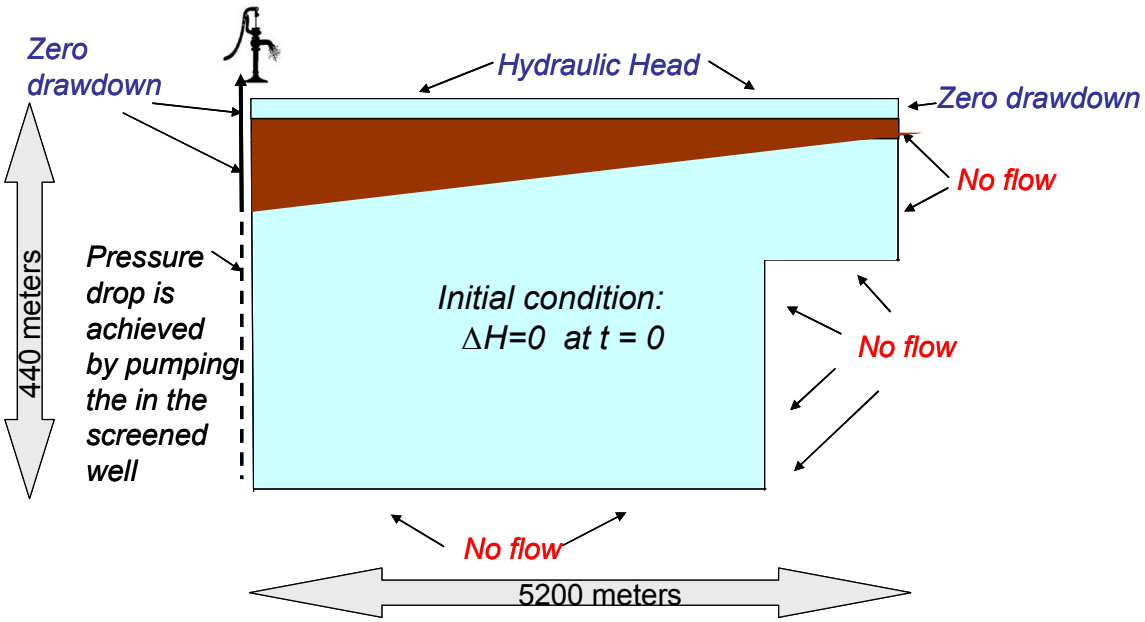

Figure 4-17. Boundary conditions imposed on fluid flow for the hydrogeologic system. For clarity, the vertical scale has been exaggerated.

The boundary conditions imposed on the system are such that horizontal and vertical movement is allowed at the surface and within the domain. The sides are not allowed to move horizontally, but are free to shift vertically. The base of the sediments is fixed and constrained to zero displacement in both directions. Figure 4-18 illustrates these boundary conditions imposed on displacements. The problem domain is meshed into 2030 triangular elements, with finer elements at the pumping boundary, along the bedrock step, and in the upper aquifer (Figure 4-19). The time-dependent solver is used for a transient simulation with a 10-year test period.

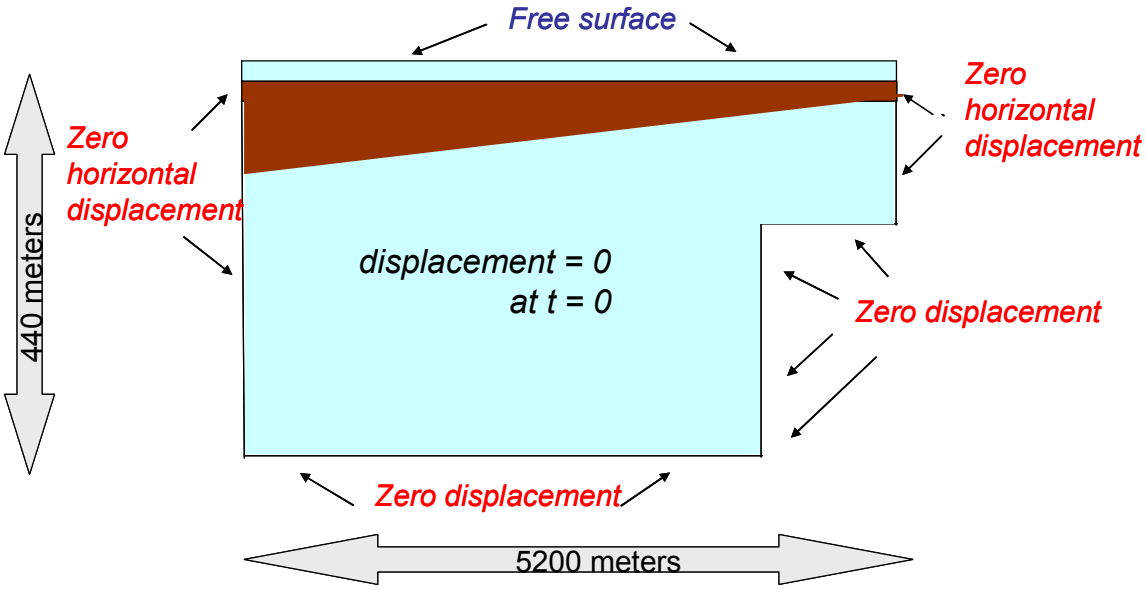

Figure 4-18. Boundary conditions for displacements imposed on the hydrogeologic system. For clarity, the vertical scale has been exaggerated.

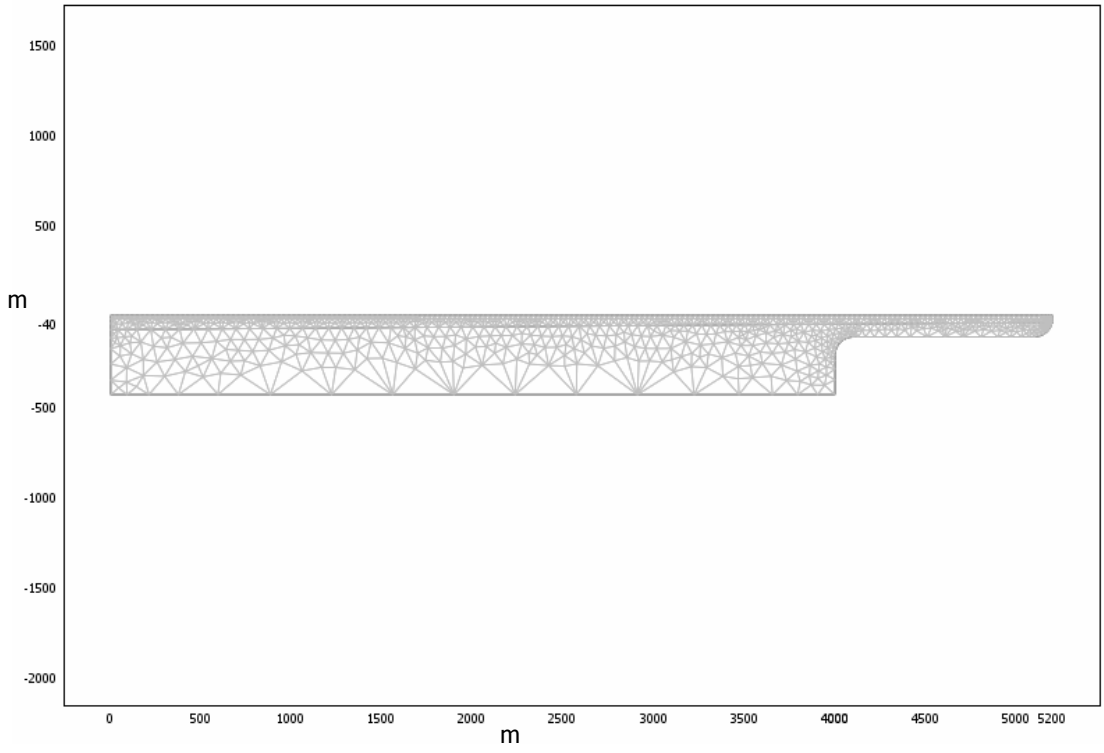

Figure 4-19. Finite mesh of the hydrogeologic system containing 2038 elements.

4.5.2 Model Results and Discussion

Figure 4-20 shows the von Mises stress distribution through the hydrogeologic system after approximately 10 years of pumping the lower aquifer. The stresses increase notably over the bedrock step, an indicator of potentially fracturing and fissuring. The fluid streamlines indicate the travel paths. There are abrupt changes in direction and flow velocity due to the bedrock step. The deformed shapes illustrate that the total displacements do in fact have a horizontal component.

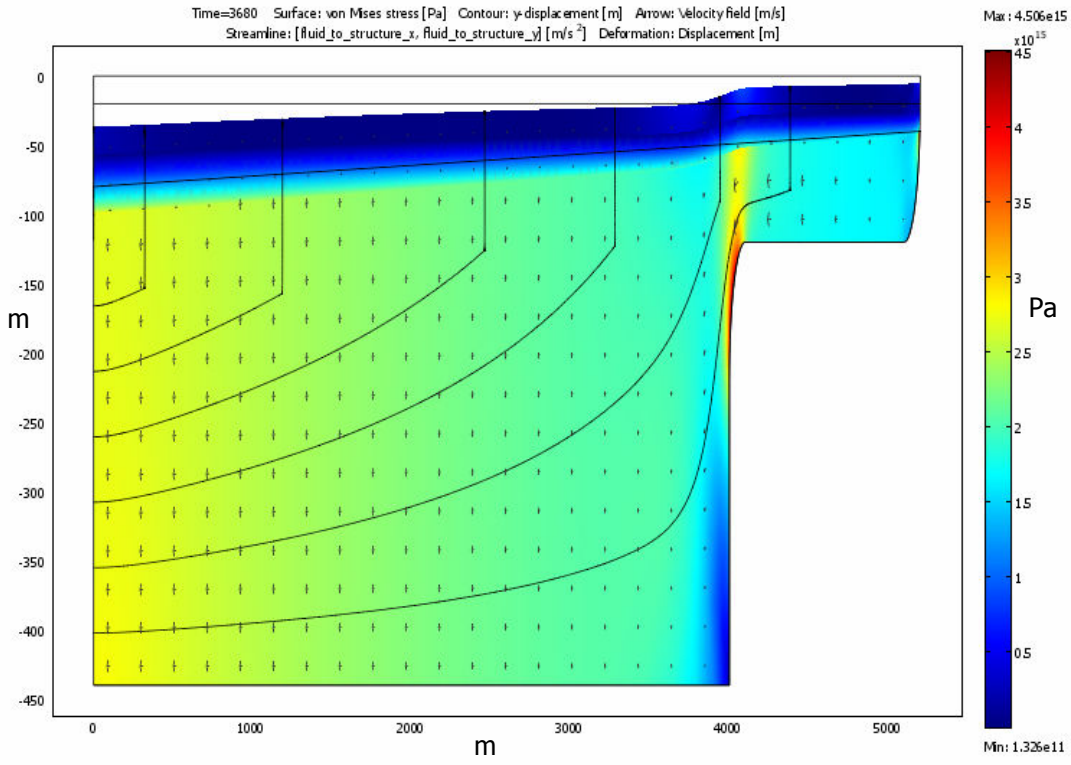

Figure 4-20. von Mises stresses (Pa), fluid streamlines, fluid velocities (vectors), and deformation (m) shown for 3860 days. Dimensions are in meters. The vertical axis has been exaggerated for clarity.

The horizontal strains (ux) at the ground surface are shown in Figure 4-21. Negative strains indicate compression and positive strains indicate tension. They illustrate the fact that lateral deformations compensate for the changing surface elevation. This coupling of strain-displacement is not seen with a simple Terzaghi consolidation formulation.

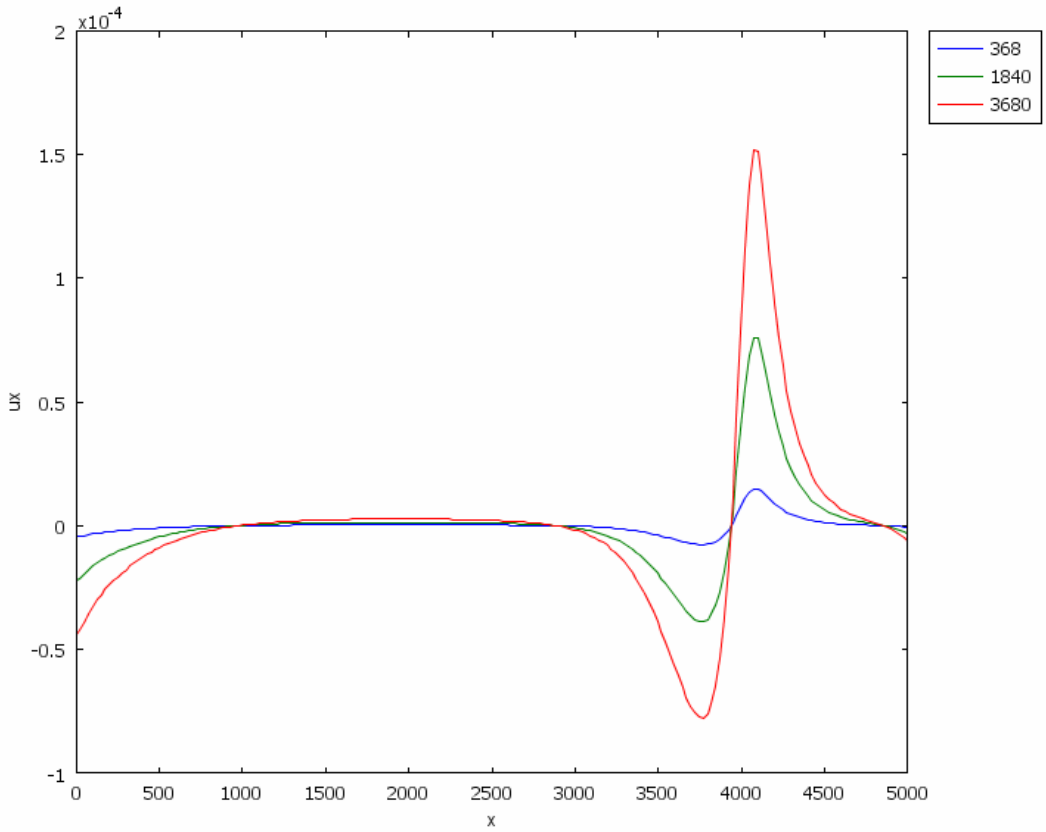

Figure 4-21. Horizontal strain predicted from at the ground surface for ~1 year (blue), ~5 years (green), and ~10 years (red). The range (x) is in meters and strain (ux) is dimensionless.

Figure 4-22 illustrates how the poroelastic simulation differs from a Terzaghi-based formulation. The solid lines indicate the uncoupled Terzaghi consolidation approach to calculating displacements (i.e., no horizontal displacements allowed), while the dashed lines indicate the fully-coupled poroelastic formulation. Towards the center of the basin, the solutions are in general agreement. However, in the regions immediately adjacent to the well and especially near the bedrock step, the difference between the two coupling techniques is quite apparent. In fact, the poroelastic solution predicts displacement at the ground surface above the bedrock step. These results are in general agreement with the published results of Leake and Hsieh (1997) who used a mixed finite-element/finite-difference approach, as shown in Figure 4-23.

At early times, the hydraulic head in the upper aquifer actually rises in response to pumping of the lower, confined aquifer (Figure 4-24). This behavior can only be

explained by the poroelastic coupling. The spike is most dramatic near the well. The effect eventually disappears, and the hydraulic head actually begins to dissipate slowly as a result of the drawdown through the relatively impermeable aquitard.

In general, the fully-coupled poroelastic solution validates the Terzaghi model approach. However, the poroelastic approach is needed to accurately simulate the vertical and horizontal deformation, which can be used to calculate horizontal strains that may lead to fissuring or displacements at the surface.

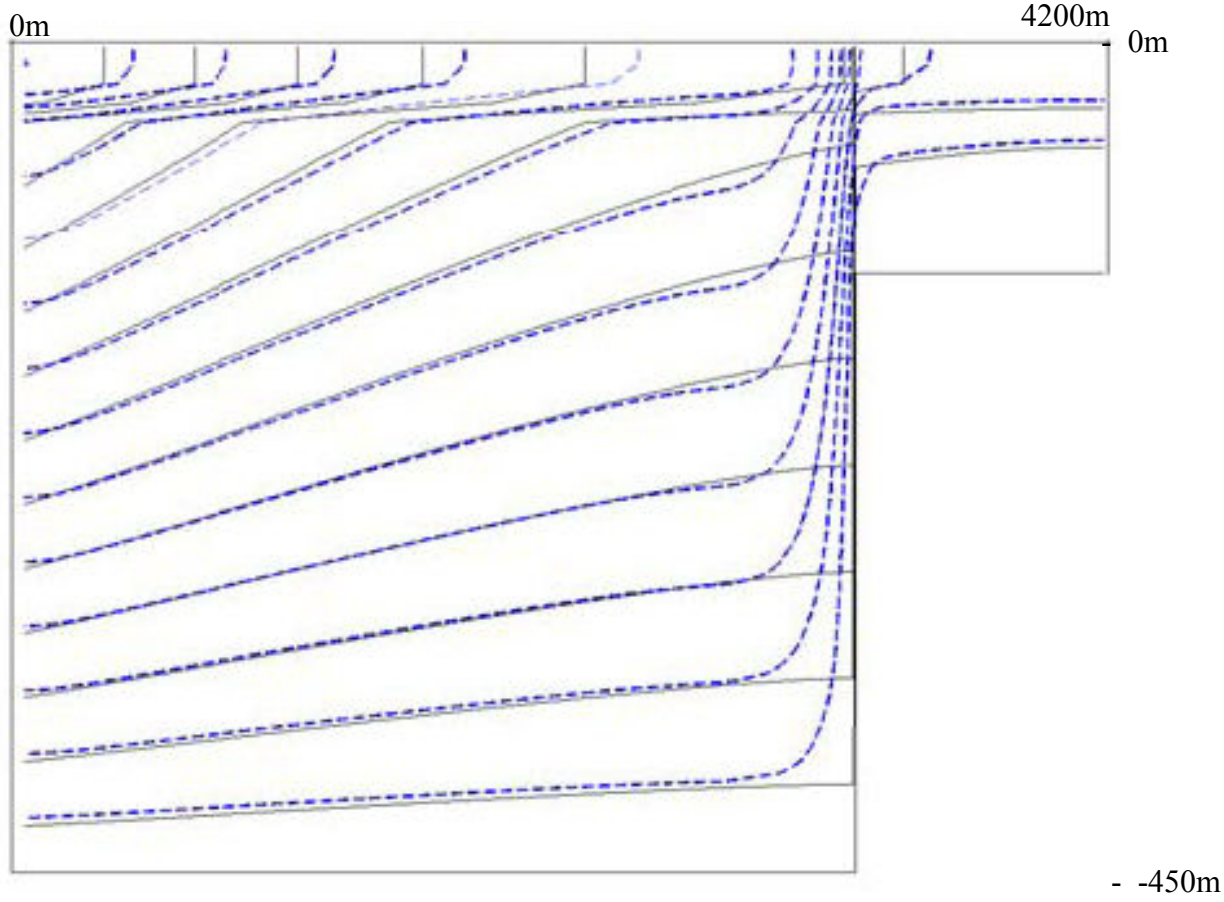

Figure 4-22. Displacements predicted by the fully-coupled poroelastic analysis (dashed lines) vs. Terzaghi's consolidation equation (solid lines). The vertical scale has been exaggerated.

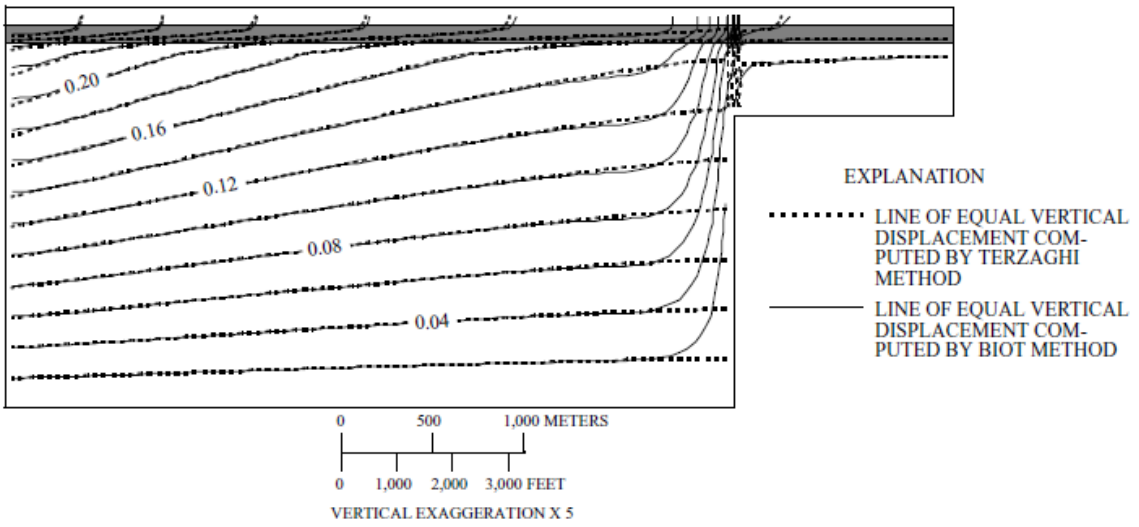

Figure 4-23. Results of simulations of flow and deformation using the Terzaghi and Biot methods for computed vertical displacements. (from Leake and Hsieh, 1997)

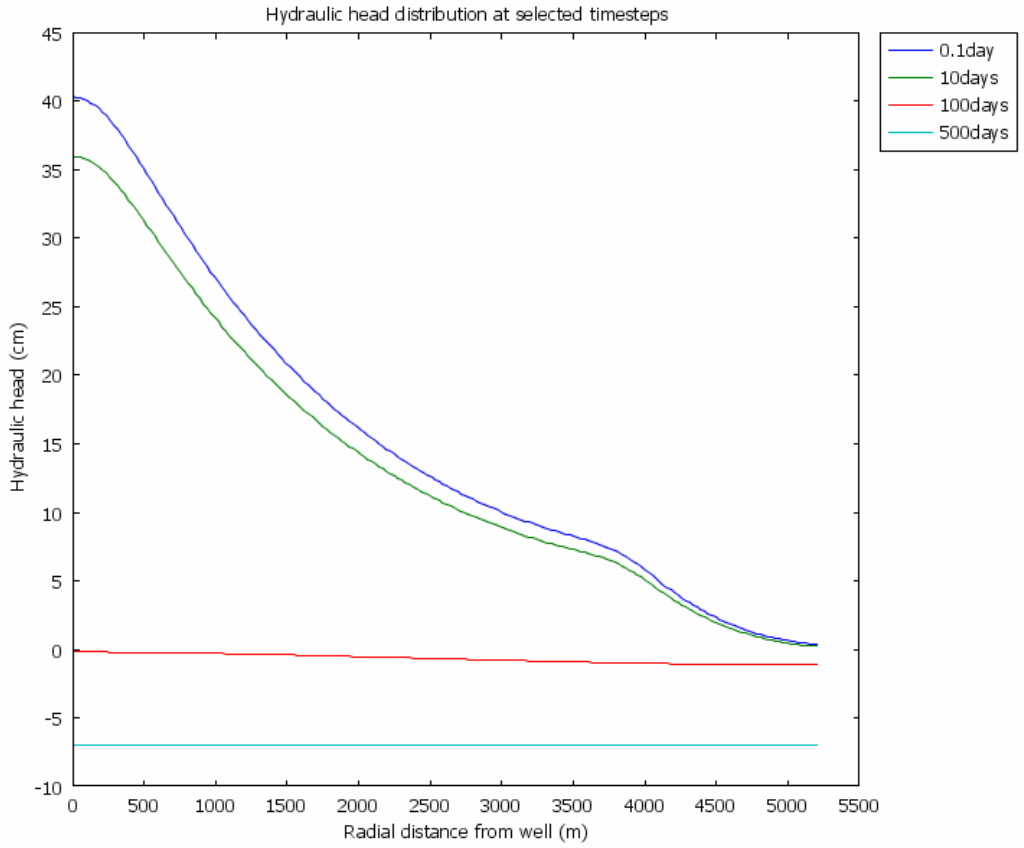

Figure 4-24. Early times at 0.1 day (dark blue), 10 days (green), and 100 days (red) show the hydraulic head reversal effect along the surface of the upper aquifer (which is not pumped directly). This effect disappears in later times (500 days, light blue) as the head drops in response to prolonged pumping of the lower aquifer.

4.6 4-D Reservoir Simulation Tied to Modeling Changes in Seismic Velocities

Accurate measurements and surveillance of reservoir properties in both the field and the laboratory are difficult and costly (Sarkar et al., 2003; Herwanger and Horne, 2005). Attempts have been made to simulate critical production scenarios through poroelastic continuum models. Analytic solutions have been proposed, but are only applicable under certain assumptions (e.g., homogeneity, single-phase fluid saturation, uniform pressure drops, etc.), and are restricted to certain geometries usually in 1-D and 2-D (Fuck, 2001; Fuck, 2007). More realistic numerical models have been developed (e.g., Dean et al., 2006) linking fluid flow to geomechanics. However, considerable effort is needed to interface the different computational schemes that handle each governing equation and tie the results to changes in seismic velocities. Grechka and Soutter (2005) and Lewis and Schrefler (1998) suggest a unified finite element platform for directly modeling shear and fast compressional wave velocity changes from a geomechanically-coupled fluid flow model.

This thesis work extends this basic formulation for implementation in Comsol 3.3a, the finite element modeling environment, from which both the fast and slow (Biot) compressional and shear wave velocities are computed at each time step from a coupled flow model. In this model, all of the relevant constitutive relations and governing equations were added manually through Comsol's PDE coefficient mode. Using a nonlinear elastic formulation, a 4-D fully-coupled simulation of reservoir production is developed for directly modeling changes in seismic velocity changes. A summary of the nonlinear elastic formulation is given in Appendix B. Given particular initial and boundary conditions for an unstressed reservoir, geomechanics and two-phase fluid flow are solved together and simultaneously in a transient analysis. Finally, the sensitivity of the model to two key input parameters, porosity and permeability, is analyzed.

4.6.1 Model Description

Since reservoir production may induce stress effects in distal non-reservoir zones, a sufficiently large host domain is needed to characterize the coupled geomechanical interaction between the producing interval and under- and overburden. Two subdomains

are defined for this model: a producing reservoir within a host formation 400 times larger in volume (Figure 4-25). Reservoir fluids (water and oil) are withdrawn at a rate of 8600 barrels/day from a well with a radius of 0.1 m (~8 in.) and a height of 50 m (~164 ft). Continuous production is simulated for five years. Additionally, after the first two years of production, water is injected at a rate of 2800 barrels/day through a source well having the same dimensions as the sink.

The unstressed material properties were selected to represent a high-porosity, unconsolidated sandstone reservoir surrounded by a stiffer shaly sandstone host rock (Table 4-5). The specific values were compiled from a number of references in the literature (Winkler and Liu, 1995; Mavko et al., 2003; Sarkar et al., 2003; Prioul et al., 2004; Grechka and Soutter, 2005).

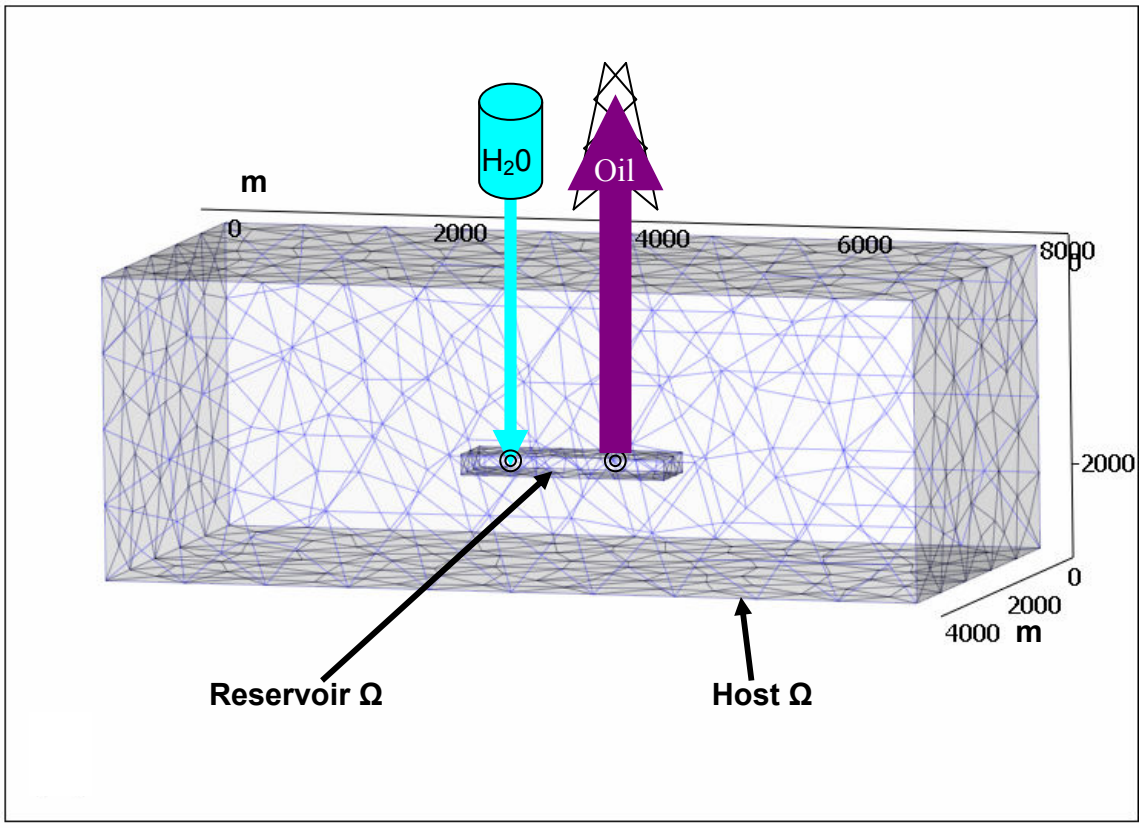

Figure 4-25. Two subdomains for the 3-D finite element mesh.

The overall finite element mesh requirements are relaxed to ensure the stability of Comsol's time-dependent solver during multiple model simulations needed for the parametric sensitivity analysis. The total number of elements is 1200. Both subdomains are meshed using second-order Lagrangian tetrahedral elements. The finite element meshing is made finer around and within the reservoir domain to accommodate the higher stress gradients.

Table 4-5. Unstressed material properties used in the 3-D finite element model.

Symbol	**Units**	**Reservoir Ω**	**Host Ω**
$V_{p\text{-}solid}$	m/s	2300	3000
$V_{s\text{-}solid}$	m/s	900	1100
$V_{p\text{-}water}$	m/s	1500	1500
$V_{p\text{-}oil}$	m/s	1700	1700
ρ_{solid}	kg/m^3	2100	2100
$c^{(3)}111$	Pa	−2.8e12	−1.5e12
$c^{(3)}112$	Pa	−1.2e12	−0.3e12
$c^{(3)}123$	Pa	0.8e12	0.1e12
φ_0	[dimensionless]	0.05 – 0.45	0.10
g	m/s^2	9.81	9.81
k_{perm}	m^2	1e-11 – 1e-14	1e-16
ρ_{oil}	kg/m^3	940	940
ρ_{water}	kg/m^3	1000	1000
kinematic-$visc_{oil}$	m^2/s	0.5e-6	0.5e-6
kinematic-$visc_{water}$	m^2/s	5.0e6	5.0e6
K_{water}	Pa	2.25e9	2.25e9
K_{oil}	Pa	2.72e9	2.7e9
α (Biot-Willis)	[dimensionless]	0.9	0.9

The governing equations for coupling two-phase fluid flow to reservoir geomechanics and seismic velocities are discussed in detail by Lewis in Schrefler (1998)

and Prioul et al. (2004) are summarized in the Appendices. The core Matlab expressions, which are loaded and run in the Comsol 3.3a finite element environment, are also given in the Appendices.

The initial steady-state conditions are specified for water and oil component pressures under hydrostatic gravity loading (i.e., pressure as a function of the integrated fluid density column, ρgz). The gravity loading of the solid component is governed by integrated bulk rock density and second- and third-order stiffness coefficients (Winkler and Liu, 1995; Sarkar et al., 2003; Prioul et al., 2004). The porosity changes as a function of initial porosity and volumetric strain, such that $\phi = 1-(1-\phi_0)e^{-\varepsilon}$.

The boundary conditions for the system are specified such that there are zero shear stresses and zero fluid flux at the top surface of the host subdomain. The top surface allows for free displacement. There are zero normal solid displacements and zero fluid fluxes at all other faces of the subdomain.

The solutions to the fluid pressures and solid displacements in the steady state (dp/dt=0 and du/dt=0) are the initial conditions for the transient fluid flow analysis. Immediately after t=0, the pumping well is activated and pumps a mixture of reservoir fluids (oil and water). At t=2 years, the water injection well is activated. The two-phase fluid flow drives the changes in pore pressure, stress state, and solid deformation. These changes are potentially detectable from apparent time-shifts of seismic data. From this fully coupled approach, compressional and shear wave velocities can be computed directly from strains linked to the changing stress state within and around the reservoir. The relationship between vertical Vp and strain is shown in Figure 4-26 (in the overburden and surrounding host rock) and Figure 4-27 (within the reservoir). The dilation factor "R" is a measure of the relative change in velocity to strain. It is used in time-lapse seismics to infer reservoir deformation (e.g., Hatchell and Bourne, 2005).

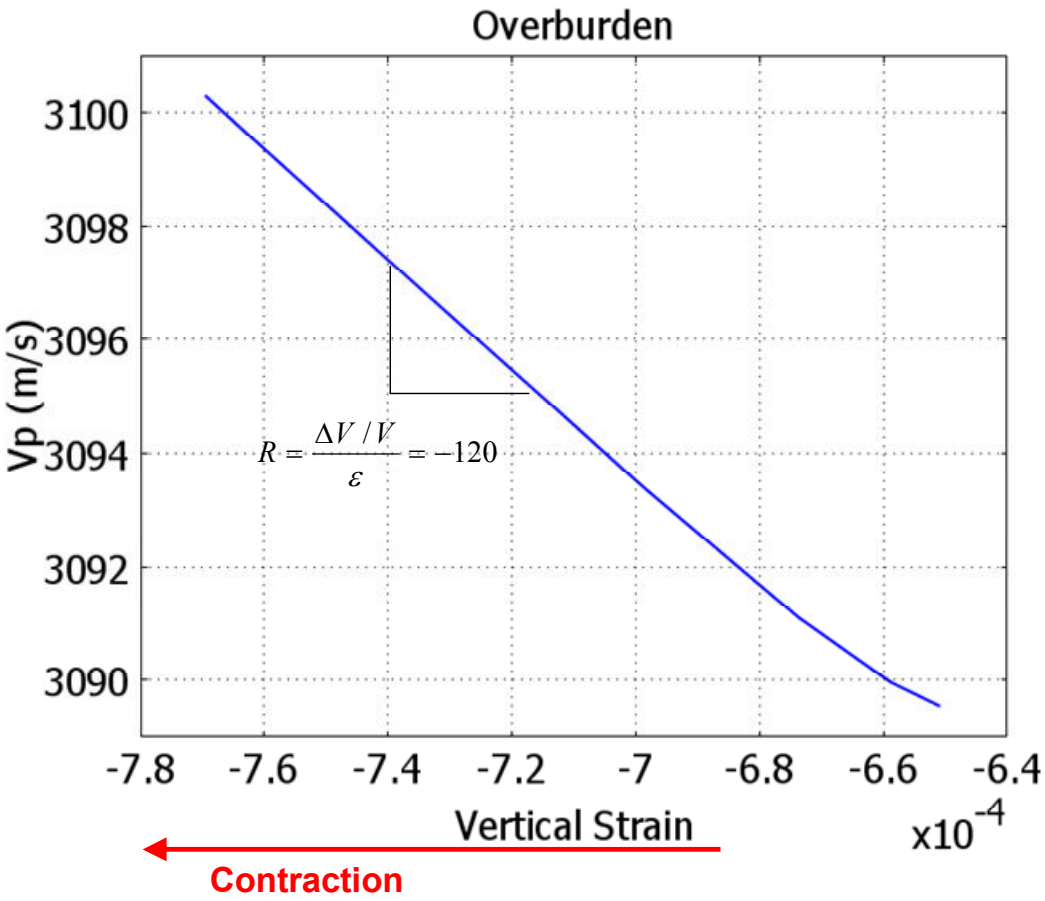

Figure 4-26. Relationship between vertical Vp and strain in the overburden and surrounding rock. In this study, strain is negative for contraction and positive for tension. The dilation factor "R" is the ratio of relative change in velocity to strain.

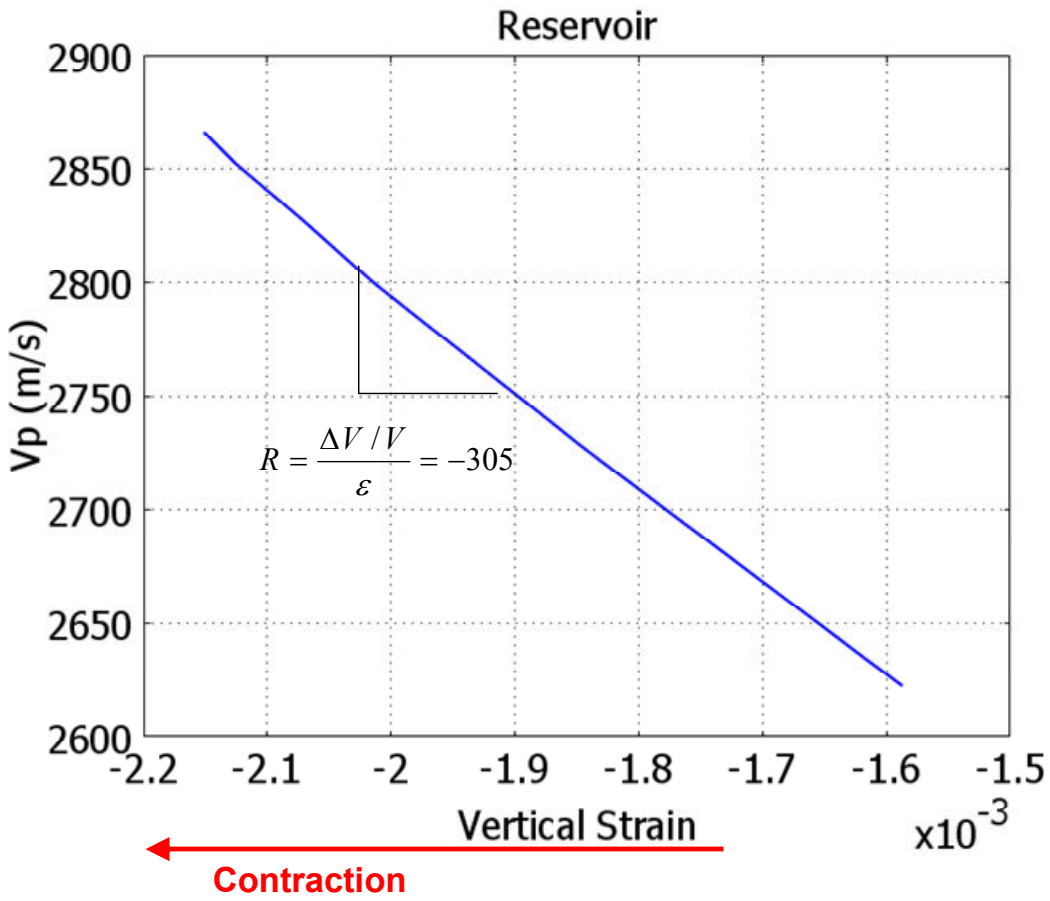

Figure 4-27. Relationship between vertical Vp and strain within the reservoir. In this study, strain is positive for contraction and negative for tension. The dilation factor "R" is the ratio of change in velocity over initial velocity to strain.

4.6.2 Model Results

The model results may be represented in a number of ways in 3-D and 4-D. For simplicity, data profiles along a cross-line intersecting both the pumping and injector wells are shown (Figure 4-28). The results for the base case are presented first, with reservoir porosity set to 40% and reservoir permeability set to 1e-12 m^2 (~1 Darcy).

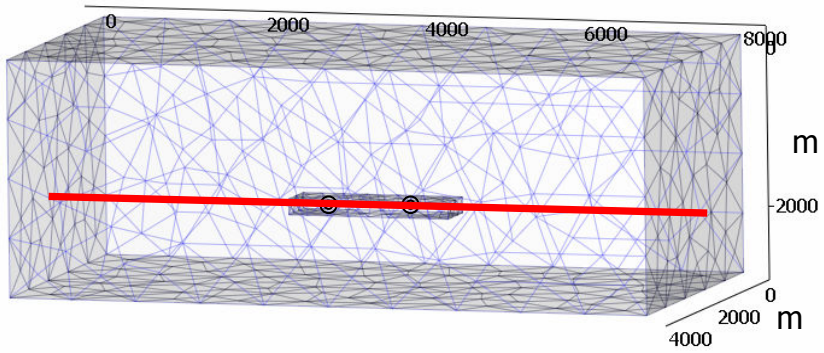

Figure 4-28. Location of the horizontal cross-line (dimensions in meters).

The vertical effective stress profile along the horizontal cross-line is plotted at different time stages of production in Figure 4-29. At t=0, the system is loaded by gravity and the initial fluid pressures. The sign convention followed here is that negative vertical stress represents compression, and a positive vertical stress would be extension. The magnitude of compression increases in the host rock approaching the reservoir from left to right. The stress changes in the surrounding host formation is a phenomena known as "stress arching" (e.g., Dusseault et al., 2007). Upon crossing the reservoir boundary (y=3000 m), the material changes and there is a sudden corresponding change in stress. The most pronounced change in compressional stresses is in the first year of production. At t=5 years, the change in stress from the previous year diminishes, indicating that stress-sensitivity of the system has stabilized. The profile is asymmetrical (about the line y=4000 m) due to the locations of the extraction well (y=4500 m) and the injection well (y =3500 m).

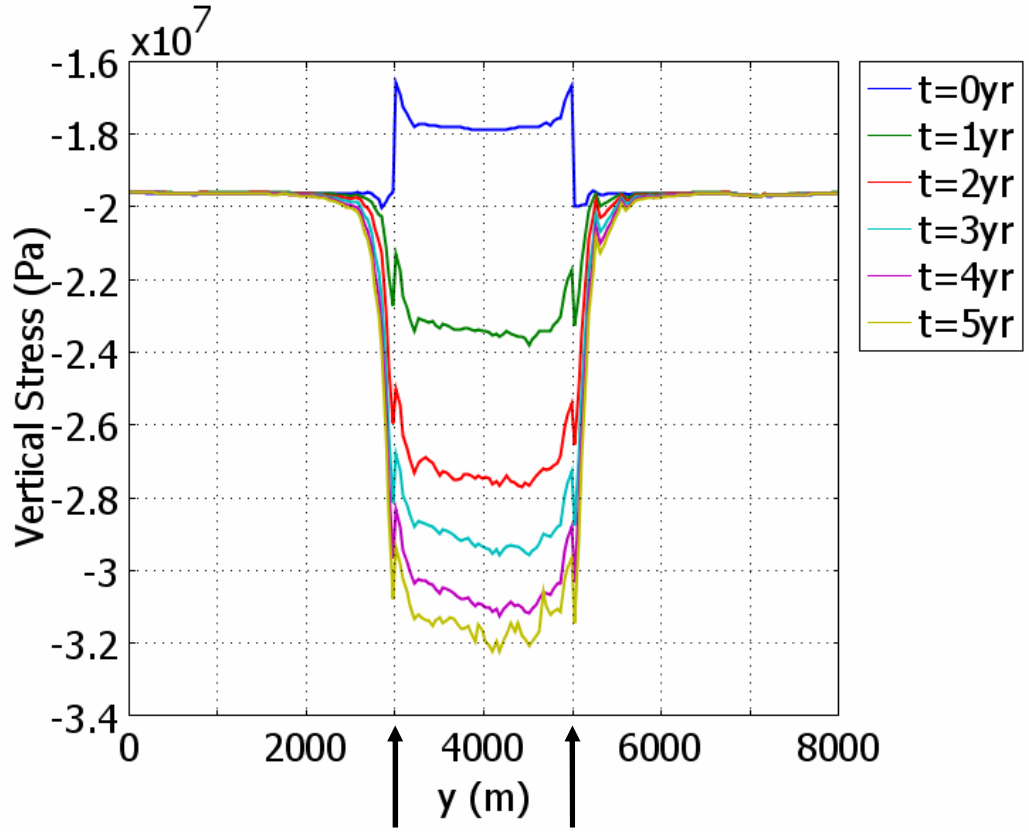

Figure 4-29. Profile of effective (solid frame) vertical stress (Pa) along a horizontal cross-line shown in Figure 4-28. The profile is not symmetric since the production well is located at y=4500 m and the injector well is located at 3500 m. The arrows indicate the boundaries of the reservoir.

Similarly, modeled vertical compressional wave velocities (V_p) are computed at different time stages of production in Figure 4-30. Approaching the reservoir boundary, the velocity profile increases in the host domain. Crossing the boundary into the reservoir, there is a material properties change (Table 4-5), which is manifested as a dip in the velocity profile. The profile plateaus within the middle of the reservoir as a result of gravity and fluid loading. In the first and second years of production only (green and red lines), the velocity changes are more pronounced than in the following years after the injector well is activated. The velocity profile is responding to stress changes induced by production. The profile is not symmetrical due the locations of the wells. In the first two years, the highest peaks of velocity in the reservoir coincide with the location of the production well (y=4500 m). A vertical slice through the reservoir (at x=2000 m) shows the change in the compressional wave velocity from t=0 to t=5 years in Figure 4-31.

Contraction within the reservoir causes the velocity to increase, while above and below the reservoir, the velocity decreases due to dilation. The V_p/V_s ratio plotted as a function of depth (z) is shown in Figure 4-32. The results relate to the changes in deformation from the (unconsolidated) seafloor bottom (z=0 m) to the reservoir (z=-2000 m) and to the underburden (z=-3000 m).

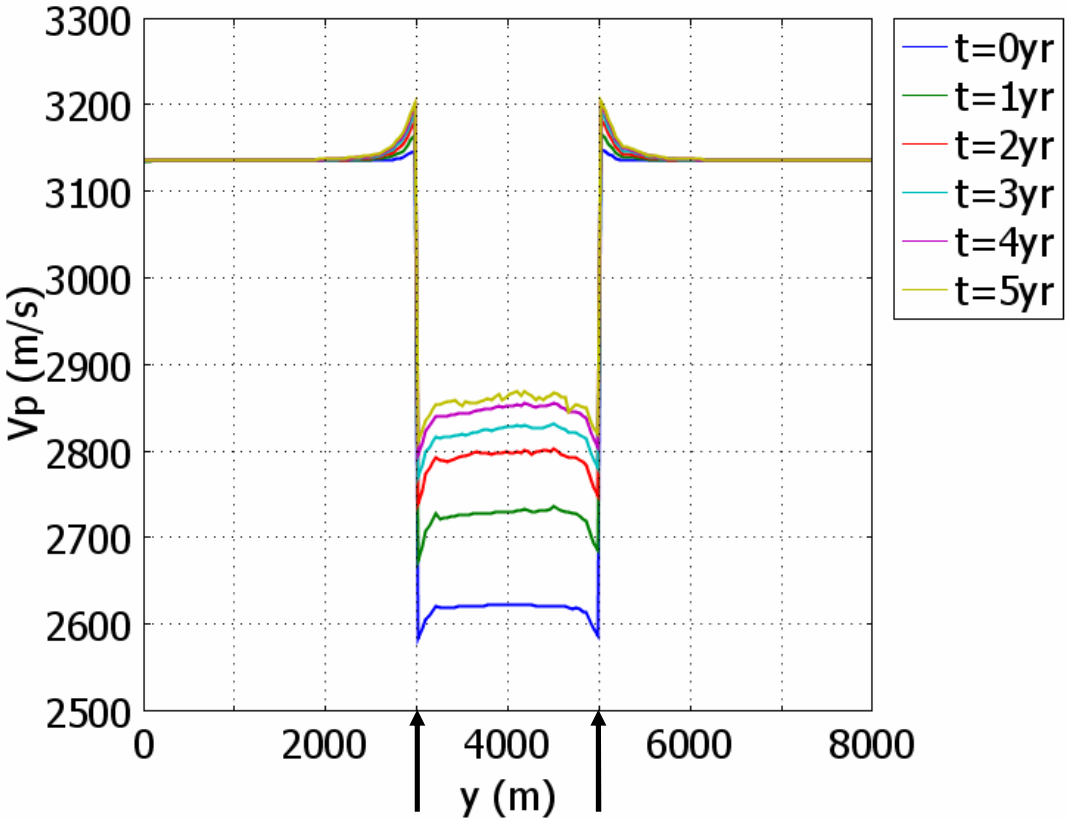

Figure 4-30. Vertical compressional wave velocity (V_p) profiles. The profile is not symmetric since the production well is located at y=4500 m and the injector well is located at 3500 m. The arrows indicate the boundaries of the reservoir.

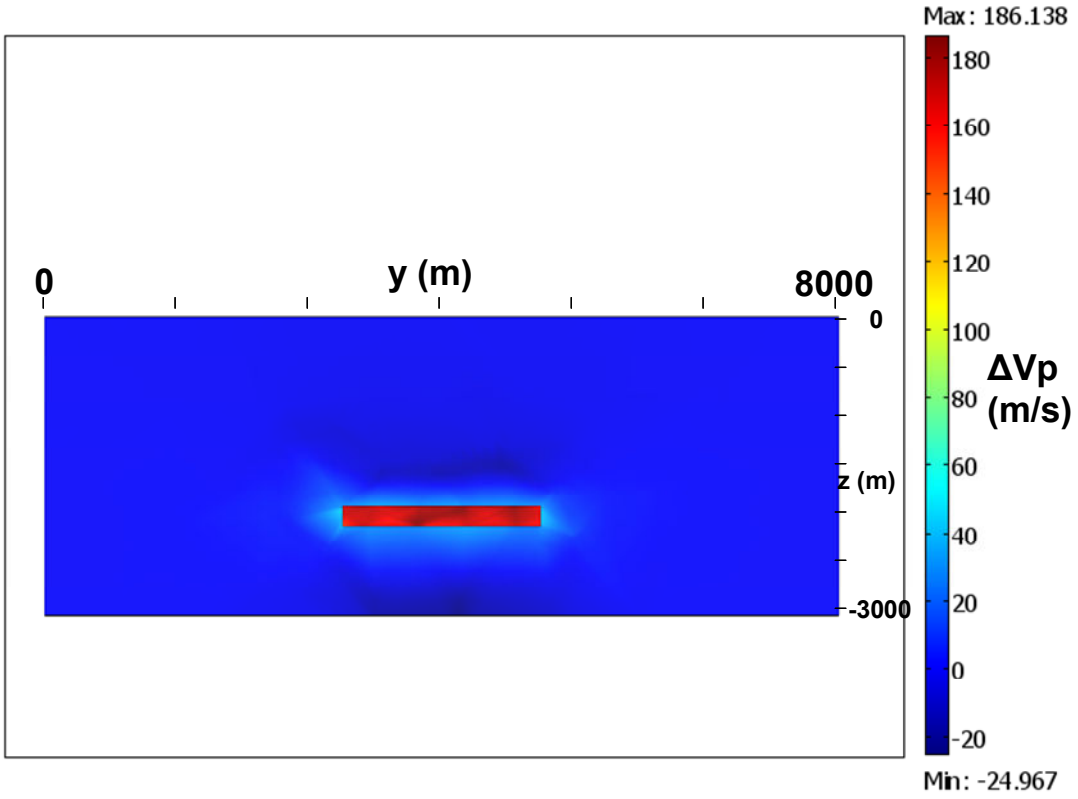

Figure 4-31. Change in V_p from t=0 to t=5 years plotted on a vertical slice (x=2000 m). Reservoir permeability is 1e-12 m^2 and reservoir porosity is 0.40. Dilation is occurring in the under- and over-burden (dark blue cool color) and contraction is occurring within the reservoir (warmer colors).

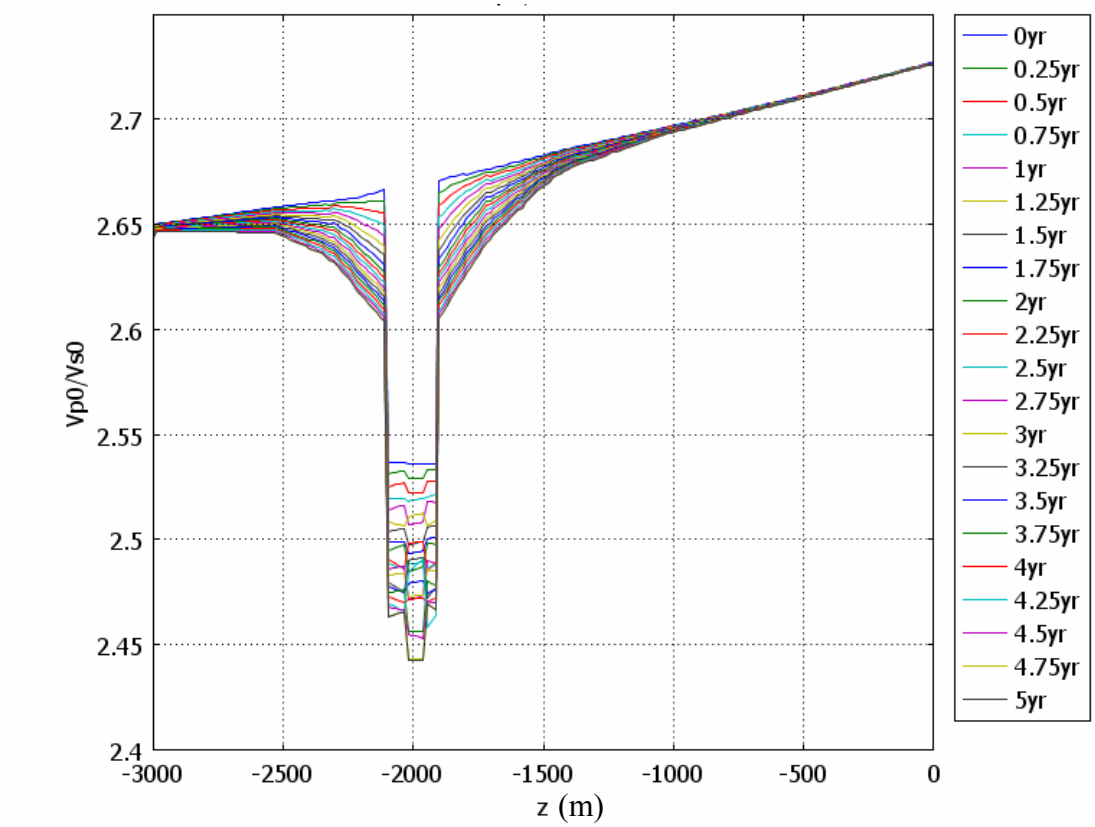

Figure 4-32. Vertical Vp/Vs ratio profile with depth (z). Permeability of the reservoir is 1e-12 m^2 and reservoir porosity is 0.40. All other parameters are as listed in Table 4-5.

To illustrate the role of strain within and surrounding the reservoir, the change in vertical strain (ε_{33}) between t=0 and t=5years is plotted on a vertical slice (x=2000) through the host and the reservoir in Figure 4-33. The cooler, negative colors indicate compression within the reservoir. The warmer, positive colors indicate dilation above and below the reservoir. This profile is consistent with the idealized conceptual understanding shown in Figure 1-3 and in previous analytical results (Calvert, 2005; Fuck, 2007).

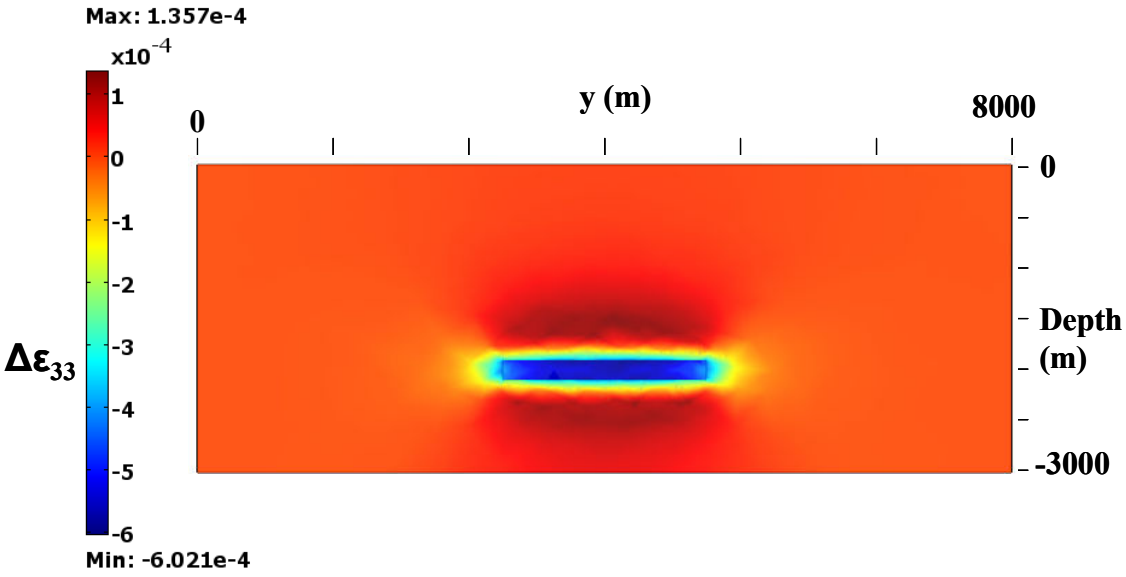

Figure 4-33. A profile slice (x=2000 m) of the change in vertical strain ε_{33} between t=0 and t=5 years. Warmer, positive colors indicate dilation. Cooler, negative colors indicate compression.

The slow (Biot) compressional velocity (VpSlow) is a dispersive, attenuating wave (Zhu and McMechan, 1991). The velocity is computed using an empirical function of tortuosity and the compressional-wave velocity of the pore fluid mixture. The expression is given in Appendix B. In Figure 4-34, the change in VpSlow from t=0 to t=5 years is shown in a vertical slice through the modeling domain. The change in fluid content is the main cause of the polar anomalies around the two wells. Increasing reservoir porosity is expected to increase VpSlow and decrease the fast vertical compressional-wave velocity, Vp0. The profiles of the slow velocity are given in Figure 4-35 and Figure 4-36 for different initial reservoir porosity and permeability. It is sensitive to changes in porosity, given that a minimum permeability is used. In laboratory studies (Woolley, 2004), the experimental detection limit was found to be 137 mD and higher.

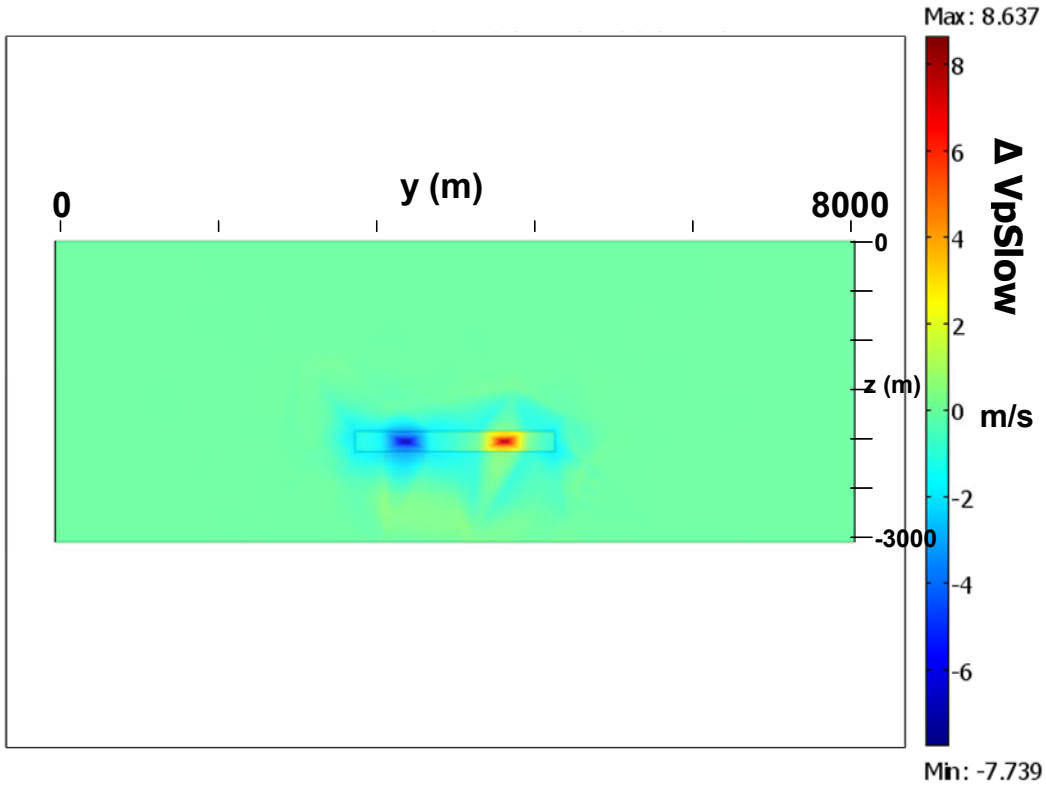

Figure 4-34. A vertical slice through the modeling domain showing the change in VpSlow from t=0 to t=5 years. The initial reservoir porosity is 0.45 and reservoir permeability is 1e-12 m^2. All other parameters are as listed in Table 4-5.

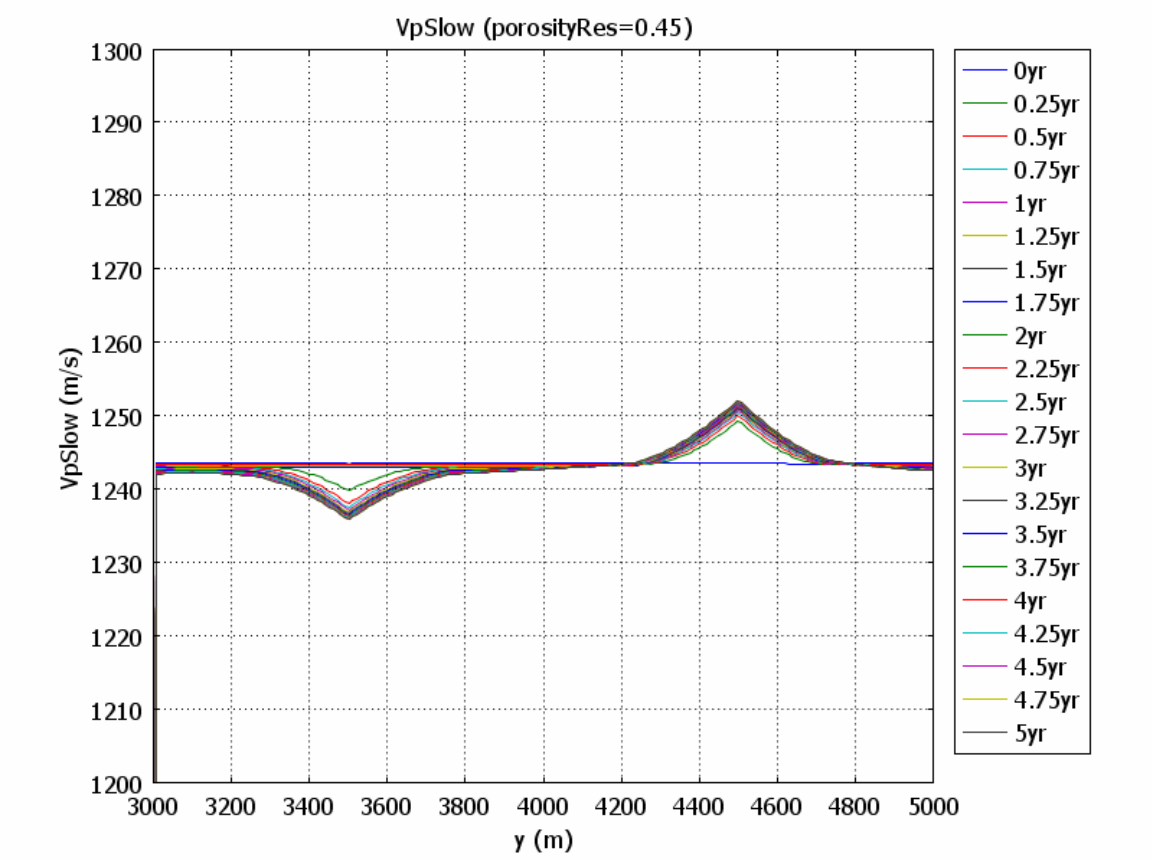

Figure 4-35. The compression slow (Biot) velocity profile. Reservoir porosity is 0.45 and reservoir permeability is 1e-12 m^2. All other parameters are as listed in Table 4-5.

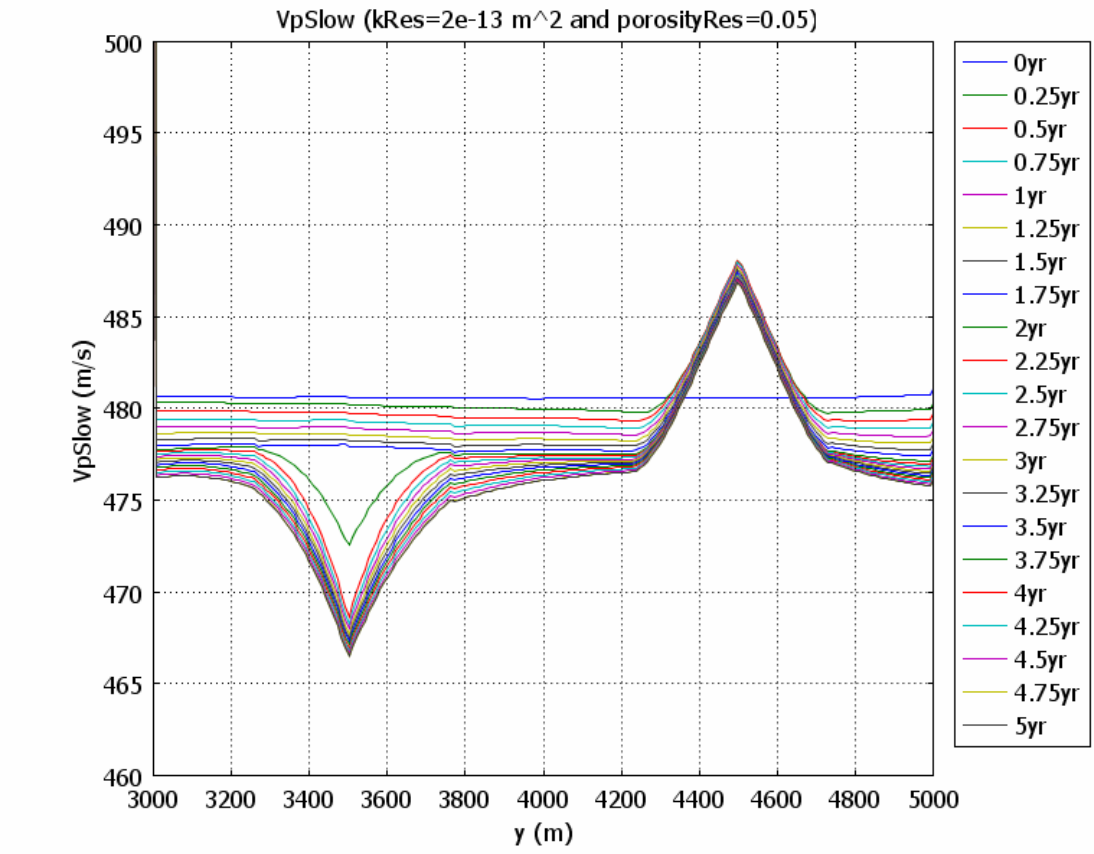

Figure 4-36. VpSlow profile where reservoir porosity is 0.05 and reservoir permeability is 2e-13 m^2. All other parameters are as listed in Table 4-5.

Dimensionless anisotropic parameters (ε and δ) and the shear-wave splitting coefficient (γ) (Thomsen, 1986) can be directly computed from the stiffness tensor. The Thomsen parameters ε and δ define the fractional difference between horizontal and vertical P- and S_H-wave velocities, respectively. In Figure 4-37, the change in the epsilon anisotropic parameter, ε=(c11-c33)/(2c33), from t=5 to t=0 years is shown in a slice profile. The parameter increases in magnitude with ongoing production.

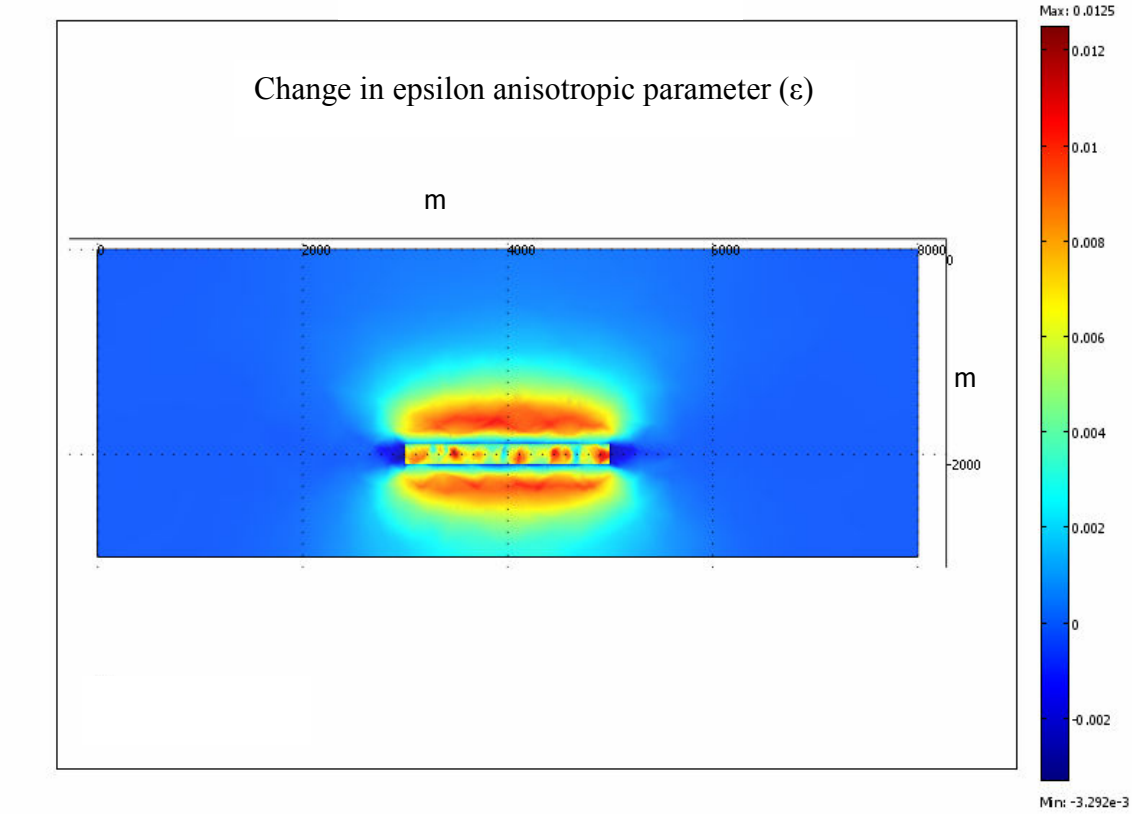

Figure 4-37. Change in the epsilon anisotropic parameter (ε) from t=5 to t=0 years.

4.6.3 Parameter Sensitivity

The sensitivity of the fully-coupled geomechanical model to changes in reservoir porosity and permeability are presented in this section. In Figure 4-38 to Figure 4-41, the total fluid pressure is plotted along the cross-line through the reservoir for a range of reservoir permeability values from kRes=1e-11 m^2 to kRes=1e-14 m^2 (~10 to 0.01 Darcy). The model simulations become unstable outside of this range. The initial porosity is set to 0.40 for each case. All other parameters are as specified in Table 4-1.

For each model run, the total fluid pressure has the same initial profile at t=0 (immediately before activation of the extraction well). After activation, the cones of pressure depression around the extraction well (y=4500 m) are more pronounced with the progressing time step. Pore fluid pressures are tightly linked to the specified initial reservoir permeability. By decreasing permeability, the cone of expansion around the

injection well (y=3500 m) is more pronounced (Figure 4-38 vs. Figure 4-41). The negative total fluid pore pressures in Figure 4-41 are an artificial effects of the model parameters imposed in this scenario. In reality, the volumetric flow rate from the production well would decrease, and would thus prevent the fluid(s) from making a phase change to gas (i.e., boiling).

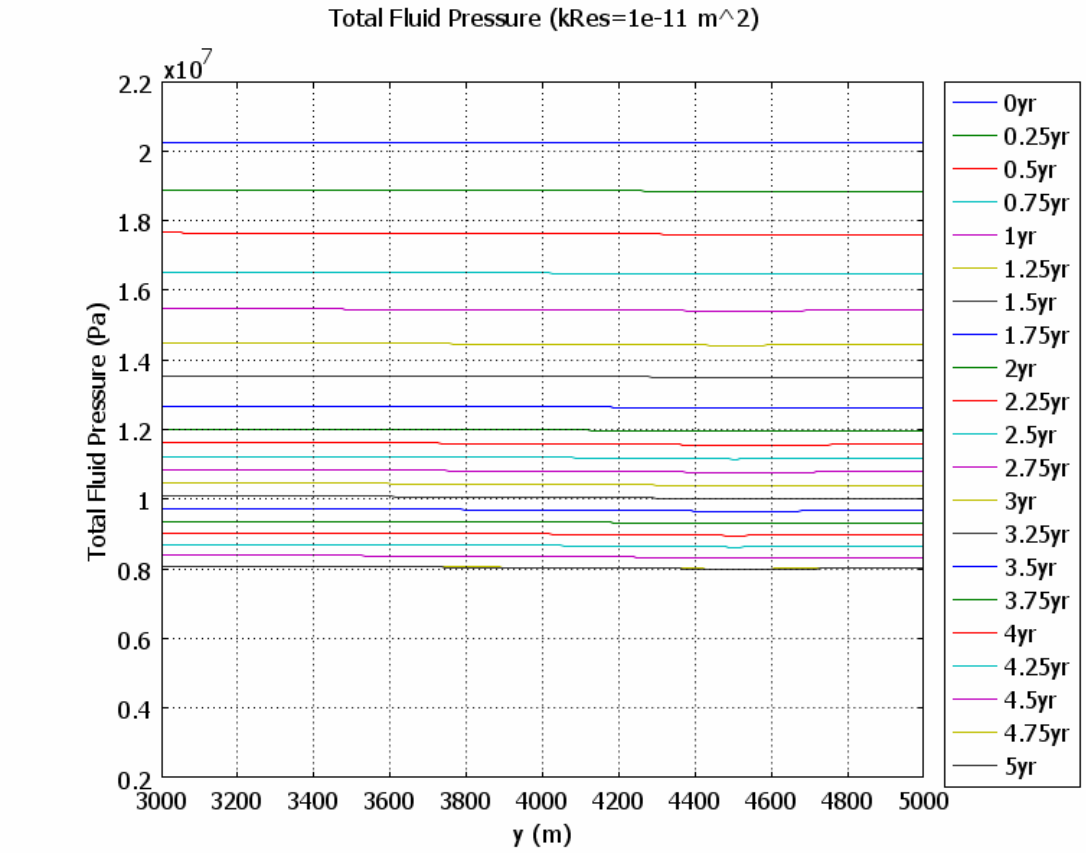

Figure 4-38. Total pore pressure profiles along a cross-line through the reservoir at different time stages. The parameter of interest is reservoir permeability: 1e-11 m^2 (~10 Darcy). The initial reservoir porosity is 35%. The producing well is located at y=4500 m and the injection well is located at y=3500 m.

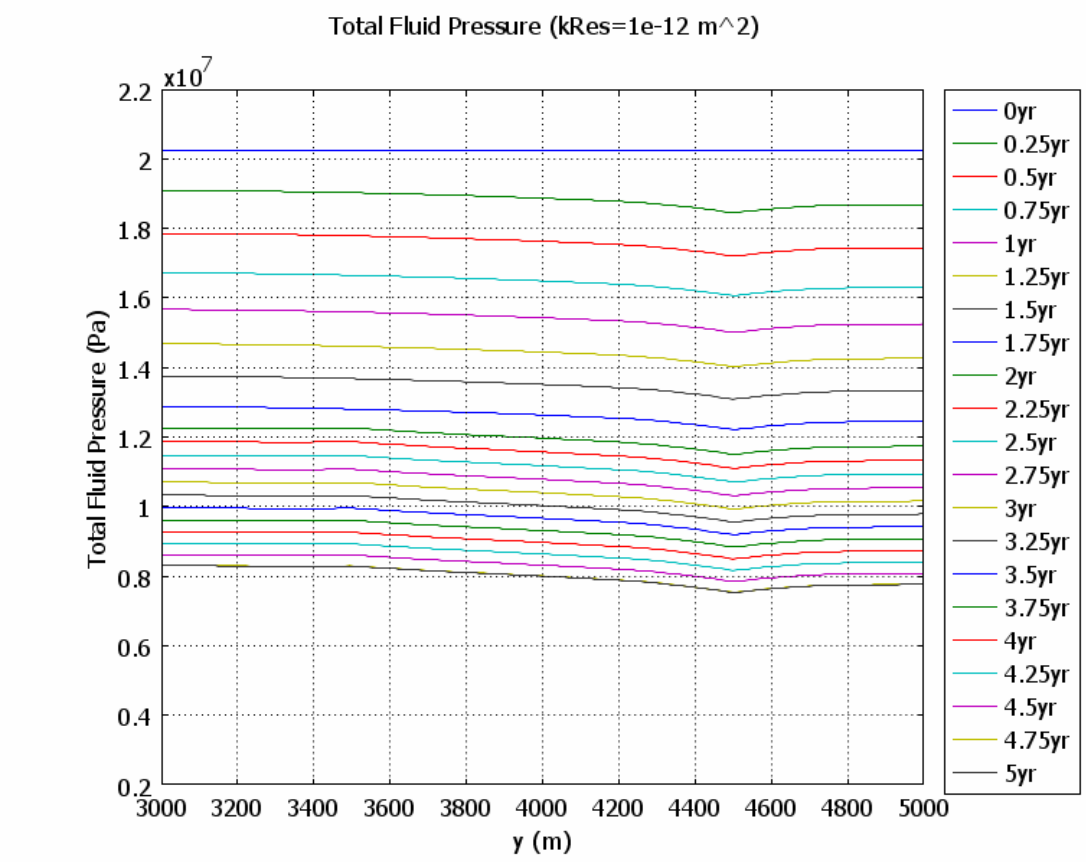

Figure 4-39. Total pore pressure profiles along a cross-line through the reservoir at different time stages. The parameter of interest is reservoir permeability: 1e-12 m^2 (~1 Darcy). The initial reservoir porosity is 0.40. The producing well is located at y=4500 m and the injection well is located at y=3500 m.

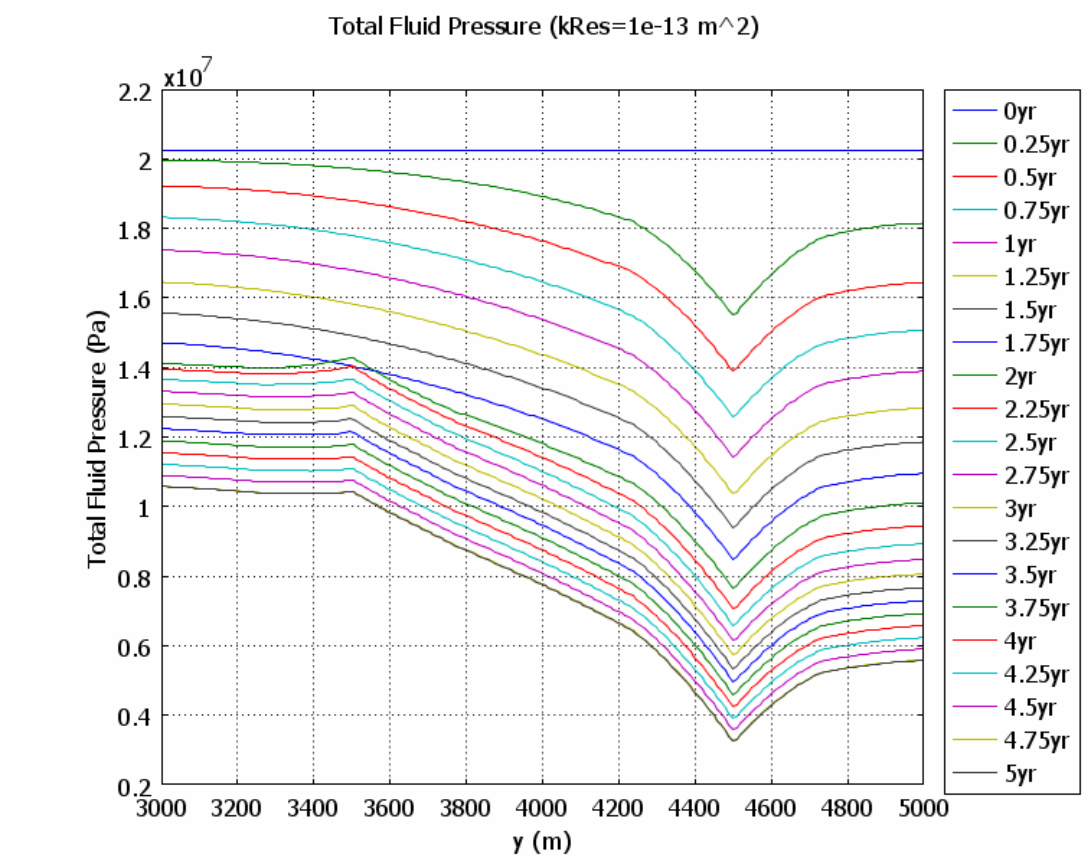

Figure 4-40. Total pore pressure profiles along a cross-line through the reservoir at different time stages. The parameter of interest is reservoir permeability: 1e-13 m^2 (~0.1 Darcy). The initial reservoir porosity is 0.40. The producing well is located at y=4500 m and the injection well is located at y=3500 m.

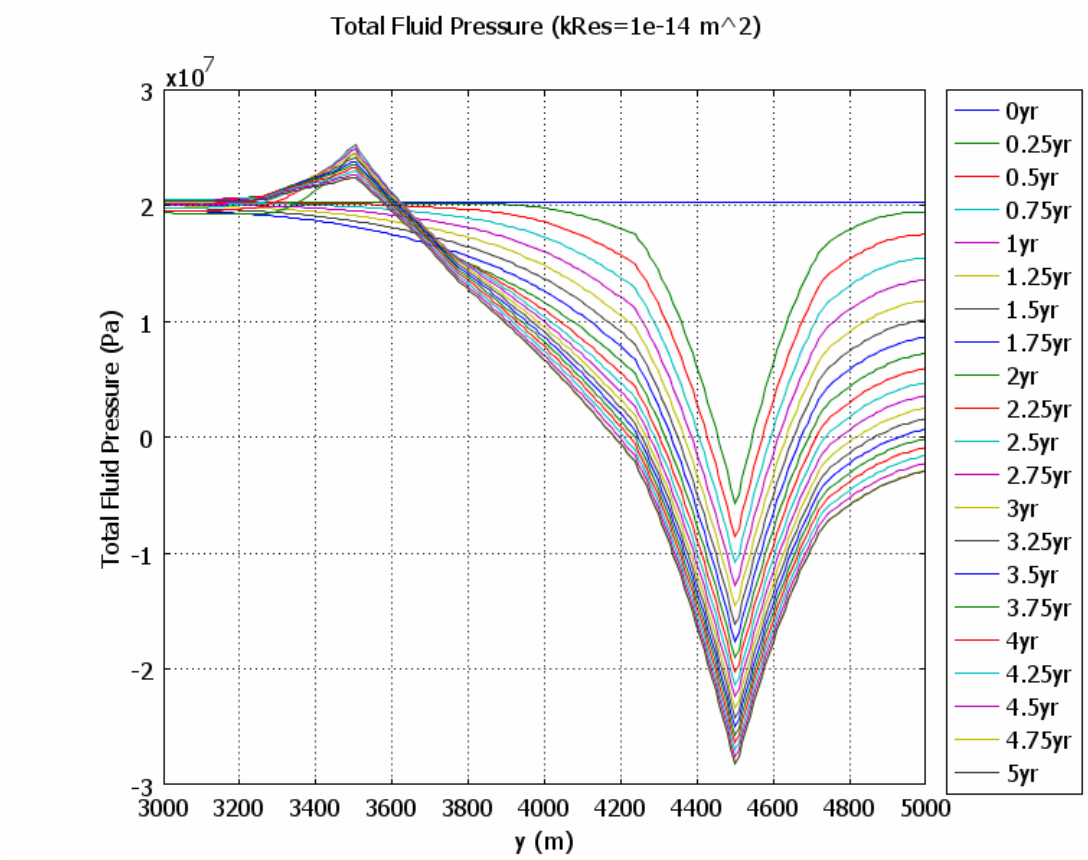

Figure 4-41. Total pore pressure profiles along a cross-line through the reservoir at different time stages. The parameter of interest is reservoir permeability: 1e-14 m^2 (~0.01 Darcy). The initial reservoir porosity is 0.40. The producing well is located at y=4500 m and the injection well is located at y=3500 m. In this scenario, negative total fluid pressures are an artifact imposed by the fluid extraction rate around the well.

In Figure 4-42 to Figure 4-50, the total fluid pressure is plotted along the cross-line through the reservoir for a range of reservoir porosity values from porosityRes=0.45 to porosityRes=0.05. The model simulations become unstable outside of this range. The reservoir permeability is set to 1e-12 m^2 for each case. All other parameters are as specified in Table 4-1.

For each model run, the total fluid pressure has the same initial profile at t=0 (immediately before activation of the extraction well). After activation, the cones of pressure depression around the extraction well (y=4500 m) are generally have the same amplitude with the progressing time step. The effect of the injection well is not seen at this scale. Nevertheless, maintenance of pore fluid pressures is strongly dependent on the

initial reservoir porosity. The higher initial porosities sustain the fluid pressures at higher levels throughout the simulation from t=0 to t=5 years.

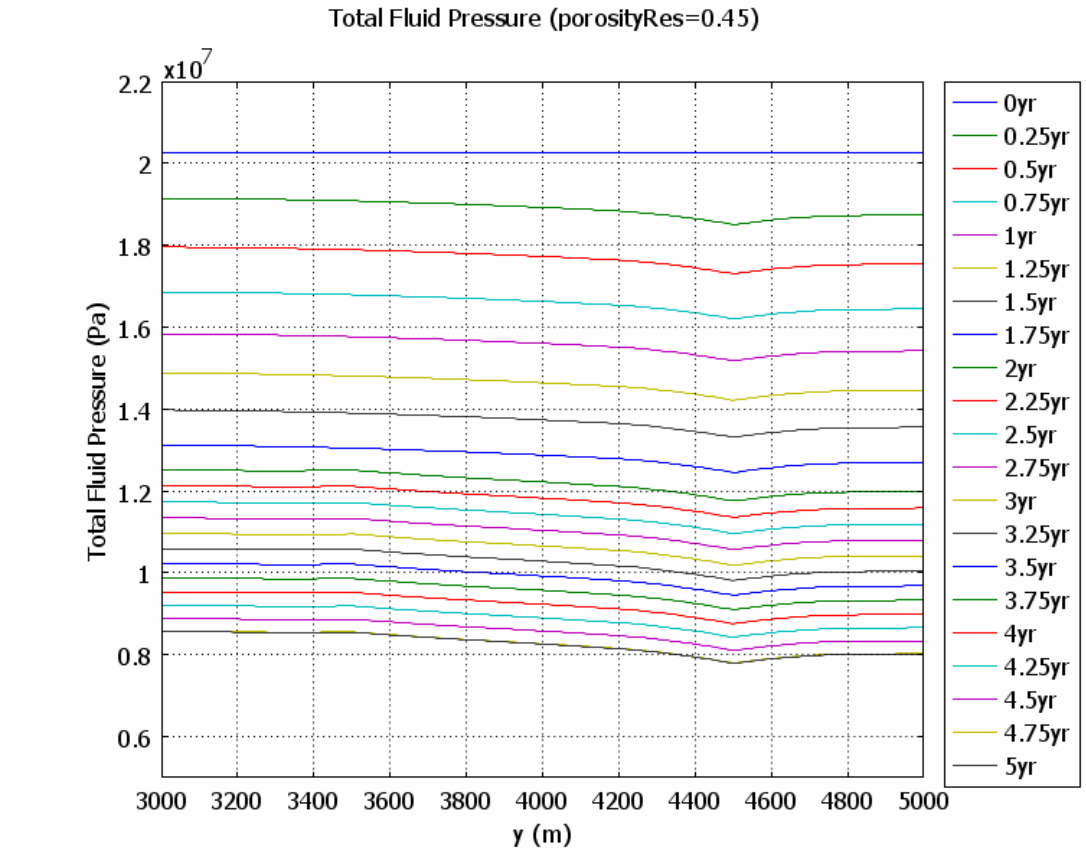

Figure 4-42. Total fluid pressure profile along a cross-line through the reservoir. In this case, the initial porosity is the parameter of interest and is set to 0.45. Reservoir permeability is 1e-12 m^2. All other parameters are as listed in Table 4-5.

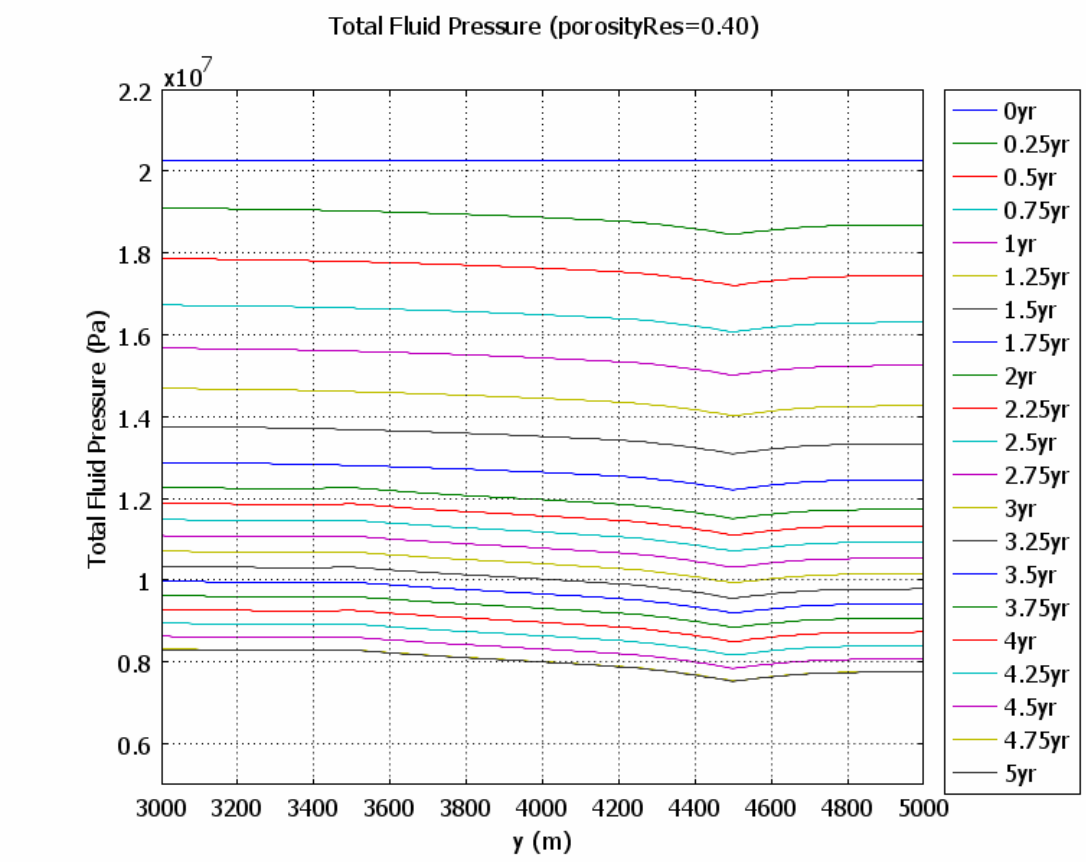

Figure 4-43. Total fluid pressure profile along a cross-line through the reservoir. In this case, the initial porosity is the parameter of interest and is set to 0.40. Reservoir permeability is 1e-12 m^2. All other parameters are as listed in Table 4-5.

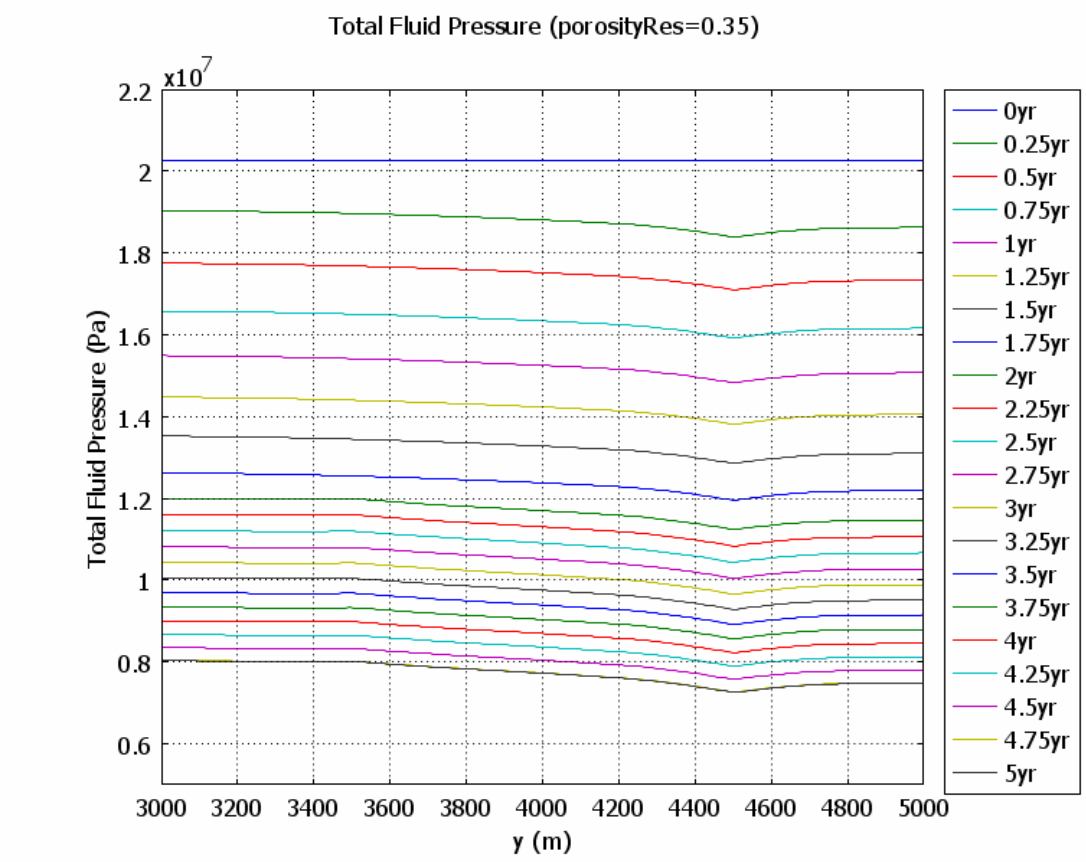

Figure 4-44. Total fluid pressure profile along a cross-line through the reservoir. In this case, the initial porosity is the parameter of interest and is set to 0.35. Reservoir permeability is 1e-12 m^2. All other parameters are as listed in Table 4-5.

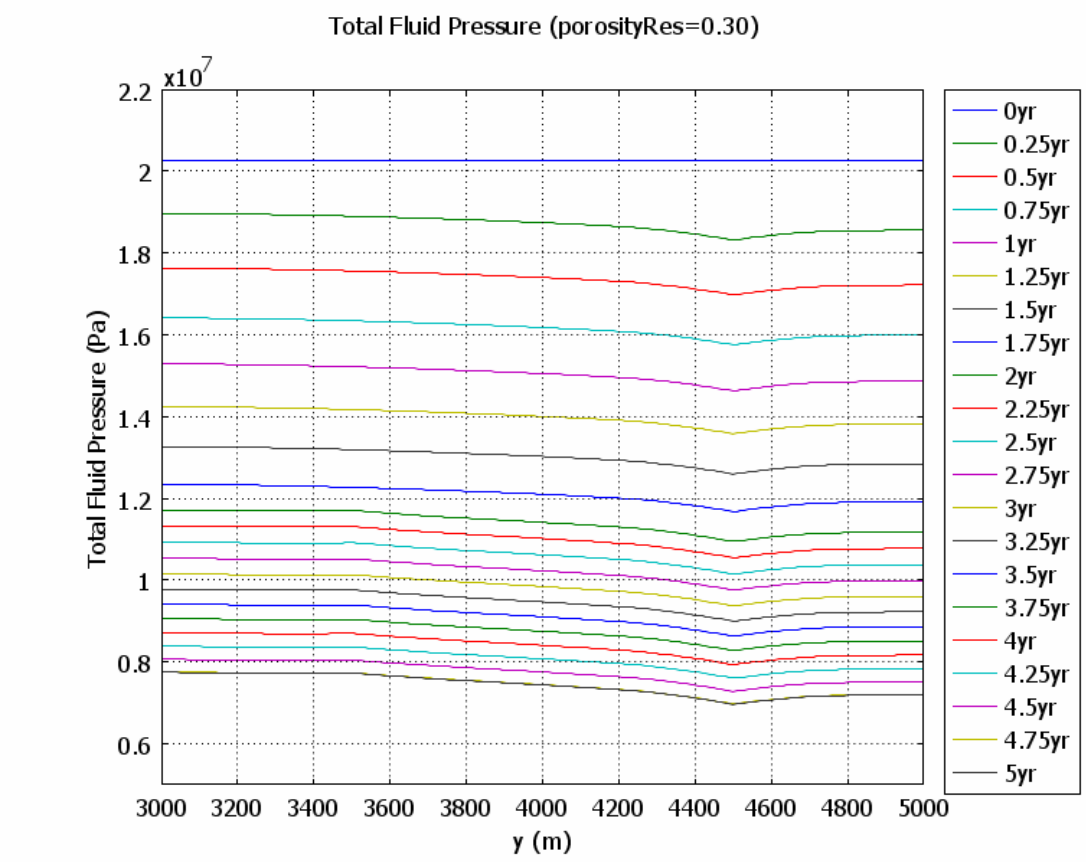

Figure 4-45. Total fluid pressure profile along a cross-line through the reservoir. In this case, the initial porosity is the parameter of interest and is set to 0.30. Reservoir permeability is 1e-12 m^2. All other parameters are as listed in Table 4-5.

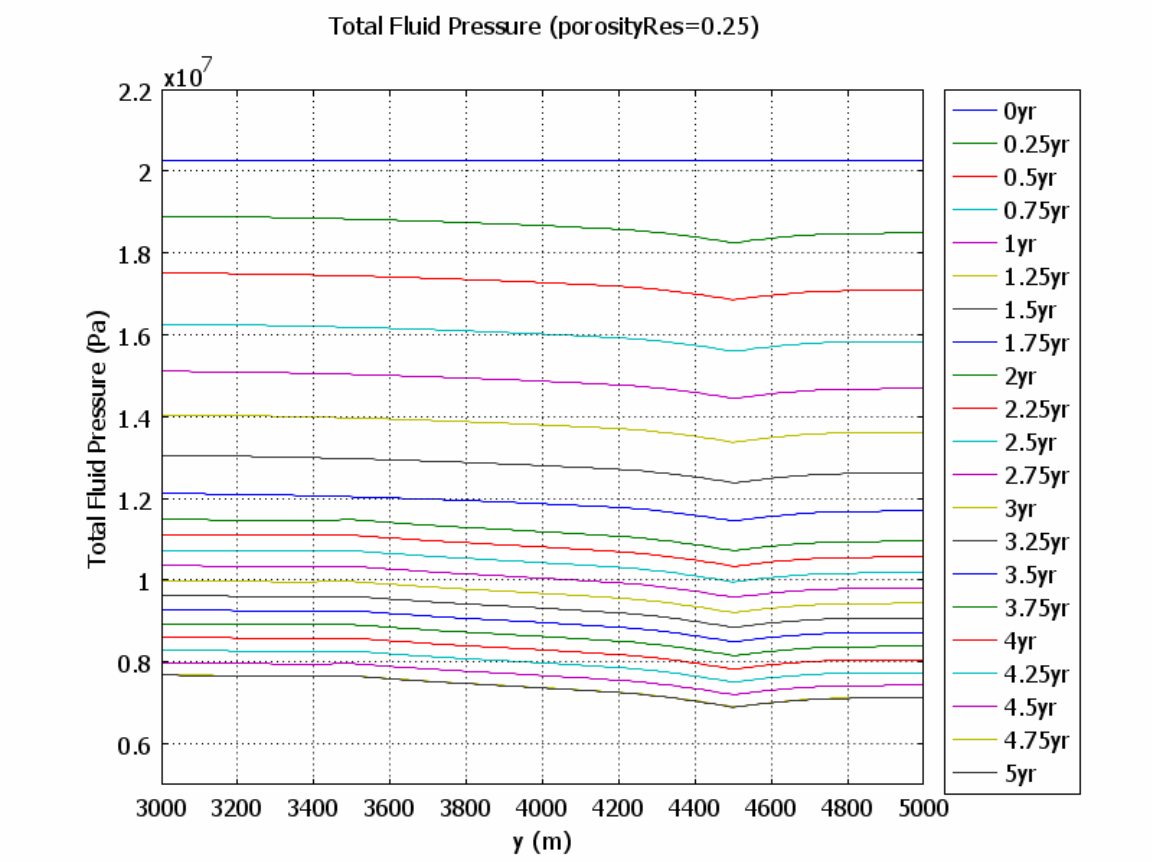

Figure 4-46. Total fluid pressure profile along a cross-line through the reservoir. In this case, the initial porosity is the parameter of interest and is set to 0.25. Reservoir permeability is 1e-12 m2. All other parameters are as listed in Table 4-5.

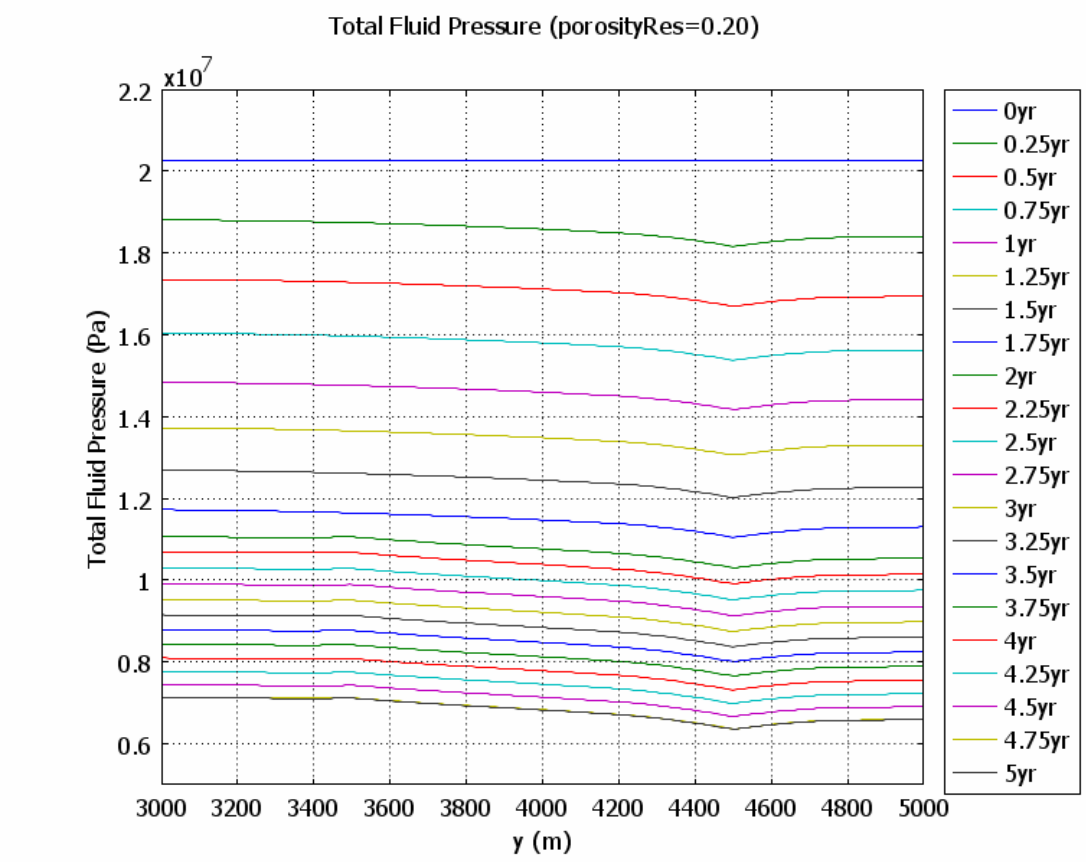

Figure 4-47. Total fluid pressure profile along a cross-line through the reservoir. In this case, the initial porosity is the parameter of interest and is set to 0.20. Reservoir permeability is 1e-12 m^2. All other parameters are as listed in Table 4-5.

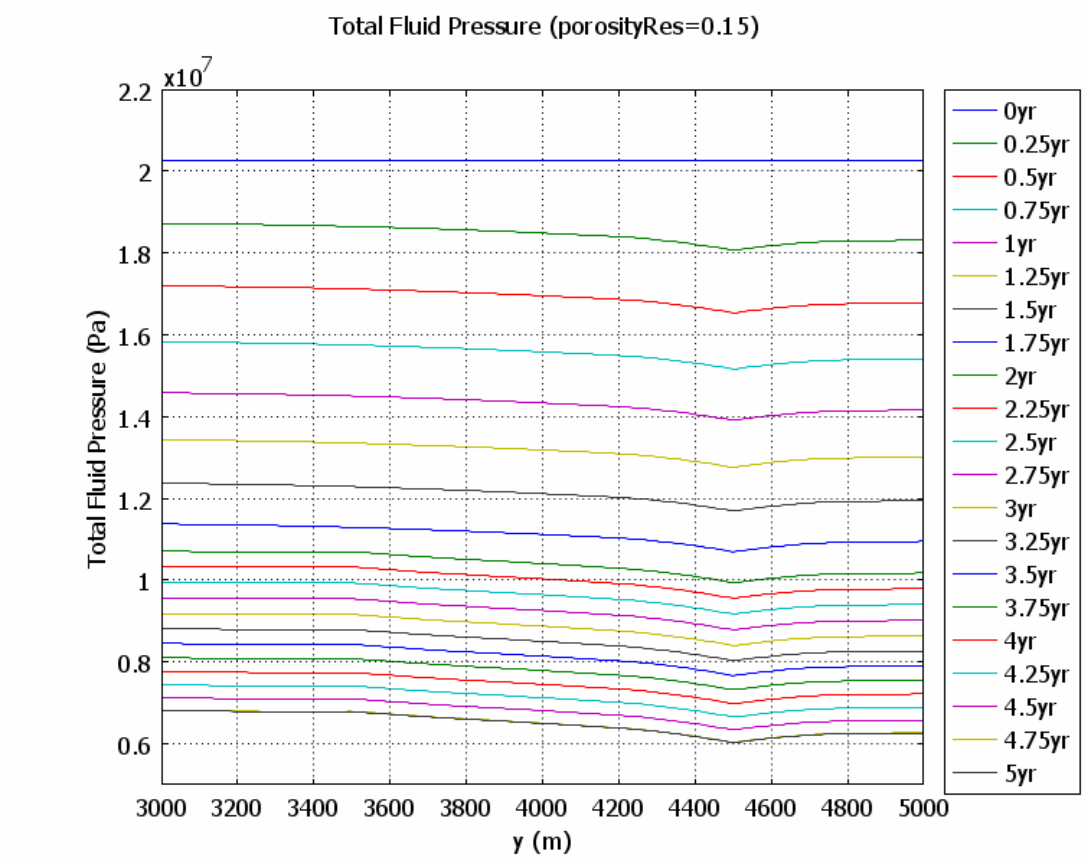

Figure 4-48. Total fluid pressure profile along a cross-line through the reservoir. In this case, the initial porosity is the parameter of interest and is set to 0.15. Reservoir permeability is 1e-12 m^2. All other parameters are as listed in Table 4-5.

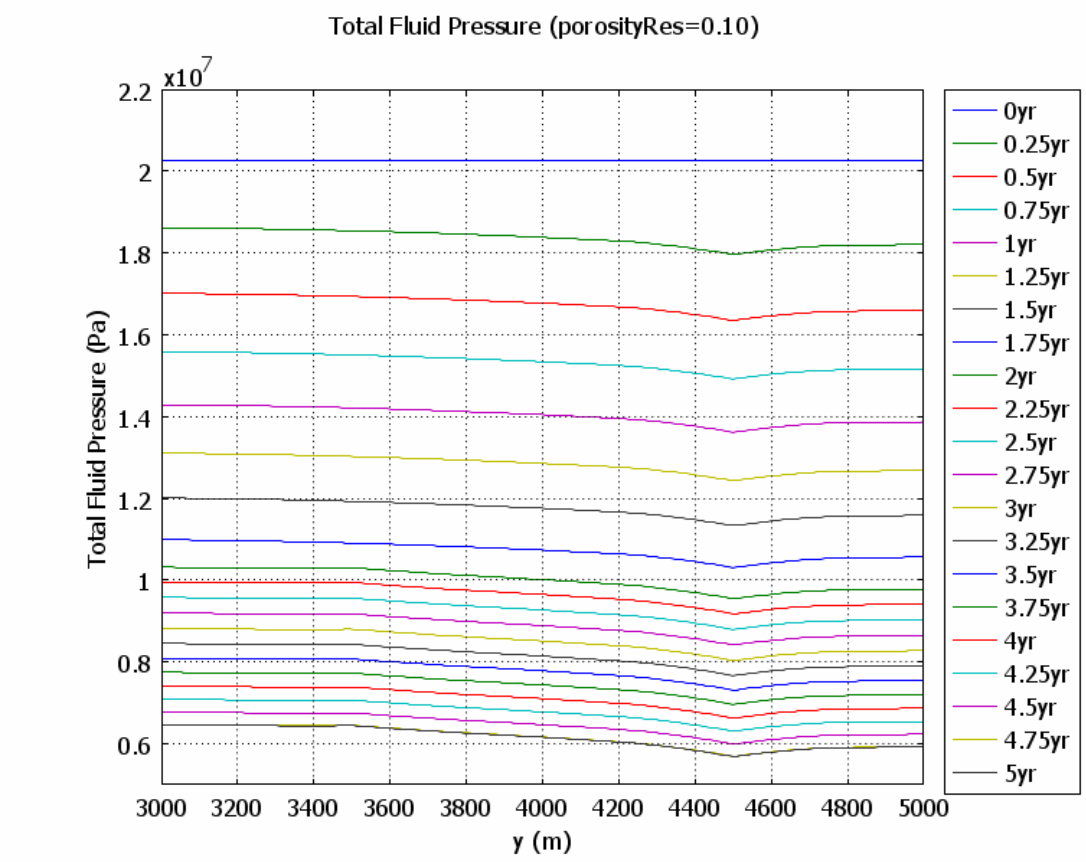

Figure 4-49. Total fluid pressure profile along a cross-line through the reservoir. In this case, the initial porosity is the parameter of interest and is set to 0.10. Reservoir permeability is 1e-12 m^2. All other parameters are as listed in Table 4-5.

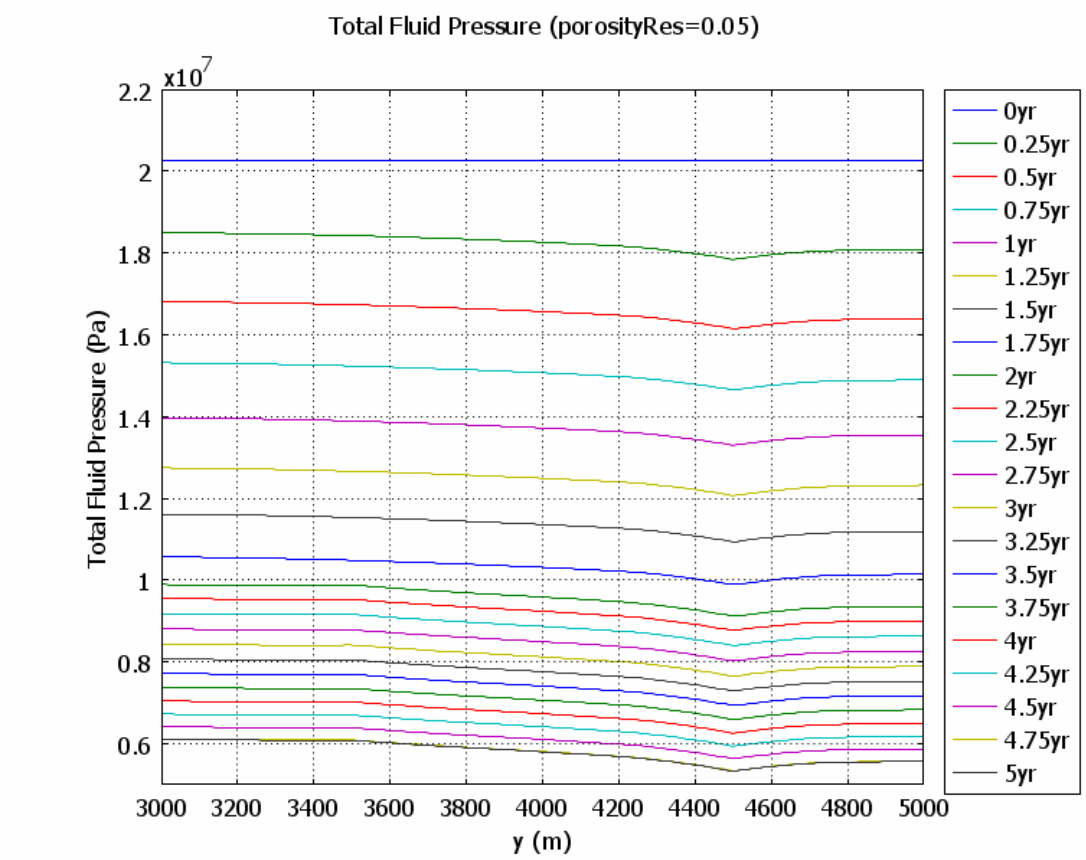

Figure 4-50. Total fluid pressure profile along a cross-line through the reservoir. In this case, the initial porosity is the parameter of interest and is set to 0.05. Reservoir permeability is 1e-12 m^2. All other parameters are as listed in Table 4-5.

4.7 Discussion on Stability

Sudden peaks in memory usage cause instability in Comsol's finite element time-dependent solver. *A priori* knowledge of when these peaks will occur is not possible in Comsol 3.3a. Comsol is developing a new product release that addresses this problem and better optimizes the time-dependent finite element algorithms. To circumvent these software and hardware limitations, the quality and number of finite elements must lowered manually to stabilize Comsol's time-dependent solver during all model simulations on a standard single 32-bit computer. Of course, the tradeoff is that some additional uncertainty is introduced in the computed solutions. However, each simulation will likely be affected in the same way, if all other parameters are held constant besides the one of interest. Furthermore, an initial comparison of pressure profiles generated from optimal finite element meshing (5000 elements) and relaxed meshing (1200

elements) showed no significant difference at the scales of interest. However, this may not be the case for more complicated, heterogeneous modeling scenarios. The optimal configuration for such projects would be to have multiple 64-bit computers running in parallel. 64-bit computers and 64-bit operating systems are quickly becoming the standard for desktop computers. The maximum theoretical memory space of a 64-bit CPU is 2^{64} unique memory addresses, equivalent to 16 exabytes. In comparison, the theoretical limitation of a 32-bit CPU is 2^{32} addresses, equivalent to 4 gigabytes. For the relaxed-mesh models presented in this section, the average peak memory usage was 1.1 gigabytes.

4.8 Summary of Salient Features

In this chapter, several numerical simulations have been presented with the intent of verifying the full poroelastic formation developed in Chapter 2 and implemented in Comsol's 3.3a finite element software. Models were developed to test simple 1-D Terzaghi consolidation, the Mandel-Cryer effect, and the Noordbergum effect. A model for simulating drill stem pressure-transient testing simulation was developed. A basin-scale hydrogeologic model was implemented and matched available data in the literature. This model included the effects of both horizontal and vertical displacements; in the classical Terzaghi approach, only vertical effects are considered.

Finally, a fully-coupled 3-D reservoir-scale model handling two-phase fluid flow was developed and directly linked strain to changes in seismic velocities through nonlinear elasticity theory. Using this approach, strain is linked to changes 3-D stress field. In this study, it was shown that vertical compressional wave velocity is sensitive to production-induced changes in vertical effective stress. Although only briefly discussed in this study, the Thomsen anisotropic coefficients and shear-wave splitting coefficient can be directly computed from this model. The coefficients are sensitive to stress-anisotropy induced by reservoir production. In particular, the model can be used to show that the magnitude of the shear-wave splitting coefficient increases concentrically around the reservoir during production. For modeling ,the coefficient can be measured from and/or calibrated to good quality multicomponent seismic reflection data (e.g., Davis, 2001; Sarkar et al., 2003; Prioul et al., 2004; Grechka and Soutter, 2005). This model can

be adapted and calibrated to fit a variety of production scenarios. Since the model is internally consistent, it has the benefit of being able to isolate the effect of varying individual parameters during multiple model simulations.

CHAPTER 5. CONCLUSIONS AND RECOMMENDATIONS

5.1 Conclusions

Sharp contrasts in geomechanical properties combined with inappropriate pumping schemes give rise to steep pressure gradients and large strains that may lead to well failure, lowering of the ground surface, disruption of subsurface fluid flow, and possible damage to infrastructural elements. To quantitatively predict both the vertical consolidation and the horizontal stretching associated with changing subsurface fluid flow, this thesis developed and verified a poroelastic finite element formulation that bidirectionally couples fluid pressure to solid rock deformation. This formulation is applied to laboratory and field applications with the goal of folding the results into criteria for predicting changes in stress and pore pressure fields. The poroelastic formulation correctly simulates the Mandel-Cryer (boundary) effect and the Noordbergum (heterogeneity) effect, two observable phenomena not accounted for in conventional flow models. Based on these study results, fluid flow in deformable porous media should be analyzed as a coupled fluid flow and deformation process, except for special, well-constrained problems where the deformation and stress conditions can be assumed *a priori*.

A nonlinear elasticity formulation was implemented for directly linking the changes in the effective stress field to changes in seismic velocities during production and injection. The vertical fast compressional wave, the slow (Biot) compressional wave, and the shear vertical wave were analyzed. The code is fully coupled and internally consistent, which is beneficial for isolating the sensitivity of individual parameters. The results were analyzed in terms of pore fluid pressure, effective vertical stress, strain, and seismic velocities. Fluid withdrawal from the reservoir causes "stress arching," which is manifested as negative strain (contraction) within the reservoir, and positive strain (expansion) in the host rock. Pore fluid pressures are tightly linked to the specified initial porosity and reservoir permeability. The specified initial porosity and the fluid content are the dominate controls on velocity changes, especially the slow (Biot) wave when a

certain threshold of permeability is met. These model results are based on laboratory data from a typical unconsolidated sandstone reservoir. The model code developed in this thesis can be modified to suit a variety of other particular reservoir conditions and production scenarios.

5.2 Recommendations for Future Work

Conventional reservoir simulators normally do not incorporate deformation and stress dynamics with changes in pressure during production simulations. The scope of this thesis has focused on bridging this gap between modeled fluid-structure interactions. A caveat here is that not all relevant thermal interactions, chemical alterations, rheological effects, and so forth, were captured in a comprehensive model. However, computational barriers involved in the robust coupling of the physical and chemical processes are being pushed back with the availability of inexpensive, high-performance hardware available on the desktop. Implementing coupled multiphysical simulations is becoming evermore feasible.

Although the topic of coupled geomechanical fluid flow simulations has received much attention in recent literature, challenging issues remain to be investigated, such as increasing computational algorithm efficiency, improving convergence/stability of numerical methods, uniting different numerical frameworks, coupling the thermal-elastic effects for seam assisted gravity drainage (SAGD) and other enhanced recovery techniques, analyzing geophysical anisotropy parameters, monitoring species transport, and simulating fracture growth, reorientation, and rheology.

This thesis has taken a needed step in implementing and developing a coupled approach to reservoir geomechanics. Obviously, the key to successfully applying this approach is to fine tune the best rock physics transform for the specific reservoir being studied. Special attention must be made to understanding the hysteresis of the loading/unloading/reloading path unique to each reservoir. It is also important to recognize the discrepancies between laboratory and field due to frequency dispersion and scale differences. Rock physics transforms may be assumed from laboratory measurements (e.g., Sarkar et al., 2003; Prioul et al., 2004). The heterogeneity of reservoir properties is generally more complex than idealized. For example, there may be

a distribution of different initial porosities. The uncertainties associated with the heterogeneities must be addressed as well.

An important phenomenon requiring more research and development is the hysteresis of the compaction mechanism (Figure 5-1). Clearly, theories of pure elasticity cannot account for inelastic effects of compaction, such as pore failure, breakage of cements, and grain decoupling, reorientation, and recontact. One way to approach this problem is by experimentally investigating triaxial strain pathways to map both the yield surfaces and the rock deformation processes in stress space (Scott, 2007). Scott discusses the concept of three deformational regimes: elasticity, pore collapse, and compaction. Acoustic velocity information suggests that each deformation regime has its own unique seismic signature. Contouring the "Q-P" (Q=shear-stress) and (P=mean-stress) stress space could be used to predict the velocities and anisotropies along any reservoir drawdown/rejection pathway.

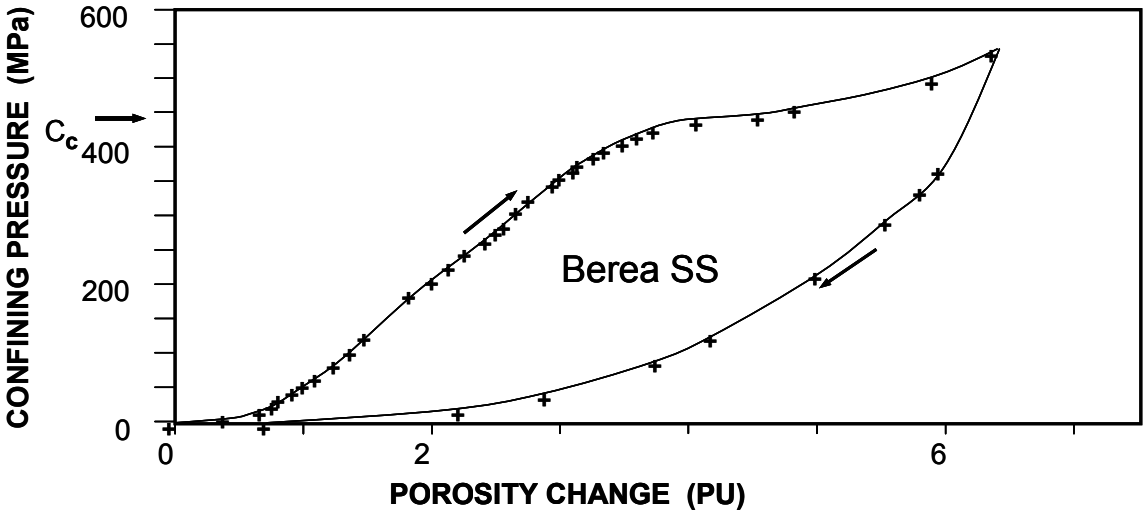

Figure 5-1. Confining pressure vs. porosity change, with irreversible compaction due to hysteresis. (after Batzle, 2006)

This thesis also serves as a springboard for modeling low-frequency laboratory experiments. The model developed to test the Mandel-Cryer effect (Section 4.3) could be adapted to represent the low-frequency apparatus shown in Figure 5-2. Boundary conditions of the Mandel-Cryer could be "inverted," so that there are no-flow boundaries along the exterior surfaces, except for the connecting fluid lines which have constant pore pressure. The sample is fixed at the bottom, but is otherwise free to deform. A low-

frequency sinusoidal load could then be applied to simulate the load being applied. Multiple scenarios could be run to develop relationships between stiffness coefficients and frequency.

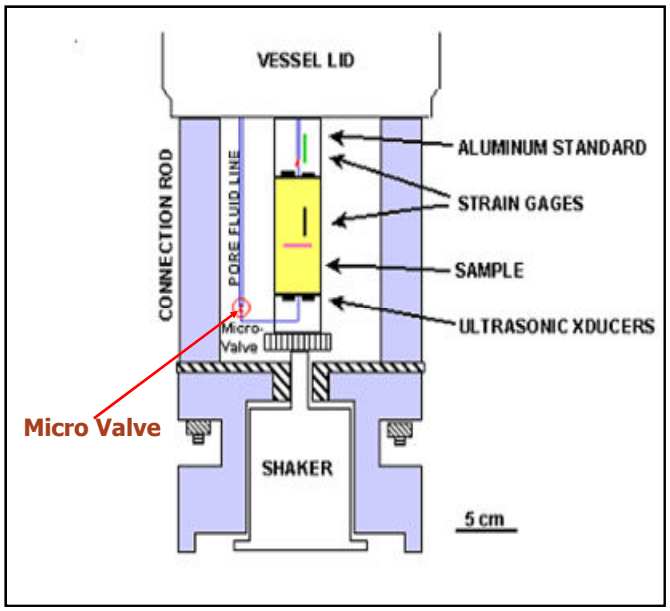

Figure 5-2. Schematic of low-frequency "shaker" apparatus (after Hofmann, 2005).

REFERENCES

Akers, S., 2001. Two-Dimensional Finite Element Analysis of Porous Geomaterials at Multikilobar Stress Levels. PhD Thesis, Virginia Polytechnic Institute and State University.

Allen, D., 1972, Environmental Aspects of Oil Producing Operations-Long Beach, California. Society of Petroleum Engineers Journal, paper SPE 3450.

Batzle, M., Han, D., Hofmann, R., 2006. Chapter 13, Rock Properties. In: L. Lake (Editor), Petroleum Engineering Handbook. Society of Petroleum Engineers.

Biot, M., 1941, General Theory of Three-Dimensional Consolidation. Journal of Applied Physics, 12(2): 155-164.

Biot, M., 1955, Theory of Elasticity and Consolidation for a Porous Anisotropic Solid. Journal of Applied Physics, 26(2): 182-185.

Biot, M.A., 1962, Mechanics of Deformation and Acoustic Propagation in Porous Media. Journal of Applied Physics, 33(4): 1482-1498.

Biot, M.A. and Willis, D.G., 1957, The Elastic Coefficients of the Theory of Consolidation. J. Appl. Mech., 24: 594-601.

Brooks, R. and Corey, A., 1966, Properties of Porous Media Affecting Fluid Flow, J. Irrigation and Drainage Div., Proc. Am. Soc. Civil Eng.(IR2), 92: 61-88.

Calvert, R., 2005. Insights and Methods for 4d Reservoir Monitoring and Characterization., Distinguished Instructor Series, No. 8.

Chen, C., Pei, S. and Jiao, J., 2003, Land Subsidence Caused by Groundwater Exploitation in Suzhou City, China. Hydrogeology Journal, 11(2): 275-287.

Chen, H., Teufel, L. and Lee, R., 1995, Coupled Fluid Flow and Geomechanics in Reservoir Study- I. Theory and Governing Equations. Society of Petroleum Engineers Journal(SPE 30752): 507-519.

Cheng, A. and Detournay, E., 1988, A Direct Boundary Element Method for Plane Strain Poroelasticity. International Journal for Numerical and Analytical Methods in Geomechanics, 12(5): 551-572.

Chilingarian, G., Donaldson, E. and Yen, T., 1996, Subsidence Due to Fluid Withdrawal. International Journal of Rock Mechanics and Mining Sciences and Geomechanics Abstracts, 33(3): 110A-110A.

Chin, L., Raghavan, R. and Thomas, L., 1998, Fully Coupled Analysis of Well Responses in Stress-Sensitive Reservoirs, Paper Spe 48967 Presented at the Spe Annual Technical Conference & Exhibition. New Orleans, Louisiana: 27-30.

Cook, C. and Jewell, S., 1995, Reservoir Simulation in a North Sea Reservoir Experiencing Significant Compaction Drive. Society of Petroleum Engineers Journal, SPE 29132.

Cryer, C., 1963, A Comparison of the Three-Dimensional Consolidation Theories of Biot and Terzaghi. The Quarterly Journal of Mechanics and Applied Mathematics, 16(4): 401.

Darcy, H., 1856, Les Fontaines De La Ville De Dijon. Dalmont, Paris.

Das, B., 2004. Principles of Foundation Engineering. Thomson/Brooks/Cole Pacific Grove, CA.

Davis, T.L., 2001, Multicomponent Seismology---the Next Wave. Geophysics, 66(1): 49.

Dean, R.H., Gai, X., Stone, C.M. and Minkoff, S.E., 2006, A Comparison of Techniques for Coupling Porous Flow and Geomechanics. SPE Journal, 11(1): 132-140.

Detournay, E. and Cheng, A., 1993, Fundamentals of Poroelasticity. Comprehensive Rock Engineering, 2: 113-71.

Duranti, L., Duranti, L. Time-Lapse Attenuation and Dispersion at Genesis--Chapter Four. Department of Energy Report., 2005.

Dusseault, M.B., Yin, S., Rothenburg, L. and Han, H., 2007, Seismic Monitoring and Geomechanics Simulation. The Leading Edge, 26(5): 610-620.

Dvorkin, J. and Nur, A., 1993, Dynamic Poroelasticity: A Unified Model with the Squirt and the Biot Mechanisms. Geophysics, 58(4): 524-533.

Fredrich, J.T., Arguello, J.G., Deitrick, G.L. and De Rouffignac, E.P., 2000. Geomechanical Modeling of Reservoir Compaction, Surface Subsidence, and Casing Damage at the Belridge Diatomite Field, SPE Reservoir Evaluation and Engineering, pp. 348-359.

Fuck, R., 2007. Personal Communication, M. Silbernagel.

Fuck, R.F., 2001, Phase Velocity Analytical Expressions for Body Waves Propagating in Horizontal Planes in Media with Hti, Orthorhombic and Monoclinic Symmetry. SEG Technical Program Expanded Abstracts, 20(1): 161-164.

Gambolati, G., Teatini, P., Bau, D. and Ferronato, M., 2000, Importance of Poroelastic Coupling in Dynamically Active Aquifers of the Po River Basin, Italy. Water Resources Research, 36(9): 2443-2459.

Gassmann, F., 1951, Uber Die Elastizitat Poroser Medien. Veirteljahrsschrift der Naturforschenden Gesellschaft in Zurich, 96: 1–23.

Geertsma, J., 1966, Problems of Rock Mechanics in Petroleum Production Engineering. Proceedings of 1st Congress on International Society of Rock Mechanics, I: 585-94.

Geertsma, J., 1973, Land Subsidence above Compacting Oil and Gas Reservoirs. J. Pet. Technol, 25: 734–744.

Gibson, R., Knight, K. and Taylor, P., 1963, A Critical Experiment to Examine Theories of Three-Dimensional Consolidation. Proceedings of European conference on soil mechanics and foundation engineering, Wiesbaden, 1: 69–76.

Grechka, V. and Soutter, L., 2005, Simulation of Two-Phase Fluid Flow through Compactible Reservoirs. Geophysical Prospecting, 53(6): 829-841.

Gutierrez, M. and Lewis, R.W., 1998. The Role of Geomechanics in Reservoir Simulation, Proceedings of the SPE/ISRM Rock Mechanics in Petroleum Engineering Conference, pp. 439-448.

Hackbarth, D., 1978, Application of the Drill-Stem Test to Hydrogeology. Ground Water, 16(1).

Hart, D., 2000. Laboratory Measurements of Poroelastic Constants and Flow Parameters and Some Associated Phenomena. PhD Thesis, University of Wisconsin--Madison.

Hatchell, P. and Bourne, S., 2005, Measuring Reservoir Compaction Using Time-Lapse Timeshifts. SEG Technical Program Expanded Abstracts, 24(1): 2500-2503.

Herwanger, J. and Horne, S., 2005, Predicting Time-Lapse Stress Effects in Seismic Data. The Leading Edge, 24(12): 1234-1242.

Holzer, T. and Johnson, A., 1985, Land Subsidence Caused by Ground Water Withdrawal in Urban Areas. GeoJournal, 11(3): 245-255.

International Energy Agency, Resources to Reserves, 2005. Paris, France.

Langguth, H. and Treskatis, C., 1989, Reverse Water Level Fluctuations in Semiconfined Aquifer Systems-- Rhade Effect. Journal of Hydrology JHYDA 7, 109(1-2).

Leake, S. and Hsieh, P., 1997. Simulation of Deformation of Sediments from Decline of Ground-Water Levels in an Aquifer Underlain by a Bedrock Step, US Geological Survey Open-File Report on Subsidence Interest, Feb. 14-16, Las Vegas, NV.

Lee, H., Torres-Verdín, C. and Sepehrnoori, K., 2006, Coupled Pressure-Transient Behavior and Geomechanical Deformation in the near-Borehole Region of

Unconsolidated Clastic Rock Formations. Society of Petroleum Engineers Journal(SPE 102904).

Lee, J., Rollins, J. and Spivey, J., 2003. Pressure Transient Testing, 9. Henry L. Doherty Memorial Fund of AIME, Society of Petroleum Engineers.

Lewis, R.W. and Schrefler, B.A., 1998. The Finite Element Method in the Static and Dynamic Deformation and Consolidation of Porous Media. John Wiley & Sons, New York.

Longuemare, P. et al., 2002, Geomechanics in Reservoir Simulation: Overview of Coupling Methods and Field Case Study. Oil & Gas Science and Technology, 57(5): 471-483.

Mandel, J., 1953, Consolidation Des Sols (Étude Mathématique). Geotechnique, 3(287): 99.

Mavko, G., Mukerji, T. and Dvorkin, J., 2003. The Rock Physics Handbook: Tools for Seismic Analysis of Porous Media. Cambridge University Press.

Means, W., 1976. Stress and Strain: Basic Concepts of Continuum Mechanics for Geologists. Springer-Verlag.

Minkoff, S. et al., 1999, Staggered in Time Coupling of Reservoir Flow Simulation and Geomechanical Deformation: Step 1–One-Way Coupling. Proceedings of the 1999 SPE Reservoir Simulation Symposium, Houston, TX., Feb: 14-17.

Minkoff, S., Stone, C., Bryant, S. and Peszynska, M., 2004, Coupled Geomechanics and Flow Simulation for Time-Lapse Seismic Modeling. Geophysics, 69(1): 200-211.

Minkoff, S., Stone, C., Bryant, S., Peszynska, M. and Wheeler, M., 2003, Coupled Fluid Flow and Geomechanical Deformation Modeling. Journal of Petroleum Science and Engineering, 38(1): 37-56.

National Academy of Sciences, Panel on Land Subsidence Report on Mitigating Losses from Land Subsidence in the United States, 1991. Washington D.C.

Noorishad, J., Ayatollahi, M. and Witherspoon, P., 1982, A Finite-Element Method for Coupled Stress and Fluid Flow Analysis in Fractured Rock Masses. Int. J. Rock Mech. Min. Sci. & Geomech. Abstr, 19: 185-193.

Olden, P. et al., 2001, Modeling Combined Fluid and Stress Change Effects in the Seismic Response of a Producing Hydrocarbon Reservoir. The Leading Edge, 20(10): 1154.

Osorio, J.G., Chen, H.Y., Teufel, L.W. and Schaffer, S., 1998, A Two-Domain, 3 D, Fully Coupled Fluid-Flow/Geomechanical Simulation Model for Reservoirs with

Stress-Sensitive Mechanical and Fluid-Flow Properties. EUROCK 98. Symposium.

Parker, J. and Lenhard, R., 1987, Model for Hysteretic Constitutive Relations Governing Multiphase Flow. 1. Saturation-Pressure Relations. Water Resources Research WRERAO, 23(12).

Poland, J., 1984, Mechanics of Land Subsidence Due to Fluid Withdrawal. Guidebook to Studies of Land Subsidence due to Groundwater Withdrawal: 37–54.

Prioul, R., Bakulin, A. and Bakulin, V., 2004, Nonlinear Rock Physics Model for Estimation of 3d Subsurface Stress in Anisotropic Formations: Theory and Laboratory Verification. Geophysics, 69(2): 415-425.

Prokofiev, D., 2007. Personal Communication, M. Silbernagel.

Rice, J. and Cleary, M., 1976, Some Basic Stress Diffusion Solutions for Fluid-Saturated Elastic Porous Media with Compressible Constituents. Reviews of Geophysics and Space Physics, 14: 227.

Ruddy, I., Anderson, M., Pattillo, P., Bishlawi, M. and Foged, N., 1989, Rock Compressibility, Compaction, and Subsidence in a High-Porosity Chalk Reservoir: A Case Study of Valhall Field. Journal of petroleum technology, 41(7): 741-746.

Sarkar, D., Bakulin, A. and Kranz, R., 2003, Anisotropic Inversion of Seismic Data for Stressed Media: Theory and a Physical Modeling Study on Berea Sandstone. Geophysics, 68(2): 690–704.

Scott, J., Thurman E., 2007, The Effects of Stress Paths on Acoustic Velocities and 4d Seismic Imaging. The Leading Edge, 26(5): 602-608.

Sen, V. and Settari, A., 2005, Coupled Geomechanical and Flow Modeling of Compacting Reservoirs. The Leading Edge, 24(12): 1284-1286.

Settari, A. and Mourits, F.M., 1998, A Coupled Reservoir and Geomechanical Simulation System. SPE Journal, 3(3): 219-226.

Settari, A. and Price, H., 1984, Simulation of Hydraulic Fracturing in Low-Permeability Reservoirs. Soc Pet Eng J, 24(2): 141-152.

Settari, A. and Walters, D.A., 1999. Advances in Coupled Geomechanical and Reservoir Modeling with Applications to Reservoir Compaction, SPE symposium on reservoir simulation. 14-17 February, Houston, pp. 345-357.

Sinha, B. and Winkler, K., 1999, Formation Nonlinear Constants from Sonic Measurements at Two Borehole Pressures. Geophysics, 64: 1890.

Terzaghi, K., 1925, Principles of Soil Mechanics. A Summary of Experimental Results of Clay and Sand'. Eng. News Rec, 3: 98.

Terzaghi, K., 1943. Theoretical Soil Mechanics. Wiley, New York.

Thomsen, L., 1986, Weak Elastic Anisotropy. Geophysics, 51(10): 1954-1966.

Thurston, R., 1974, Waves in Solids. Encyclopedia of Physics, Mechanics of Solids, VIa/4: 109-302.

Thurston, R. and Brugger, K., 1964, Third-Order Elastic Constants and the Velocity of Small Amplitude Elastic Waves in Homogeneously Stressed Media. Physical Review, 135(7AB): AB3 LP - AB3.

Timoshenko, S. and Goodier, J., 1951. Theory of Elasticity. McGraw-Hill, New York.

Tran, D., Nghiem, L. and Buchanan, L., 2005a. Improved Iterative Coupling of Geomechanics with Reservoir Simulation, SPE Reservoir Simulation Symposium, Proceedings. 2005 SPE Reservoir Simulation Symposium, Proceedings, Houston, TX, pp. 299-305.

Tran, D., Nghiem, L. and Buchanan, L., 2005b. An Overview of Iterative Coupling between Geomechanical Deformation and Reservoir Flow, SPE/PS-CIM/CHOA International Thermal Operations and Heavy Oil Symposium Proceedings. SPE/PS-CIM/CHOA International Thermal Operations and Heavy Oil Symposium, Calgary, AB.

Tran, D., Settari, A. and Nghiem, L., 2004, New Iterative Coupling between a Reservoir Simulator and a Geomechanics Module. SPE Journal, 9(3): 362-369.

Verruijt, A., 1969. Elastic Storage of Aquifers, In: Flow through Porous Media. Academic Press, New York.

Vidal, S., Huguet, F. and Mechler, P., 2002a, Characterizing Reservoir Parameters by Integrating Seismic Monitoring and Geomechanics. The Leading Edge, 21(3): 295.

Vidal, S., Longuemare, P., Huguet, F. and Mechler, P., 2002b, Reservoir Parameters Quantification from Seismic Monitoring Integrating Geomechanics. Oil and Gas Science and Technology, 57(5): 555-568.

Wang, H., 2000. Theory of Linear Poroelasticity : With Applications to Geomechanics and Hydrogeology. Princeton Series in Geophysics. Princeton University Press, Princeton, N.J.

Winkler, K. and Liu, X., 1995, Measurements of Third-Order Elastic Constants in Rocks. The Journal of the Acoustical Society of America, 98: 2886.

Wolff, R., 1970, Field and Laboratory Determination of the Hydraulic Diffusivity of a Confining Bed. Water Resources Research, 6(1): 194-203.

Woolley, J., 2004. Shock Tube Experiments Measuring and Modeling the Slow Wave in Low Permeability Rock Cores. M.S. Thesis, Colorado School of Mines, Golden, CO.

Yin, S., Dusseault, M.B., Rothenburg,L., 2006. Three Dimensional Hybrid Dd-Fem Model for Fully Coupled Reservoir Simulation, SPE Asia Pacific Oil & Gas Conference, Adelaide, Australia.

Zheng, Y., Burridge, R. and Burns, D., Reservoir Simulation with the Finite Element Method Using Biot Poroelastic Approach, 2003.

Zhu, X. and McMechan, G., 1991, Numerical Simulation of Seismic Responses of Poroelastic Reservoirs Using Biot Theory. Geophysics, 56: 328.

Zienkiewicz, O. and Taylor, R., 2000. Finite Element Method Volume 1: The Basis. John Wiley & Sons.

APPENDICES

APPENDIX A: Superposition of Finite Element Matrices and Notation

The following finite element matrices alluded to Chapter 3 are formed from the superposition of the following terms (after Gutierrez and Lewis, 1998):

$$\Phi_{ij} = \int_{\Omega} \left(\frac{\partial N_i}{\partial x_m} \frac{k_{mn}}{\mu} \frac{\partial N_j}{\partial x_n} \right) d\Omega$$

$$C_{ij} = \int_{\Omega} N_i N_j \phi c_T d\Omega$$

$$K_{ij} = \int_{\Omega} (B_{ik} D_{ikjl} B_{jl}) d\Omega$$

$$L_{ij} = \int_{\Omega} B_{ik} \left(\delta_{kl} - \frac{\delta_{mn} D_{mnkl}}{3K_s} \right) N_j \, d\Omega$$

$$S_{ij} = \int_{\Omega} N_i N_j \left(\frac{\phi}{K_f} + \frac{1-\phi}{K_s} - \frac{\delta_{mn} D_{mnkl} \delta_{kl}}{(3K_s)^2} \right) d\Omega$$

$$\Delta q_i = \oint_{d\Omega} N_i q \, dn - \oint_{\Omega} \frac{\partial N_i}{\partial x_m} k_{mn} \frac{\partial N_j}{\partial x_n} \rho g z \, d\Omega$$

where N_i=the element shape functions, and

$$B_{ij} = \frac{1}{2} \left(\frac{\partial N_i}{\partial x_j} + \frac{\partial N_j}{\partial x_i} \right)$$

APPENDIX B: Nonlinear Elasticity and Two-Phase Fluid Flow Theory

Nonlinear elasticity is a continuous medium theory that includes third-order terms that account for the change in acoustic properties with stress. In comparison to conventional linear elasticity, the potential energy is a second-order function of strains. It should be noted, however, the ordinary nonlinear elastic constants are still functions of the stress state and not the stress history. The effect of hysteresis in large strain and stress changes is not considered in the generic formulation.

To review and summarize the basic laws governing deformation (cf. Lewis and Schrefler, 1998; Wang, 2000; Sarkar et al., 2003; Grechka and Soutter, 2005), the linear momentum balance equations describing quasi-static motion of porous media are, in short hand, $\frac{\partial \sigma_{ij}}{\partial x_j} + \rho g = 0$ for i = 1,2,3 , where σ_{ij} is the total stress tensor, ρ is the bulk density of the saturated rock, and g is the (vertical) gravitational constant. The effective stress (σ'_{ij}) law gives the total stress tensor, $\sigma_{ij} = \sigma'_{ij} - \alpha p$ for i,j=1,2,3, where $\sigma'_{ij} = c_{ijkl}\varepsilon_{kl}$ for i,j=1,2,3. The minus sign in front of the Biot-Willis coefficient (α) represents the convention that pressure (p) is positive in compression and while stress components in the solid are positive in tension. The strain tensor, ε_{ij}, is a function of the displacement **u** of the solid frame, $\varepsilon_{ij} = \frac{1}{2}\left(\frac{\partial u_i}{\partial x_j} + \frac{\partial u_j}{\partial x_i}\right) for i, j = 1,2,3$. The bulk density of the rock is $\rho = (1-\varphi)\rho_s + \varphi\rho_f$ where the subscripts s and f refer to solid and fluid, respectively, and φ is porosity. The mixed fluid density is the sum of each fluid density multiplied by its respective saturation. For this thesis, two-phase flow is assumed, such that $S_{water} + S_{oil} = 1$. Further, the total pressure is the sum of each individual fluid pressure multiplied by its respective saturation (i.e., Delesse's Law): $p = S_1 p_1 + S_2 p_2$.

To complete the solid-fluid coupling, the fluid mass balance equations are:

$$A_{I1}\frac{\partial p_1}{\partial t} + A_{I2}\frac{\partial p_2}{\partial t} + S\alpha_{ij}\frac{\partial \varepsilon_{ij}}{\partial t} + A_{I1}\frac{\partial}{\partial t}\left(\frac{k_{ij}k_I^r}{\mu_I}\left(\rho_I g_g - \frac{\partial p_I}{\partial x_j}\right)\right) = F_I \text{ for I} = 1(\text{water}),2(\text{oil})$$

where t is time, k is the permeability tensor, k^r_1 and k^r_2 are the relative permeabilities of

the two fluids, μ is the dynamic fluid viscosity, and F is the fluid source or sink. The A matrix is given as

$$\begin{pmatrix} MS_1(S_1 + p_{cap}D + \phi D + \frac{\phi S_1}{K_1}) & MS_1\left(S_2 - p_{cap}D + \phi D\right) \\ MS_2\left(S_1 + p_{cap}D + \phi D\right) & MS_2(S_2 - p_{cap}D - \phi D + \frac{\phi S_2}{K_2}) \end{pmatrix}$$

where K_1 and K_2 are the bulk moduli of the fluids (water and oil), K_g is the bulk modulus of the grains, $p_{cap}=p_2-p_1$ is the capillary pressure, D is the specific moisture content, $M=(\alpha-\varphi)/K_g$, and $\alpha=1-K/K_g$. The two-phase fluid problem is also nonlinear because the relative permeabilities (k^r) and fluid saturations (S) depend on unknown fluid pressures (p). The saturations and relative permeabilities are determined from empirical two-phase fluid functions of capillary pressure (e.g., Brooks and Corey, 1966; Parker and Lenhard, 1987; Lewis and Schrefler, 1998; Grechka and Soutter, 2005). The concept of effective saturation (S_1') is described by Parker et al. (1987) in terms of the wettability of the saturating fluid (S_1), such that $S_1'=(S_1-S_{1,irr})/(S_{1,sat}-S_{1,irr})$, where $S_{1,sat}$ is full saturation and $S_{1,irr}$ is the irreducible saturation of water. In the model developed in this thesis, water is assumed to be the wetting fluid ($S_{1,sat}$=0.96 and $S_{1,irr}$=0.20). Further, the effective saturation (for $p_{cap}>0$) is given by an empirical equation (Parker and Lenhard, 1987): $S_1'=(1+(\beta p_c)^n)^m$ where β and n are empirical parameters (β=0.01 m^{-1} and n=2) and m=(1-1/n). Given these relations, the saturation of water (S_1) can be thus be inverted. Then, the oil saturation (S_2) can be found assuming $S_2=1-S_1$ for two-phase fluid flow. The relative permeabilities are also given as functions of the effective saturation, such that: $k^r_1=(S_{1,eff})^{0.5}(1-(1-S^{1/m}_{1,eff})^m)^2$ and $k^r_2=(1-S_{1,eff})^{0.5}(1-S^{1/m}_{1,eff})^{2m}$.

Finally, the seismic velocity responses are related to the changes in the coupled system (Sarkar et al., 2003). In the absence of pre-existing stresses, the stiffness tensor **c** is defined in terms of the second- and third-order stiffness tensors:

$c_{ijkl} = c^{(2)}_{ijkl} + c^{(3)}_{ijklmn}\varepsilon_{mn}$ for i, j, k, $l = 1,2,3$. $c^{(3)}_{ijklmn}$ is defined by the three intrinsically isotropic third-order stiffness tensors, c111, c112, and c123. Using Matlab expressions for contracted Voigt notation, the simplified equations for the effective elastics constants of solid in the initial reference configuration are given as:

```
c11 =     c110+c111*e11+c112*(e22+e33)
c12 =     c120+c112*(e11+e22)+c123*e33
```

```
c13 =       c130+c123*e22+c112*(e11+e33)
c14 =       c140+2*c144*e23
c15 =       c150+2*c155*e13
c16 =       c160+2*c155*e12
c22 =       c220+c111*e22+c112*(e11+e33)
c23 =       c230+c123*e11+c112*(e22+e33)
c24 =       c240+2*c155*e23
c25 =       c250+2*c144*e13
c26 =       c260+2*c155*e12
c33 =       c330+c112*(e11+e22)+c111*e33
c34 =       c340+2*c155*e23
c35 =       c350+2*c155*e13
c36 =       c360+2*c144*e12
c44 =       c440+c144*e11+c155*(e22+e33)
c45 =       c450+2*c456*e12
c46 =       c460+2*c456*e13
c55 =       c550+c144*e22+c155*(e11+e33)
c56 =       c560+2*c456*e23
c66 =       c660+c155*(e11+e22)+c144*e33
```

where strains are

```
e11 =       ux
e22 =       vy
e33 =       wz
e23 =       (vz+wy)/2
e13 =       (uz+wx)/2
e12 =       (uy+vx)/2
```

and the second-order elastic stiffness constants are

```
c110 =      rho*VpSolid^2
c120 =      rho*VpSolid^2 – 2*rho*VsSolid^2
c130 =      rho*VpSolid^2 – 2*rho*VsSolid^2
c220 =      rho*VpSolid^2
c230 =      rho*VpSolid^2 – 2*rho*VsSolid^2
c330 =      rho*VpSolid^2
c440 =      rho*VsSolid^2
c550 =      rho*VsSolid^2
c660 =      rho*VsSolid^2
c144 =      (c112-c123)/2
c155 =      (c111-c112)/4
c456 =      (c111-3*c112+2*c123)/8
```

The stresses and vertical seismic velocities are

```
t11 =           c11*e11+c12*e22+c13*e33+c14*e23+c15*e13+c16*e12
t22 =           c12*e11+c22*e22+c23*e33+c24*e23+c25*e13+c26*e12
t33 =           c13*e11+c23*e22+c33*e33+c34*e23+c35*e13+c36*e12
t23 =           c14*e11+c24*e22+c34*e33+c44*e23+c45*e13+c46*e12
```

```
t13 =          c15*e11+c25*e22+c35*e33+c45*e23+c55*e13+c56*e12
t12 =          c16*e11+c26*e22+c36*e33+c46*e23+c56*e13+c66*e12
Vp0 =          sqrt(c33/rho)
Vs0 =          sqrt(c55/rho)
VpSlow =       (VpFluidMix)/((1-0.5*(1-1/porosity))^(0.5))
VpFluidMix=    ( (VpWat*(sw)+VpOil*(so))+((sw)/VpWat+(so)/VpOil)^-1 )/2
```

where VpSlow is the slow (Biot) dispersive wave velocity given by a tortuosity formulation (Zhu and McMechan, 1991), and VpFluidMix is a Voigt-Reuss-Hill average of the compressional wave velocities (VpWat and VpOil) of the saturating fluid components (sw and so, for water and oil, respectively).